Report

R-18-06

May 2019

Greenland ICE project

Final report

Joel Harper

Toby Meierbachtol

Neil Humphrey

SVENSK KÄRNBRÄNSLEHANTERING AB

SWEDISH NUCLEAR FUEL
AND WASTE MANAGEMENT CO

Box 3091, SE-169 03 Solna
Phone +46 8 459 84 00
skb.se

ISSN 1402-3091
SKB R-18-06
ID 1674708

May 2019

Greenland ICE project

Final report

Joel Harper, Toby Meierbachtol
University of Montana

Neil Humphrey, University of Wyoming

This report concerns a study which was conducted for Svensk Kärnbränslehantering AB (SKB), NWMO (Canada), Posiva Oy (Finland) and Nagra (Switzerland). The conclusions and viewpoints presented in the report are those of the authors. SKB may draw modified conclusions, based on additional literature sources and/or expert opinions.

Data in SKB's database can be changed for different reasons. Minor changes in SKB's database will not necessarily result in a revised report. Data revisions may also be presented as supplements, available at www.skb.se.

Summary

Safety assessments of potential underground repository locations prone to future glaciations must consider the impact of ice sheet advance on site conditions. This requires detailed knowledge of the processes and conditions at the boundary coupling ice sheet and earth systems. The ICE Project employed the Greenland ice sheet as a field laboratory to advance understanding of the physical processes governing ice/water/earth interactions.

Detailed instrumentation, data collection, and analysis of a portion of the Greenland ice sheet were performed to address four science objectives focused on: 1) interpreting the physical framework of the ice sheet bed, 2) quantifying the magnitude of, and spatial gradients in, basal water pressure, 3) determining the presence of short duration water pressure transients in the ice sheet basal drainage system, and 4) advancing understanding of the distribution of water along the ice sheet bed. Access to the full ice thickness was created through nine boreholes drilled to the bed by a hot water drill. Sensors installed at the surface, within the ice, and at the basal boundary of a ~700 × 700 × 700-meter block of ice generated a comprehensive dataset spanning three years. These data were interpreted with respect to the ~50 km long transect of observations previously collected by the Greenland Analogue Project (GAP) in order to accomplish the project objectives.

Findings from the ICE Project demonstrate that the bed of the study site and the GAP borehole study transect is bedrock with a relatively thin cover of sediment, indicating that the subglacial drainage system is of a ‘hard-bed’ type rather than porous-till type. The basal water pressure was confined to a limited range between 0.8–1.1 as a fraction of ice overburden pressure. Two types of spatial gradients were identified: 1) a primary gradient driven by the large-scale longitudinal change in ice overburden pressure, and 2) secondary local gradients related to the dynamics of the subglacial drainage system. Measurements showed that drainage system pressure changes arise from mechanical adjustments to drainage system volume, in addition to basal water flow dynamics.

Very rare pulses in pressure occurred within the subglacial drainage system, reaching magnitudes of 0.72 MPa, but were spatially localized. Ice deformation inhibits the reliable estimation of water volume changes at the ice/bed interface utilizing elevation changes of the ice surface. The large-scale geometry of the ice sheet reflects enhanced basal sliding, most likely related to the occurrence of water at the ice/bed interface.

Sammanfattning

Analyser av långsiktig säkerhet för potentiella slutförvarsplatser i områden som kan komma att nedisas i framtiden, måste beakta den påverkan som en inlandsis har på förhållandena vid förvarsplatsen. Detta kräver detaljerad kunskap om processer och förhållanden som råder vid inlandsisens botten. ICE-projektet har därför använt en del av den grönländska inlandsisen som fältlaboratorium för att förbättra förståelsen för de fysikaliska processer som styr interaktionen mellan is, vatten och geosfär (jord, berggrund).

Detaljerad instrumentering, datainsamling och analys gjordes för den utvalda delen den Grönländska inlandsisen för att studera fyra vetenskapliga områden; 1) beskrivning och tolkning av det fysikaliska ramverket vid inlandsisens botten, 2) kvantifiering av storleken på, och rumsliga gradienter i, basalt vattentryck, 3) detektion och beskrivning av eventuell förekomst av kortvariga vattentrycktransienter i det basala dräneringssystemet, och 4) öka förståelsen av vattnets fördelning vid botten av inlandsisen. Observationer av hela isens egenskaper, från ytan ner till bottnen, erhölls genom att nio borrhål borrades till botten med en varmvattenborr. Sensorer installerade från isytan och igenom isen ned till botten i ett ”isblock” med storleken 700 × 700 × 700 meter. Från denna installation erhölls ett omfattande dataset som i tiden sträckte sig över tre år. Dessa data tolkades sen i sammanhanget av tidigare resultat från den ca 50 km långa profil av observationer som samlades in inom ramen för Greenland Analog Project (GAP).

Resultaten från ICE-projektet visar, tillsammans med tidigare resultat från GAP studien, att botten av isen inom det undersökta området utgörs av berggrund med ett relativt tunt sedimentlager, vilket i sin tur indikerar att det subglaciala dräneringssystemet är av en ”hard bed”-typ snarare än av porös-morän-typ. Det basala vattentrycket är begränsas till intervallet 0,8 till 1,1 (uttryckt som del av isövertrycket). Två typer av rumsliga gradienter identifierades: 1) en primär gradient vilken drivs av den storskaliga longitudinella förändringen i isövertrycket, och 2) sekundära lokala gradienter relaterade till dynamiken i det subglaciala dräneringssystemet. Mätningar visade att tryckförändringar i dräneringssystemet uppstår från mekaniska justeringar av dräneringssystemets volym, utöver de förändringar som orsakas av det basala vattenflödessystemet egna dynamik.

Mycket sällsynta (i tid) och lokalt förekommande tryckpulser observerades i det subglaciala dräneringssystemet, vilka nådde en magnitud på 0,72 MPa. Användandet av höjdförändringar hos isöverytan för uppskattningar av vattenvolymförändringar vid isens botten hämmas av isdeformationen. Inlandsisens storskaliga geometri återspeglar förstärkt basal glidning (enhanced basal sliding, Eng.), sannolikt relaterad till förekomsten av vatten vid isens botten.

Contents

1 Introduction: motivation and scope

1.1 Background

During future ice ages, deep geologic repositories (DGRs) for nuclear waste that are located in historically glaciated regions (e.g. Sweden, Finland, Canada and Switzerland) are likely to again be overridden by ice. When ice is present at a repository site, the conditions at the base of the glacier or ice sheet form a surficial boundary condition to the underlying groundwater system. The glacier bed boundary conditions must be carefully considered when conducting groundwater flow simulations for safety assessment purposes. For instance, the frozen/melted conditions at the glacier bed determine whether free water is available to recharge the groundwater system. The physical bed conditions (extensive sediment vs. hard bedrock) determine whether the glacier basal drainage system between ice and bedrock is everywhere connected to the groundwater system (as is the case where the glacier bed is composed of thick, saturated sediment), or if recharge to the groundwater system is limited to discrete drainage system elements developed over bedrock. Further, drainage system processes at the ice-bed interface redistribute and focus water at the glacier bed, creating a water pressure field that is spatially and temporally variable. These and other glaciological factors, therefore, impact the mechanical and hydrogeological boundary between ice and earth domains, and potentially influence gradients that develop over the course of a glacial cycle.

One of the few ways to investigate the ice sheet boundary condition relevant to future repository assessment is to study a modern-day analogue such as the Greenland Ice Sheet (GrIS). The most comprehensive effort to directly investigate the basal conditions of the GrIS to date has been the 'Greenland Analogue Project' (GAP) funded by the nuclear waste management organisations SKB in Sweden, Posiva Oy in Finland, and NWMO in Canada (Claesson Liljedahl et al. 2016, Harper et al. 2016). The research conducted within the GAP resulted in important advancements to the understanding of the thermal and hydrologic conditions at the ice sheet basal boundary – critical information to assess the role of an ice sheet in the context of groundwater flow.

At the conclusion of the GAP, several important aspects of the basal boundary study remained uncertain or required further investigation. Additionally, new scientific questions, pertaining to time and space variations in the basal boundary condition, arose that are relevant to site assessment calculations under glacial conditions. This motivated the ICE project to address the outstanding uncertainties, and advance the conceptualisation of the ice-bed interface condition, through analysis and integration of existing GAP data along with new borehole information collected on the GrIS.

1.2 Objectives

The overarching goal of the ICE project is to advance key knowledge gaps related to the ice sheet – groundwater boundary by focusing research on four objectives:

Objective 1) Build a physical framework of basal conditions: The GAP presented preliminary evidence that the borehole study sites consist of a 'hard bed' (Harper et al. 2016; section 4.10.1), implying that the ice-bed interface in the study region is characterised by bedrock rather than a thick and persistent layer of sediment. The ICE project aimed to introduce new and more detailed observations and more in-depth analysis to develop the framework of the ice-bed interface.

Objective 2) Quantify water pressure and spatial gradients at the bed: The GAP yielded important observations of hydraulic head conditions at the ice-bed interface at distances as far as 50 kilometres from the ice sheet margin. This work demonstrated consistently high values near overburden and identified local scale (~20 m) hydraulic head gradients at the bed reaching approximately 16 kPa/m (0.16) (Harper et al. 2016; section 4.10.3). Local scale hydraulic gradients, however, were not reconciled against those estimated at regional scale (tens of km), and GAP results were not adequately contextualized with regards to other measurements in Greenland. The ICE project aimed to compare local hydrologic gradients to regional gradients, and to compare GAP and new data to other Greenland datasets.

Objective 3) Measure the presence or absence of short duration pressure transients in the drainage system: Prior research on mountain glaciers has revealed that very high, but short duration, pressure pulses sometimes occur in the basal drainage system (Kavanaugh 2009, Kavanaugh and Clarke 2000). No pressure spikes were documented in the studied portion of the GrIS during the GAP, but instrumentation deployed during the project was not capable of capturing such short duration events. The ICE project aimed to deploy suitable instrumentation and data analysis focused on short duration pressure pulses.

Objective 4) Advance the conceptualisation of water distribution at the ice sheet bed: At the local scale, the distribution and flux of water through basal drainage elements is central to understanding where there is water along the ice sheet bed. At the regional scale, uncertainty persists regarding the distribution of water at the bed in the ice sheet interior; particularly as it relates to the introduction of water from the surface. The ICE project aimed to address these problems through studies at the local and regional scale.

Scientific findings from the ICE project have been published in five independent, peer-reviewed publications. A sixth publication is currently in preparation. The published works and manuscript in progress are presented in this report as appendices, summarised in Table 1-1. The intent of this report is to present a summary of the research and outcomes from studies related to the four objectives, and to synthesise key findings within the conceptualisation of the ice sheet basal boundary that are relevant to future activities focused on repository safety assessment. Chapter 2 details the study area and ICE project field activities within the context of the existing GAP sites. Chapter 3 presents a brief summary of the findings from the ICE project. Chapter 4 synthesises these findings within the context of the conceptualisation of the basal drainage system, and offers key findings that may need consideration in future safety assessments of deep geologic repositories that employ ice sheet-groundwater modeling.

Table 1-1. Summary of Appendices in this Report and Study Objectives.

Appendix in this report	Paper associated with Appendix	Objective addressed
Appendix A	**Harper J T, Humphrey N F, Meierbachtol T W, Graly J A, Fischer U H, 2017.** Borehole measurements indicate hard bed conditions, Kangerlussuaq sector, Western Greenland Ice Sheet. Journal of Geophysical Research: Earth Surface 122, 1605–1618.	Obj 1
Appendix B	**Wright P J, Harper J T, Humphrey N F, Meierbachtol T W, 2016.** Measured basal water pressure variability of the Western Greenland Ice Sheet: Implications for hydraulic potential. Journal of Geophysical Research: Earth Surface 121, 1134–1147.	Obj 2
Appendix C	**Meierbachtol T W, Harper J T, Humphrey N F, 2018.** Short duration water pressure transients in Western Greenland's subglacial drainage system. Journal of Glaciology 64, 171–174.	Obj 3
Appendix D	**Meierbachtol T W, Harper J T, Humphrey N F, Wright P J, 2016.** Mechanical forcing of water pressure in a hydraulically isolated reach beneath Western Greenland's ablation zone. Annals of Glaciology 57, 62–70.	Obj 4
Appendix E	**Meierbachtol, T W, Harper J T, Humphrey N F, Maier N, In Preparation.** Local basal water storage: assessment of estimates from surface elevation measurements.	Obj 4
Appendix F	**Meierbachtol T, Harper J, Johnson J, 2016.** Force balance along Isunnguata Sermia, West Greenland. Frontiers In Earth Science 4. doi:10.3389/feart.2016.00087	Obj 4

2 Project design

Studies of subglacial conditions undertaken by the GAP were conducted in a transect of boreholes spanning the GAP study region (Figure 2-1 and 2-2). The boreholes were drilled at separate sites along the transect, with two or three boreholes at each site spaced 20–30 m apart. This permitted hydrological conditions to be quantified over a nearly 50 km long reach of the Greenland ablation zone.

The ICE project employed an approach to data collection different than any prior study, with complete focus on intensive study of a single site (Figure 2-1 and 2-2). The aim was to heavily instrument a block of ice, its underlying bed and the ice surface. The dimensions of the block were equivalent to approximately one ice depth, in this case 700 × 700 × 700 m. The chosen 'block site' is 33 km inland from the Isunnguata Sermia terminus, at a location with a relatively smooth, flat bed, and a reverse (slight) bed slope (i.e. the bed slopes to the east, away from the ice margin). Bedrock troughs several hundred meters deep are located to both the north and the south. Thus, the block site is flanked by ice exceeding 1 000 m thick.

The study block was instrumented with five GPS stations at the surface, which were arranged in a four-point diamond with the fifth point at the centre (Figure 2-1). Ten total boreholes were drilled, nine of which extended to the bed within the block. These holes were arranged in a smaller double-diamond pattern (Figure 2-1, Figure 2-3). The western diamond of the boreholes was drilled in 2014, and the remaining boreholes were drilled and instrumented in 2015. Data were collected from the network of surface and borehole sensors during the summer in 2015, 2016 and 2017. Due to the fact that 1) instrumentation was installed in two different years, 2) environmental conditions resulted in data gaps (e.g. GPS units power down during the dark winter when solar charging does not occur), and 3) not all sensors remained functional through the full duration of the project, not all sensors were operational at the same time.

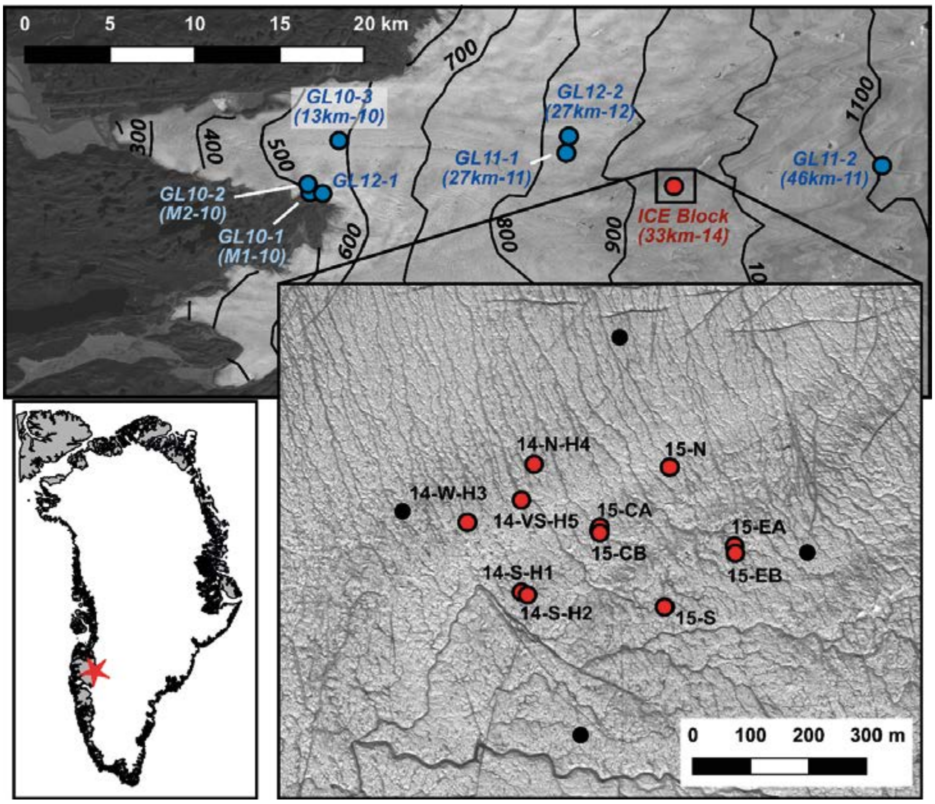

Figure 2-1. *Map showing the location of boreholes (nine drilled to the bed; red dots) at the ICE project block study site. Black dots are locations of five continuously logging GPS stations. A fifth GPS station was installed in the center of the study site but is obscured in the figure by boreholes 15-CA and 15-CB. A meteorological station was installed at the centre location of the nine hole arrangement. Background is satellite image showing ice surface. Inset shows block location with respect to other GAP borehole sites (blue dots). Sites are labelled following the GAP final report. Site names in parentheses correspond to nomenclature in Appendices A and B. Black contours illustrate surface topography following Bamber et al. (2013).*

The ice temperature structure of the block is described in Hills et al. (2017). The vertical temperature structure of our instrumented block follows the expected pattern of coldest temperature approximately midway through the ice depth. The ice at the bed is at the pressure melting point, with a thin layer of temperate basal ice up to ~5 m thick. Above the warm basal layer, ice becomes colder, following a roughly linear temperature gradient of about −0.04 °C/m until the coldest temperatures of about −10 to −12 °C between 200 and 300 m below ice surface. Above the cold core, the ice becomes progressively warmer toward the surface, with a gradient of approximately +0.01 °C/m. Measured temperatures in the near-surface ice (20 m depth) are −9.5 °C, slightly warmer than the mean annual air temperature of −10.5 °C measured at the surface.

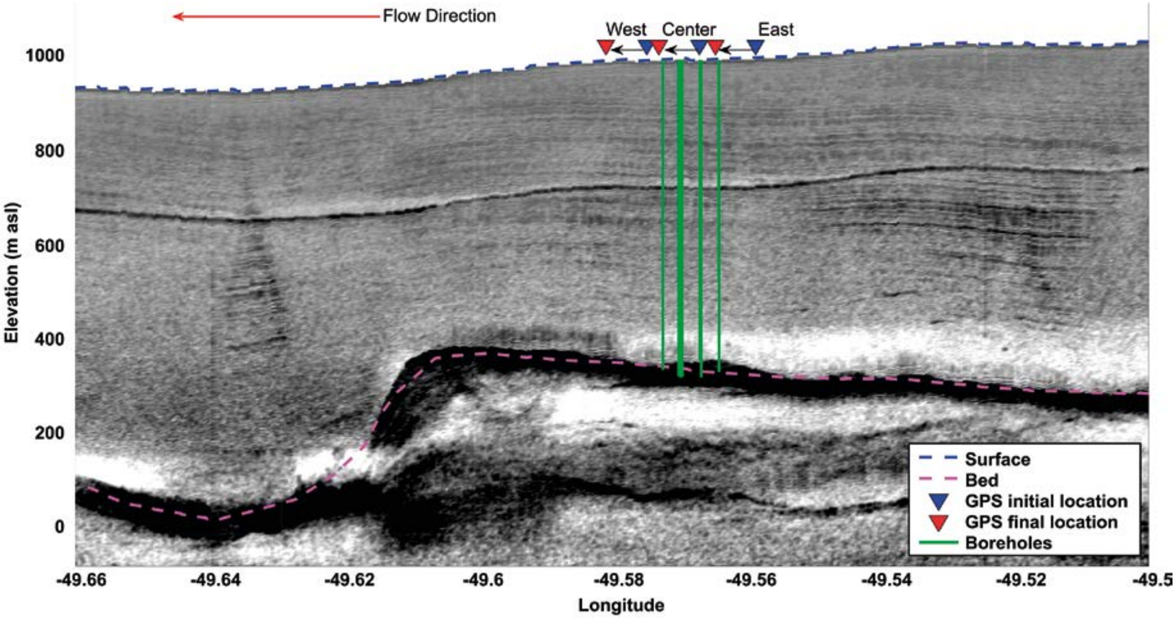

Figure 2-2. *IceBridge radargram passing through the middle of the ICE project block site. Blue triangles show GPS positions on the day of installation, red triangles show GPS positions at the end of the project. Green vertical lines identify locations of boreholes. Dashed magenta line is the IceBridge provided bed pick (Leuschen et al. 2010), illustrating a reverse bedrock slope. Dashed blue line is the IceBridge provided surface elevation profile. Ice flow direction is from right to left.*

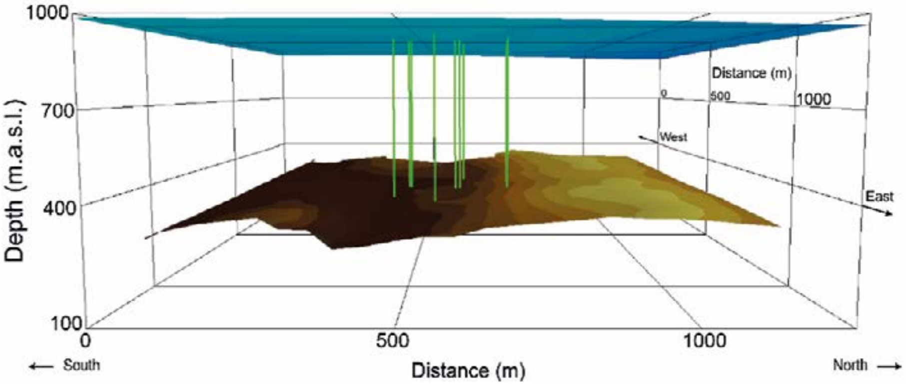

Figure 2-3. *Perspective view of block site boreholes and ice surface and bedrock geometry. Bedrock geometry is interpolated from ground-based radar transects. Surface topography is based on a 2 m DEM from the ArcticDEM initiative (DEM created by the Polar Geospatial Center from DigitalGlobe, Inc. imagery). Ice flow direction is into the page.*

The eleven boreholes drilled during the ICE project build upon the suite of holes drilled during the GAP. Collectively, the two projects yield an instrumented transect consisting of 37 total boreholes, 32 of which penetrate to the ice sheet bed. A summary of all holes drilled between the GAP and the ICE project is provided in Table 2-1. In published manuscripts (Appendices A and B), naming conventions for boreholes and sites were changed to communicate the site distance from the Isunnguata Sermia terminus. These alternate naming conventions are illustrated in Figure 2-1 and provided in Table 2-1.

Table 2-1. Summary of boreholes drilled during the GAP and the ICE projects.

	Site	Hole ID (GAP)	Hole ID (App. A and B)	Drill Date	Latitude (WGS 84)	Longitude (WGS 84)	Elev. (m)	Depth (m)
GAP Boreholes	GL10-1 (M1-10)	GL10-1A		2010-06-12	67.1622	−50.0643	520	98
		GL10-1B		2010-06-13	67.1621	−50.0644	519	92.5
		GL10-1C	M1-10	2010-06-14	67.1625	−50.0633	523	91
		GL10-1D		2010-06-14	61.1624	−50.0633	523	98.5
		GL10-1E		2010-06-16	67.1625	−50.0629	525	91.9
		GL10-1F		2010-06-17	67.1627	−50.0620	532	102
	GL10-2 (M2-10)	GL10-2A	M2-10A	2010-06-20	67.1670	−50.0665	554	144
		GL10-2B	M2-10B	2010-06-21	67.1671	−50.0665	554	148.7
		GL10-2C		2010-06-23	67.1670	−50.0663	555	146.3
		GL10-2D		2010-06-23	67.1671	−50.0662	555	145.6
		GL10-2E		2010-06-25	67.1671	−50.0664	556	148.7
	GL10-3	GL10-3A		2010-06-30	67.1917	−50.0293	618	577.3*
		GL10-3B		2010-07-02	67.1916	−50.0295	619	700.4*
	GL11-1 (27km-11)	GL11-1A	27km-11A	2011-07-02	67.1952	−49.7195	848	457.5
		GL11-1B	27km-11B	2011-07-04	67.1953	−49.7191	850	466
		GL11-1C	27km-11C	2011-07-06	67.1951	−49.7189	849	459.5
	GL11-2 (46km-11)	GL11-2A		2011-07-13	67.2016	−49.2891	1 095	254.5*
		GL11-2B	46km-11A	2011-07-14	67.2014	−49.2888	1 092	821
		GL11-2C		2011-07-17	67.2013	−49.2893	1 087	816
		GL11-2D	46km-11B	2011-07-18	67.2013	−49.2891	1 088	814.5
	GL12-1	GL12-1A		2012-06-07	67.1593	−50.0593	482	116.7
		GL12-1B		2012-06-07	67.1592	−50.0593	479	114.5
	GL12-2 (27km-12)	GL12-2A	27km-12A	2012-06-13	67.2042	−49.7179	849	701.3
		GL12-2B		2012-06-15	67.2040	−49.7179	849	715.3
		GL12-2C	27km-12B	2012-06-17	67.2037	−49.7178	849	691.5
		GL12-2D	27km-12C	2012-06-20	67.2039	−49.7180	849	697.7
ICE Boreholes	Block (33km-14)	14-S-H1	33km-14A	2014-07-17	67.1811	−49.5700	978	674
		14-S-H2		2014-07-19	67.1810	−49.5697	977	677
		14-W-H3	33km-14B	2014-07-22	67.1821	−49.5724	978	661
		14-N-H4		2014-07-26	67.1831	−49.5697	977	641
		14-VS-H5		2014-07-27	67.1827	−49.5696	977	182*
		15-CA		2015-07-06	67.1821	−49.5695	979	671
		15-CB		2015-07-08	67.1820	−49.5695	978	675
		15-S		2015-07-11	67.1809	−49.5667	979	677
		15-EA		2015-07-14	67.1820	−49.5641	980	473*
		15-EB		2015-07-15	67.1819	−49.5640	980	665
		15-N		2015-07-17	67.1831	−49.5669	978	640

* Hole did not reach bed.

3 Summary of ICE findings with respect to objectives

Data and interpretation from GAP subproject B resulted in substantial knowledge gains regarding the physical and hydrological conditions of the ice-bed interface beneath the GrIS (Harper et al. 2016; chapter 4). The findings stem from data and interpretation from the 46 km long transect of boreholes drilled to the ice sheet bed in the GAP study region. Interpretation of new data stemming from the nine boreholes drilled to the bed at the block site during the ICE project, coupled with synthesis of these new results within the context of the original GAP findings, has revealed new characteristics of the subglacial drainage system and advanced its conceptualisation. In some instances, ICE project results have substantiated and refined understanding gained by the GAP, but with greater detail and better quantified evidence. In other instances, ICE project activities yielded new findings which were not explored during the GAP, and contribute to achieving project objectives.

Below, key results from the published studies and manuscript in preparation are summarised. Detailed methods and analyses are presented in the published studies and manuscript in progress, which appear in this report as Appendices A–F.

3.1 Physical conditions of Greenland's bed

From in situ drilling observations and borehole experiments, the preliminary interpretation was that the bed framework at the GAP borehole study sites consisted primarily of bedrock (Harper et al. 2016; section 4.10.1). Borehole drilling during the ICE project expanded the existing GAP dataset by nine boreholes (see Table 2-1), established observations at a new site along the GAP transect, and used new methods and experiments to refine, support, and fully test this interpretation.

Activities and interpretation from the ICE project support the initial GAP conceptualisation. A thin sediment mantle may be present, but observations indicate that any such mantle is discontinuous, and unlikely to exceed decimeters in thickness (Appendix A, Harper et al. 2017). This interpretation is consistently supported by observations at all drilling sites, implying that the 'hard' bed framework is not an anomalous feature in the study area. Nevertheless, field observations at other sites in Greenland's ablation zone, and even at sites within tens of kilometers of the GAP and ICE project drilling sites, have interpreted bed conditions to consist of till with measurable thickness (Booth et al. 2012, Dow et al. 2013, Walter et al. 2014). Moreover, large amounts of sediment emanate from the terminus of Isunnguata Sermia. A plausible hypothesis is that the limited sediment available across the bed is transported into, and concentrated in, deep bedrock troughs. In other words, the rate of transport of basal sediment matches or exceeds the rate of production from erosion processes. Basal troughs then act as line sinks, integrating sediment over large swaths of the ice sheet bed (Figure 3-1). This postulation is supported by hydraulic potential gradients, which favor water routing into deep troughs.

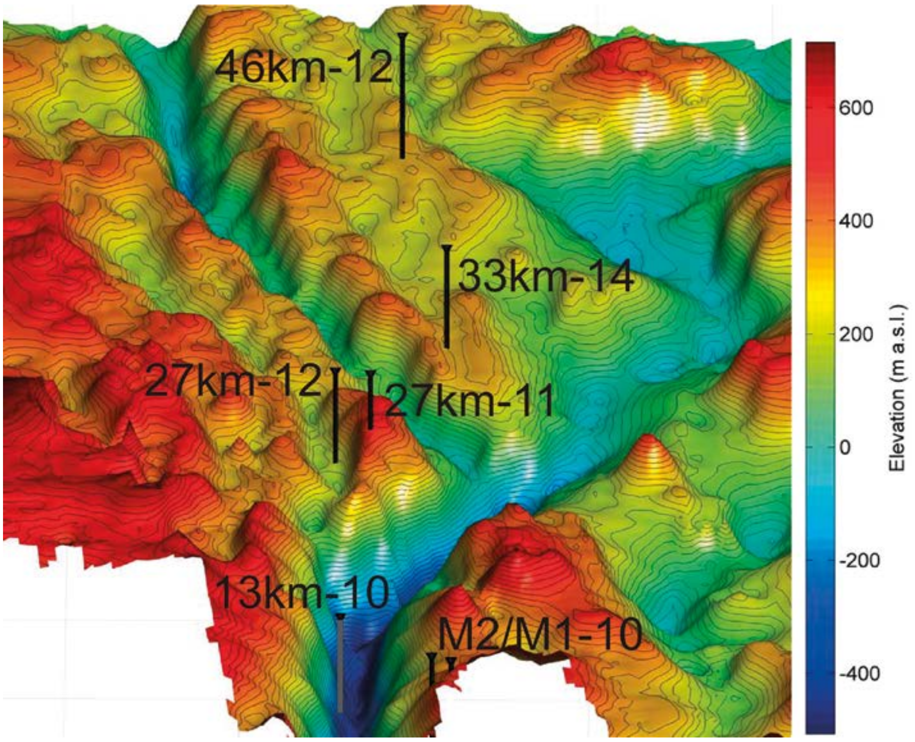

Figure 3-1. *Basal topography over the study reach from the digital elevation model of Lindbäck et al. (2014). Vertical black lines indicate drilling sites, and color bar represents elevation above sea level. Extension of observations indicates that continuous, thick sediment packages are unlikely at higher bed elevations, such as those represented at drill sites. However, hydraulic transport of limited sediment over large areas of the bed into sparse bedrock troughs may yield abundant sediment at trough bottoms. Figure from Harper et al. (2017).*

3.2 Pressure in the subglacial drainage system

Direct borehole observations of basal water pressure conditions have yielded datasets that are distilled into four key findings relevant to the project objectives.

1. Pressure is consistently high, and confined to a limited range

Outcomes from the GAP project revealed that high pressure near overburden is an adequate assumption for the pressure regime at the ice sheet basal boundary (Harper et al. 2016; section 4.10.2). Pressure data from new boreholes drilled during the ICE project have expanded the basal pressure dataset, and support the findings from the GAP. Furthermore, synthesis of all pressure data collected on the GrIS has further refined the initial GAP result to a deeper level of understanding of conditions.

The collective pressure data from both the ICE project and GAP reveal that basal drainage system pressures are confined to a limited range between 0.8–1.1 as a fraction of local ice overburden pressure (Figure 3-2), (Appendix B, Wright et al. 2016). In addition to the pressure measurements from the ICE project and GAP, we are aware of measurements in a total of 24 other boreholes at sites around Western Greenland's ablation zone (Andrews et al. 2014, Iken et al. 1993, Lüthi et al. 2002, Thomsen and Olesen 1990, 1991, Thomsen et al. 1991, van de Wal et al. 2015) (see Appendix B, Table B-2). These measurements span a wide range of possible conditions: ice thickness ranges from 180 m (Thomsen and Olesen 1990, Thomsen et al. 1991) to a maximum of 1 600 m in the trough of Jakobshavn Isbrae (Iken et al. 1993), and on a basal substrate which has, in some cases, been interpreted to consist of thick till (Walter et al. 2014). Whereas the GAP and ICE project datasets include multiple records that extend for more than one year, the other records generally span shorter time periods. Importantly, in all cases, the pressures measured in the past decades are within the confined range established by the ICE and GAP projects.

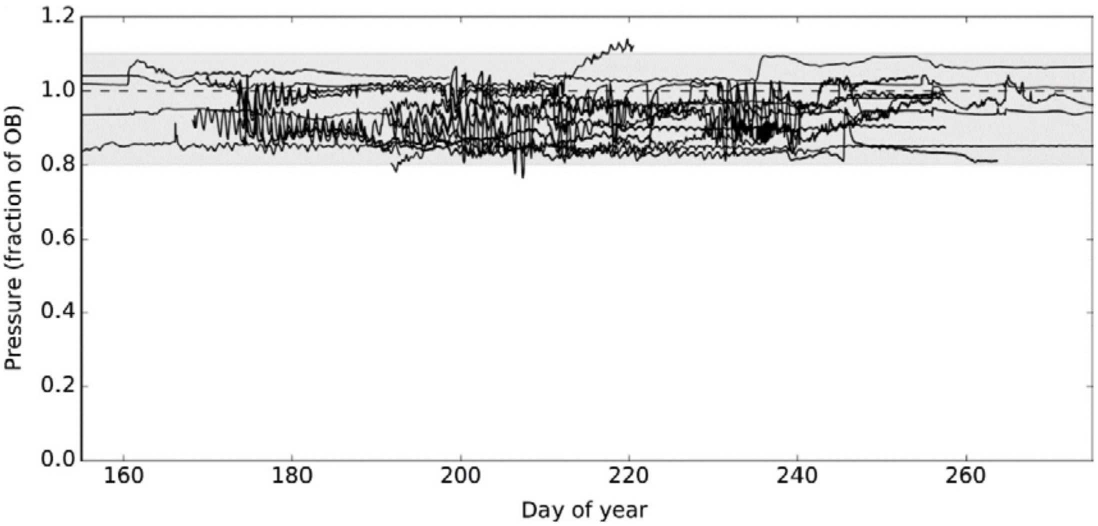

Figure 3-2. Melt season basal pressure records from 12 boreholes drilled during the ICE project and GAP through ice ranging from 150 to >800 m in thickness. The shaded region essentially brackets the measured range of pressures, which are confined to 0.8–1.1 as a fraction of local ice overburden. Figure from Wright et al. (2016).

2. Basal pressure undergoes daily to seasonal changes

The GAP established that basal pressures are highly variable over time scales ranging from daily to seasonal (Harper et al. 2016; section 4.4.3). Observations and modeling demonstrated that the seasonal growth of conduits from the margin toward the ice sheet interior is limited by two dampening processes: 1) the conduit closure rate increases as the ice becomes thicker, and 2) the melting power of flowing water is reduced as the surface slope decreases. In the study region, the seasonal growth of a discrete conduit network is limited in extent to about 20 km inward from the ice edge. New pressure results from the ICE project, spanning summer melt and winter seasons at the block site, support GAP findings.

The suite of measurements from the ICE project and GAP illustrates that basal water pressure undergoes distinct seasonal phases (Figure 3-3), (Appendix B, Wright et al. 2016). Higher frequency diurnal variations are common during the summer melt season. The magnitude and character of diurnal variations is highly variable across the drainage system. The lowest pressures from annual records are typically observed during the summer diurnal period. Diurnal pressure variations are commonly associated with active drainage system processes (e.g. Andrews et al. 2014); this is supported by the observation of diurnal variability during the melt season, but concurrent dye and pressure measurements also indicate that small diurnal pressure variations may arise in the absence of water flow (Appendix D, Meierbachtol et al. 2016b). The emerging picture is that active drainage system and ice flow responses to variations in surface melt input force pressure variations over short time periods that are spatially extensive across the bed. However, even the largest measured diurnal pressure variations are confined to the limited range described above. Moreover, because low basal pressure during the melt season diurnal period only persists for a small fraction of the day, and is often offset by a high pressure peak, the median melt season pressure is very similar to the winter median pressure (Appendix B, Wright et al. 2016).

3. Potential gradients at the ice sheet bed arise from drainage system processes over short length scales

The high basal pressures measured consistently in the GAP allowed for the quantification of long length scale (ice sheet scale) potential hydraulic gradients, which arise from both the ice sheet surface and bed geometries: an average potential gradient of ~115 kPa/km was found across the study transect. Both higher and lower values were measured across shorter length scales of 10 km or less, due to local variability in basal topography and ice thickness. The relatively high relief of basal topography within 10s of km from the ice margin results in hydraulic potential gradients with strong deviations from the overall ice sheet mean when computed over length scales of a few km. Note that such high relief topography is not characteristic of any proposed DGR site.

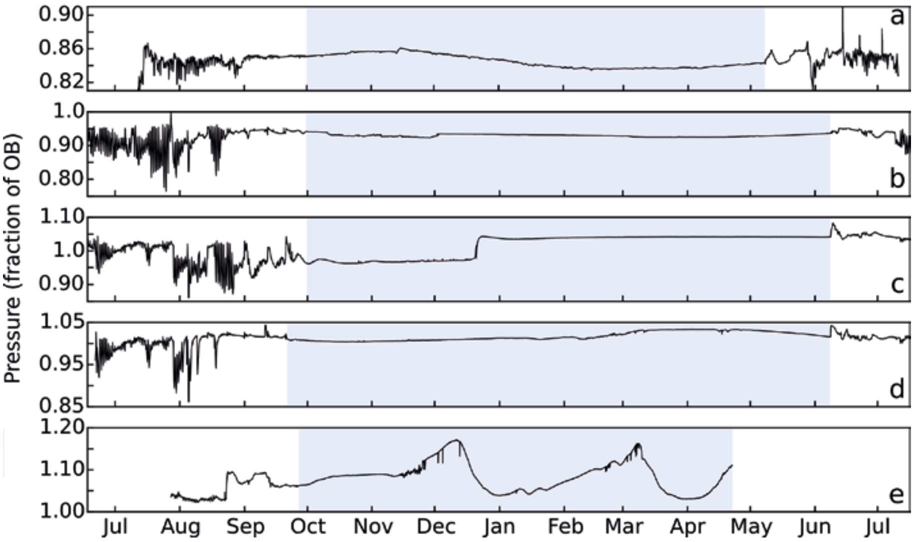

Figure 3-3. *Pressure records in boreholes 27km-11A (a), 27km-12A (b), 27km-12B (c), 27km-12C (d), and 33km-14B (e), displaying pressure variability over diurnal to seasonal time scales. Data span different years of measurement. Y-axis scales are different between panels to elucidate pressure variability in each borehole. Characteristic winter period, based on pressure variability, is shaded in blue. Figure adapted from Wright et al. (2016).*

Superimposed on topographically-driven potential gradients are pressure gradients arising from local drainage system processes. Pressures measured at the site scale (10s of meters) identify the possibility that such gradients can be large. However, quantification of local gradients in the basal drainage system is complicated by the unknown sinuosity of drainage elements along the bed. The drainage network consists of discrete and complex pathways, and whether two geographic locations on the bed are hydraulically connected via a straight line or a complex and highly sinuous pathway remains unconstrained. Confident quantification of the pressure gradients arising from drainage system processes awaits a fuller understanding of the geometry and dynamics of the basal flow system. Consequently, because the local gradients calculated (reaching 20 kPa/m) (Figure 3-4) are done so using a straight-line assumption, these should be viewed as an end-member maximum in the subglacial drainage system. Nevertheless, the observations illustrate that such gradients are present along the upper groundwater system boundary.

4. Short duration basal pressure transients are uncommon and spatially localised

Identification of short duration pressure transients in the basal drainage system was not a scientific objective of the GAP; therefore, instrumentation was not developed for such an investigation as part of this earlier program.

Measurements of basal water pressure at high frequency during the ICE project identified rapid pressure pulses to be exceedingly rare (Figure 3-5), (Appendix C, Meierbachtol et al. 2018). Five pulses were measured in a dataset containing nearly 49 million measurements from two boreholes located 180 m apart. Measured pulses all occurred as pressure drops and, critically, were spatially localised. Extension of the measured high frequency pressure dataset to the broader basal system is hindered by an incomplete understanding of the potential cause(s) of the few measured pulses. Multiple processes could lead to such behavior, and the pressure records alone are insufficient to fully constrain potential causal mechanisms. Nevertheless, the dataset indicates that potential mechanisms are localised, yielding a pressure response that is spatially restricted at the bed.

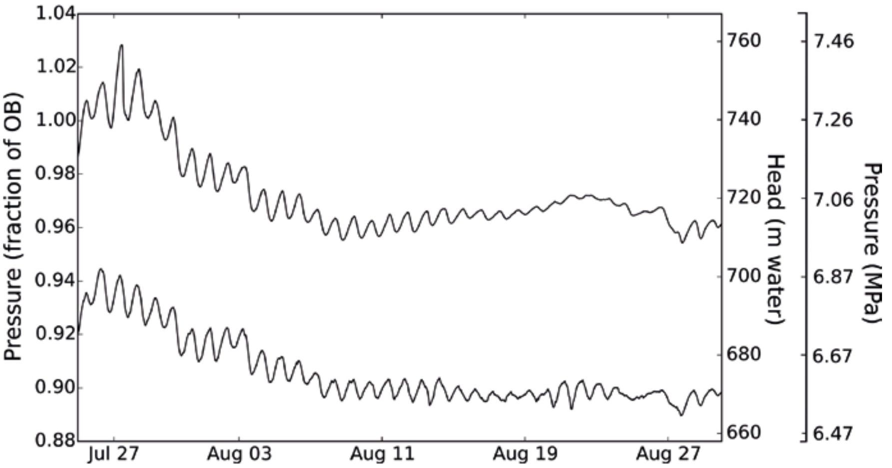

Figure 3-4. *Basal pressure records from two boreholes 20 meters apart. Both boreholes illustrate diurnal pressure variations that imply a degree of hydraulic connectivity and connection to an active drainage system, but pressures are offset by approximately 40 m. Ice thickness differs by no more than 6 m between the boreholes, meaning that the gradient can only be attributed to drainage system processes. Given the assumption of a straight line connection between boreholes, the gradient is approximately 20 kPa/m. Figure from Wright et al. (2016).*

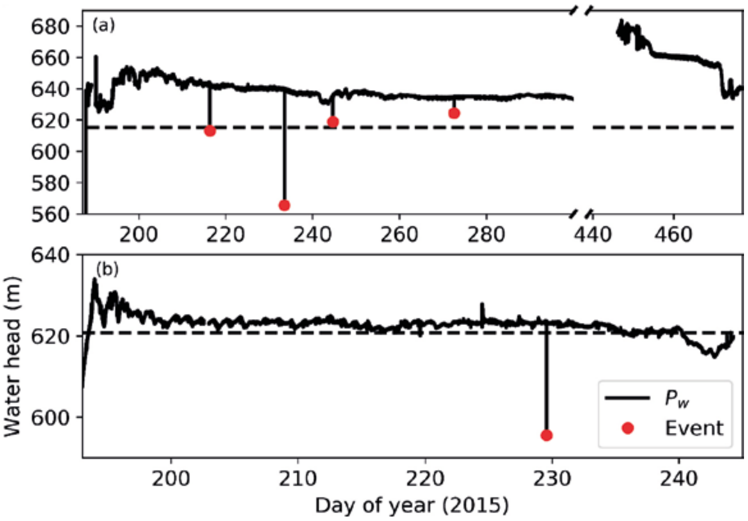

Figure 3-5. *Basal pressure records, measured at 4 Hz frequency, in two boreholes 180 meters apart. Red dots indicate identified short duration (<1 minute) pressure transients. Note the differing x- and y-axis scales. Figure from Meierbachtol et al. (2018).*

3.3 Characteristics of the subglacial drainage system

Observations and analysis lead to five key findings concerning the drainage system.

1. The entire ablation zone is forced by surface meltwater

Analysis of ice sheet geometry and surface speed for a study area extending nearly to the ice sheet divide in the western part of the GrIS, and including the ICE project and GAP study sites, shows a decline in gravitational driving stress that is correlative with an increase in surface speed at the long term equilibirum line altitude (ELA) (Appendix F, Meierbachtol et al. 2016a). This behavior requires an increase in ice sheet sliding, which is interpreted to result from an increase in water at the bed arising from the introduction of surface melt. This interpretation is supported by the inland limit of: a) observed surface lake drainage events (Fitzpatrick et al. 2014), and b) surface speed conditions that are believed to facilitate crevassing, and therefore provide a meltwater transport pathway from the surface to the bed (Poinar et al. 2015). These collective findings imply that essentially the entire ablation zone is covered by water, and that surface meltwater that drains to the bed near the ELA is capable of residing over winter.

2. The basal drainage system is capable of dynamic routing

The GAP and the ICE project results have identified potential gradients over varying length scales. The magnitude of the potential gradients vary depending on the length scale of interest, owing to the substantial ice surface and basal topography in the ablation zone across the study area.

From analysis of pressure records, and leveraging a high resolution DEM created with GAP support (Lindbäck et al. 2014), the ICE project revealed that different locations on the bed undergo sub annual changes in the direction and magnitude of the hydraulic potential in response to water pressure fluctuations. The hydraulic potential of the subglacial water layer is a function of the sloping ice surface and bed topography, and pressure gradients within the water layer. Water pressure gradients result from changing ice overburden due to changes in ice thickness, and in addition, the development of a subglacial drainage system which can, in itself, lead to pressure gradients on the bed. While regional-scale ice thickness does not change on annual time scales, the basal water pressure does change as the drainage system undergoes diurnal and seasonal forcing. The pressure gradients from this forcing can lead to spatially-variable and time-change basal water pressure fluctuations (Appendix B, Wright et al. 2016). The water pressure variations, therefore, result in a time-space evolving potential gradient field that may be capable of promoting dynamic drainage system connectivity (Figure 3-6).

The effect of this process is amplified where bed topography slopes steeply, is oblique to the ice surface slope, and where water pressure varies around a baseline that is a high fraction of ice overburden. These conditions are satisfied over large reaches of the GAP/ICE study area, particularly during the melt season when diurnal pressure variations are commonly measured.

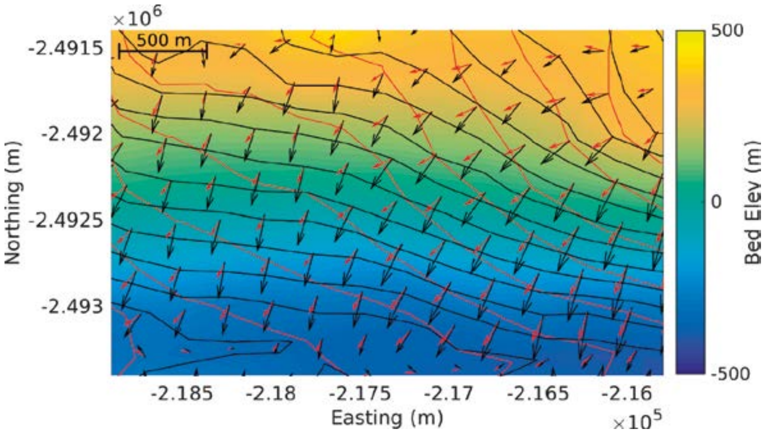

Figure 3-6. *Example of plausible changes in the magnitude and direction of the hydraulic potential gradient field arising from two different basal water pressure scenarios. Contours illustrate the hydraulic potential field, and arrows identify the magnitude and direction of hydraulic potential gradients. Red and black colors show hydraulic potential and gradients under high pressure (0.99 as a fraction of ice overburden) and low pressure (0.87 as a fraction of ice overburden) scenarios, respectively. Background color map illustrates bed elevation. Ice sheet surface slopes from right to left. The particular setting reflects the steep north wall of the Isunnguata Sermia outlet trough. Pressure scenarios are selected based on the diurnal pressure range measured in ICE project and GAP boreholes. Figure adapted from Wright et al. (2016).*

3. The basal drainage system is composed of discrete elements with variable transmissivity

The outcomes of drilling breakthrough tests, slug testing, and pumping tests in ice-sheet boreholes during the GAP indicated that water flow along the ice sheet bed in the study area occurs through discrete drainage elements with variable transmissivity. Clear hydraulic connections were observed between boreholes 10s of meters apart, while connections were completely absent in others. The accommodation of a substantial water volume in response to borehole drainage during drilling (nearly 2 m^3, assuming a borehole radius of nearly 7 cm) in less than 200 seconds indicated connection to a drainage system with substantial capacity (Figure 3-7). Outcomes of the ICE project support these early GAP findings. Moreover, quantification of the volume of an isolated water pocket (1–7 m^3) from in situ dye tracing indicates that disconnected cavities exist in measurable volumes and may cover substantial regions of the bed (Appendix D, Meierbachtol et al. 2016b).

4. Connectivity between drainage elements is prone to spontaneous change

The results from repeat slug testing and pumping tests during the GAP indicated that the transmissivity of discrete basal drainage system elements was capable of undergoing rapid change in response to a flow perturbation (Harper et al. 2016; section 4.3). These results were supported by additional dye tracing experiments during the ICE project (Appendix D, Meierbachtol et al. 2016b). Measurement of dye disappearance over the course of one hour (Figure 3-8) illustrates the dynamic nature of connections between drainage elements at the ice sheet bed.

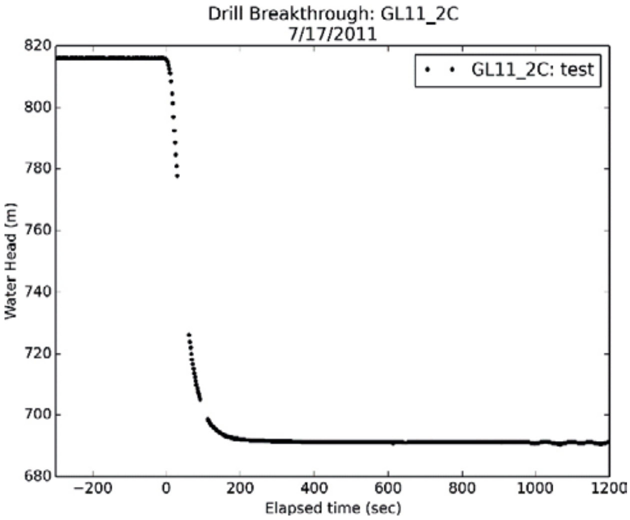

Figure 3-7. Drilling breakthrough curve illustrating a drop in borehole water level of 124 m over less than 200 seconds in response to borehole intersection with the bed.

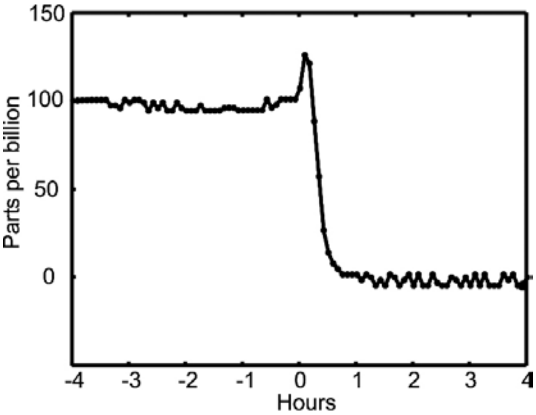

Figure 3-8. Dye concentration time series in an isolated basal cavity. Dye disappearance over the course of an hour is interpreted to reflect establishment of a connection between the isolated cavity and active drainage system, and evacuation of 1–7 m^3 of dyed water. Figure from Meierbachtol et al. (2016b).

5. Calculation of basal water storage changes from surface elevation measurements is confounded by ice flow

The dense instrumentation network at the ICE project study site permitted quantification of basal sliding velocity and englacial strain rates, two variables that are central to estimating changes in basal water storage from measurements of surface elevation change (Appendix E). Preliminary results from 2016 demonstrated that vertical strain varies substantially with depth, and is of first order importance in computing basal water storage. As a result, estimates of basal storage change are extremely sensitive to the depth interval over which vertical strain in the ice column is averaged. Any studies that have assumed the vertical strain at the ice surface is constant throughout the entire ice thickness (e.g. Andrews 2014, 2018, Howat 2008, Hoffman 2011) should be interpreted with caution. At present, a more confident estimate of basal storage at the ICE project site awaits integration of additional data for the 2016 melt season.

4 Implications for safety assessment of deep geologic repositories

Deep geological repositories (DGRs) for spent nuclear fuel must be designed to sequester the radioactivity for long time intervals, ranging from intervals similar in length to recent glacial/interglacial cycles (tens of thousands of years) up to a million years. Thus, safety assessments for repositories to be located in places known to be periodically covered by ice must consider the potential impacts of future glaciations. As ice sheets advance and retreat over an ice age cycle, the surface boundary of the geosphere undergoes climate and hydrological change that may or may not impact conditions at proposed repository depths. An important component of safety assessments for DGRs is an extensive exploration of these conditions, using numerical simulations, of climate and hydrological change.

Numerical models of earth systems commonly require simplifications, parameterisations, and assumptions due to complex and sometimes poorly understood processes. The difficulties in making direct measurements and observations beneath ice sheets has impeded advancements in conceptual understanding of processes at the earth/ice boundary that govern underlying groundwater flow. Consequently, numerical simulations of groundwater flow beneath ice sheets have coupled the two systems with boundary conditions that are oversimplified and with limited observational or theoretical bases (e.g. Person et al. 2012). Further, ice sheet-groundwater interactions have not been an intensive focus area for the fields of glaciology or groundwater – it has primarily been of interest to the community concerned with repository safety assessment. Thus, models employed for safety assessments inherently have uncertainties, and may have particular aspects with low confidence. The GAP and the ICE project utilised the GrIS's basal boundary to gain perspective, context and understanding for more representative modeling of ice sheet-groundwater interactions.

The importance of all ICE project findings to DGR safety assessment stem from improved understanding of the ice sheet basal boundary. The overarching goal of the work was to gain new understanding and constraints, which will facilitate 1) the reduction of simplifications, 2) the use of fewer assumptions, and 3) improved parameterisation in numerical simulations of ice sheet interactions with groundwater. These goals were achieved through four specific objectives, which facilitated an advanced conceptualisation of the ice sheet basal boundary (Section 4.1) and also resulted in the development of critical constraints for key elements of the basal boundary that can be employed in models (Section 4.2).

4.1 Conceptual understanding of the ice sheet bed

The ICE project activities were framed around four objectives designed to advance the conceptualisation of the ice sheet bed, and test and build upon the understanding developed during the GAP. The ICE project produced no results that challenge or overturn the conceptualisation formed during the GAP (Claesson Liljedahl et al. 2016; section 5.1). Many of the scientific findings used to formulate the GAP conceptual model of the subglacial drainage system have been supported by additional information and more detailed analysis of the GAP data. Below, the findings from the ICE project are cast within the framework of the project objectives.

Objective 1) Build a physical framework of basal conditions

The framework of the basal boundary over the ICE project and GAP study areas is hard bedrock with a relatively thin and discontinuous veneer of sediment (Appendix A). It is likely, however, that the deep troughs which cross the study area act as sediment sinks and route sediment to glacier outlets. These troughs may be underlain by thick sediment. Elsewhere on the ice sheet, sediment has been estimated to be many tens of meters thick (Walter et al. 2014). While the hard bed setting provides a framework for interpretation of the ICE project and GAP observations, a spectrum of basal conditions is possible. Mixed hard bedrock and thick sediment-covered basal conditions are likely to be present over spatial scales of kilometers (and plausibly smaller).

Objective 2) Quantify water pressure and spatial gradients at the bed

Pressure Magnitude: Despite the remarkable differences in possible basal frameworks, all existing field observations, from this project and others, and spanning variable conditions and locations across Greenland, demonstrate a consistent range of water pressures that vary between 0.8 and 1.1 of the ice overburden pressure (Appendix B).

If pressures greater than overburden persisted over large spatial scales (e.g. an ice thickness), widespread jacking, flotation, and unstable ice sheet sliding would likely ensue. Such conditions may be possible in response to an event, such as the sudden introduction of water to the bed from supraglacial lake drainage, but observations of ice dynamic response to lake drainages imply such events would be highly transient, lasting no longer than a few days (e.g. Das et al. 2008, Doyle et al. 2013). Over longer time scales, water pressure persisting above ice overburden may be plausible over localised regions of the ice bed, such as may occur from the increased stress induced by ice flow against the stoss side of steep bedrock bumps (e.g. Weertman 1957). This is the most likely explanation for the high pressures measured in the GAP, ICE project and other borehole studies.

Pressure measurements were all made in the ablation zone. No measurements of pressure have been made deep in the ice sheet interior, where melted bed conditions are likely to exist (Harper et al. 2016, MacGregor et al. 2016) but there is no surface melt forcing. Owing to thick ice, which would facilitate rapid creep closure of any basal cavity at low pressure, and the likely absence of varying water flux, basal water pressures in the interior region are likely to reside in a range that is even closer to ice overburden pressure than measurements reveal from locations within the ablation zone. The possibility of basal pressure greater than ice overburden still exists, but because there is no surface melt input, any possible overpressure at the bed is likely to arise from localised processes, such as the ice flow mechanism described above. In the case of a stress perturbation from ice flow against a bedrock feature, the magnitude of the stress perturbation does not scale with the overlying ice pressure but, rather, scales with the basal shear stress at the bed that the feature must support (Weertman 1957). Hence, in this particular instance the magnitude of the pressure increase is not expected to scale with overburden ice pressure. In other words, there is no physical justification as to why maximum pressures (i.e. pressure above overburden), even if localised, should scale with ice overburden pressure in the ice sheet interior, despite ice thicknesses that are a factor of 2 or 3 greater than in the ablation zone.

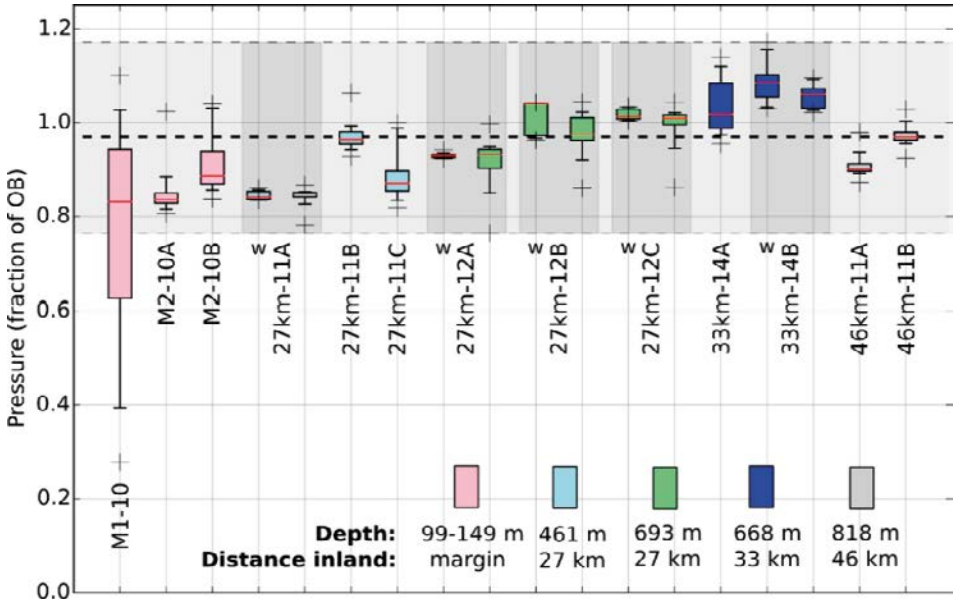

Figure 4-1. *Box plots of basal water pressure data for all boreholes from GAP and the ICE project (see Appendix B). For boreholes with over-winter records, corresponding winter and melt season periods are shown in shaded pairs, where winter records are indicated with "w". For boreholes with only melt season records, all data in the record are represented. Box center lines are median, boxes span the 1st and 3rd quartiles, whiskers extend to 5th and 95th percentiles, and crosses indicate max and min points. Bold dashed line is the weighted annual mean for the 12-borehole suite. Shaded region spans the minimum and maximum values of the 12-borehole suite. Figure from Wright et al. (2016).*

The drainage system differences between measurement locations, and the differences between summer melt season and winter seasons, do not ultimately impact the median water pressure averaged over annual time steps (Figure 4-1, Appendix B). This is because diurnal and seasonal swings between higher and lower pressures average away over longer time periods.

Pressure Gradients: The studied drainage system is capable of maintaining large pressure gradients between two geographic locations at the bed. For example, gradients such as 20 kPa/m have been measured (Appendix B). These gradients are likely possible where nearby points on the bed are connected by a water pathway that is very long.

The structure of the drainage system and its tendency to undergo dynamic changes, leads to an essentially unpredictable range of possible pressure values and gradients between specific locations at any given time. However, this range does not encompass all possible values and has relatively narrow bands in the ablation zone (0.8–1.1 of overburden) (Figure 4-1, Appendix B).

Because the water pressure field is primarily linked to ice thickness, it demonstrates strong variability in the horizontal direction. Values of hydraulic potential, however, are a function of both ice thickness and bed elevation, and undergo far smoother changes along the length of the ice sheet (Figure 4-2, Appendix B).

Objective 3) Measure the presence or absence of short duration pressure transients in the drainage system

Outcomes of ICE project activities identified rare pressure transients at the ice sheet bed, and none of the measured events were transmitted between boreholes. If two points on the bed less than 200 m apart do not experience a common event, it is implausible that an event could impact a location at repository depth of 500 m.

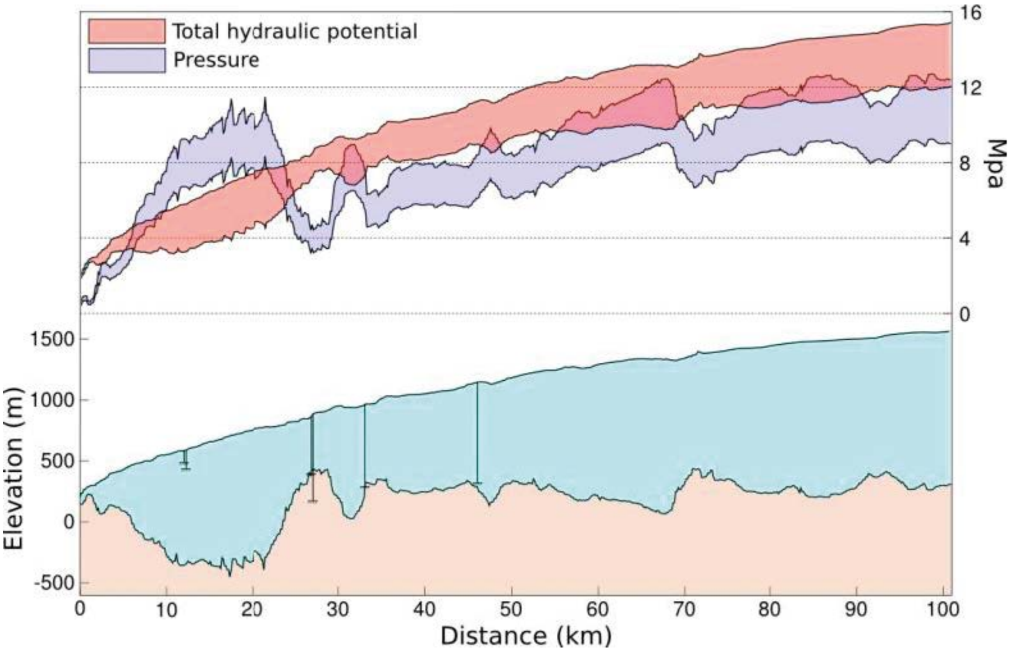

Figure 4-2. *Basal water pressure and total hydraulic potential along the transect through the GAP/ICE project study region which extends to 100 km inland (see Appendix B). Ice surface and bed topography along the profile are shown for context, and borehole locations and depths have been projected into the plane of the profile. Shaded band for water pressure (blue) is derived from ice thickness and measured borehole water pressures, ranging from 0.8–1.1 as a fraction of ice overburden. Total hydraulic potential (red) includes basal water pressure and elevation potential from bedrock topography. Gradients in total hydraulic potential, therefore, reflect changes in ice thickness and bed elevation, combined with local water pressure gradients that stem from basal processes. Figure from Wright et al. (2016).*

The lack of spatially extensive pressure pulses at the ICE project block site does not necessarily preclude the possibility that such events occur in the ice sheet setting. A widespread 'event' has been observed on an alpine glacier that was sufficient to cause borehole instrumentation failure (Kavanaugh and Clarke 2001). There are presently no data to suggest that similar events are not possible beneath ice sheets. However, pressure data collected during the ICE project confirms that such events are uncommon at the time scale of this study (i.e. over several years).

Objective 4) Advance the conceptualisation of water distribution at the ice sheet bed

At the regional scale, indirect evidence suggests surface meltwater reaches the bed across the ablation zone, and could reside over winter (Appendix F). The quantity of water at the bed during the winter and over large regions, thus, has the potential to be far greater than that supplied by basal melting alone.

Locally, water pathways in the studied basal drainage system are highly dynamic (Appendix D). Rapid sliding makes individual pathways unstable, cavities move in and out of connection and efficiency, and the hydraulic potential gradient is capable of magnitude changes and direction rotations in response to changing water pressure. This implies that copious amounts of water likely have access to essentially all regions of the ice sheet bed in the ablation zone. Measurement of changes in the volume of this water from observations of surface elevation change (from GPS stations), however, is unreliable (Appendix E). This owes to depth variations in internal deformation that can cause significant changes in surface elevation and cannot be accounted for by ice flow thinning or thickening alone. Thus, existing works using surface measurements of velocity and elevation alone to predict basal water storage changes should not be heavily factored in conceptual models of subglacial drainage evolution.

4.2 Key findings for modeling the DGR boundary condition

The findings of this work have implications for modeling assessments of long term DGR safety under ice sheet conditions. The information that will be required for modeling endeavors in the distant future cannot be known; only the present paradigm and most plausible modeling questions and methodologies can be considered. For current models, two important elements of DGR design and safety assessment are assumed in order to constrain the scope of glaciological information required: (1) DGRs are to be located deep (100s of meters) below the ice sheet basal boundary, and (2) the relevant time scale associated with change in the ice sheet boundary condition is long (i.e. >10 000 years). Adopting these assumptions, the findings of the ICE project provide the following generalisations which may guide DGR safety assessment modeling of ice sheet conditions.

1. The distribution of water at the basal boundary.

   The basal boundary across the entire ablation zone should be considered to have liquid water at the bed. This conclusion was reached in the GAP report based on borehole observations, modeling, and surface observations. The ICE project has further supported this conclusion by an independent and broader geographic analysis of ice sheet geometry and basal sliding (Appendix F).

2. The representation of basal water pressure.

   A. *Representative values*. Ice overburden pressure is the most reasonable representation of basal water pressure as a constant value. However, the mean pressure could likely vary between 0.8 to 1.1 of ice overburden (Appendix B). This result appears to be true regardless of hard bed or sediment covered basal frameworks (Appendix A, Appendix B).
   Basal pressures exceeding ice overburden over the long temporal and spatial scales associated with numerical simulations of glacial cycles, however, are most likely untenable. This is also likely to be true deep in the ice sheet interior. Therefore, while modeling may consider the range of pressures to assess sensitivity to the spectrum of measured conditions, an upper end member of local ice overburden pressure is probably appropriate.

B. *Mechanically induced pressure*. While evidence exists for mechanical pressure forcing on basal water bodies due to ice flow, the resulting pressure variations do not appear to be large deviations from background (Appendix D).

C. *Transient pressures*. Rare, high frequency pressure transients have been identified in Greenland (Appendix C). Despite their occurrence, events are highly localised, implying that they are unimportant to conditions at repository depth.

D. *Pressure gradients*. While pressure gradients occur over a range of shorter length scales – between individual cavities in the form of mechanical oscillations (Appendix D) or pulses (Appendix C), and over 10s of meters in the discrete subglacial drainage system (Appendix B) – only the long length scale gradients due to changing ice thickness (Appendix B) should be relevant to regional groundwater flow. Furthermore, the mechanical and drainage system processes which drive observed gradients over short length scales arise from seasonal melt forcing and are therefore highly transient. Over time scales greater than one year, such short length scale variations should not persist at any given location, and are expected to average away (e.g. Appendix B). The mechanically induced pressure, as described in 2B above, is the most relevant pressure boundary condition to regional groundwater flow beneath ice sheets.

Acknowledgment

Field and project assistance

Joel Brown, Ph.D., Aesir LCC.

Caitlyn Florentine, Ph.D. Candidate, University of Montana.

Joel Harrington, M.S. Candidate, University of Wyoming.

Ben Hills, M.S. Candidate, University of Montana.

Rosie Leone, M.S. Candidate, University of Montana.

Ian McDowell, M.S. Candidate, University of Wyoming.

Nate Maier, Ph.D. Candidate, University of Wyoming.

Aaron St. George, B.S. Candidate, University of Montana.

Aidan Stansberry, B.S. Candidate, University of Montana.

Patrick Wright, M.S. Candidate, University of Montana.

Urs H. Fischer, Project Manager, Nagra.

References

Andrews L C, Catania G A, Hoffman M J, Gulley J D, Lüthi M P, Ryser C, Hawley R L, Neumann T A, 2014. Direct observations of evolving subglacial drainage beneath the Greenland Ice Sheet. Nature 514, 80–83.

Andrews L C, Hoffman M J, Neumann T A, Ginny A, Lüthi M P, Hawley R L, Schild K M, Ryser C, Morriss B F, 2018. Seasonal evolution of the subglacial hydrologic system modified by supraglacial lake drainage in western Greenland. Journal of Geophysical Research: Earth Surface 123, 1479–1496.

Bamber J L, Griggs J A, Hurkmans R T W L, Dowdeswell J A, Gogineni S P, Howat I, Mouginot J, Paden J, Palmer S, Rignot E, Steinhage D, 2013. A new bed elevation dataset for Greenland. The Cryosphere 7, 499–510.

Booth A D, Clark R A, Kulessa B, Murray T, Carter J, Doyle S, Hubbard A, 2012. Thin-layer effects in glaciological seismic amplitude-versus-angle (AVA) analysis: Implications for characterising a subglacial till unit, Russell Glacier, West Greenland. The Cryosphere 6, 909–922.

Claesson Liljedahl L, Lehtinen A, Harper J, Näslund J-O, Selroos J-O, Pitkänen P, Puigdomenech I, Hobbs M, Follin S, Hirschorn S, Jansson P, Järvinen H, Kennell L, Marcos N, Ruskeeniemi T, Tullborg E-L, Vidstrand P, 2016. Greenland Analogue Project: Final Report. SKB TR-14-13, Svensk Kärnbränslehantering AB.

Das S B, Joughin I, Behn M D, Howat I M, King M A, Lizarralde D, Bhatia M P, 2008. Fracture propagation to the base of the Greenland Ice Sheet during supraglacial lake drainage. Science 320, 778–781.

Dow C F, Hubbard A, Booth A D, Doyle S H, Gusmeroli A, Kulessa B, 2013. Seismic evidence of mechanically weak sediments underlying Russell Glacier, West Greenland. Annals of Glaciology 54, 135–141.

Doyle S H, Hubbard A L, Dow C F, Jones G A, Fitzpatrick A, Gusmeroli A, Kulessa B, Lindbäck K, Pettersson R, Box J E, 2013. Ice tectonic deformation during the rapid in situ drainage of a supraglacial lake on the Greenland Ice Sheet. The Cryosphere 7, 129–140.

Fitzpatrick A A W, Hubbard A L, Box J E, Quincey D J, van As D, Mikkelsen A P B, Doyle S H, Dow C F, Hasholt B, Jones G A, 2014. A decade (2002–2012) of supraglacial lake volume estimates across Russell Glacier, West Greenland. The Cryosphere 8, 107–121.

Harper J, Hubbard A, Ruskeeniemi T, L C L, Kontula A, Hobbs M, Brown J, Dirkson A, Dow C, Doyle S, Drake H, Engström J, Fitzpatrick A, Follin S, Frape S, 2016. The Greenland Analogue Project : Data and Processes. SKB R-14-13, Svensk Kärnbränslehantering AB.

Harper J T, Humphrey N F, Meierbachtol T W, Graly J A, Fischer U H, 2017. Borehole measurements indicate hard bed conditions, Kangerlussuaq sector, western Greenland Ice Sheet. Journal of Geophysical Research: Earth Surface 122, 1605–1618.

Hills B H, Harper J T, Humphrey N F, Meierbachtol T W, 2017. Measured horizontal temperature gradients constrain heat transfer mechanisms in Greenland ice. Geophysical Research Letters 44, 9778–9785.

Hoffman M J, Catania G A, Neumann T A, Andrews L C, Rumrill J A, 2011. Links between acceleration, melting, and supraglacial lake drainage of the western Greenland Ice Sheet. Journal of Geophysical Research 116, F04035. doi:10.1029/2010JF001934

Howat I M, Tulaczyk S, Waddington E, Björnsson H, 2008. Dynamic controls on glacier basal motion inferred from surface ice motion. Journal of Geophysical Research: Earth Surface 113, F03015. doi:10.1029/2007JF000925

Iken A, Echelmeyer K, Harrison W, Funk M, 1993. Mechanisms of fast flow in Jakobshavns Isbrae, West Greenland: Part I. Measurements of temperature and water level in deep boreholes. Journal of Glaciology 39, 15–25.

Kavanaugh J L, 2009. Exploring glacier dynamics with subglacial water pressure pulses: Evidence for self-organized criticality? Journal of Geophysical Research: Earth Surface 114, F01021. doi:10.1029/2008JF001036

Kavanaugh J L, Clarke G K C, 2000. Evidence for extreme pressure pulses in the subglacial water system. Journal of Glaciology 46, 206–212.

Kavanaugh J L, Clarke G K C, 2001. Abrupt glacier motion and reorganization of basal shear stress following the establishment of a connected drainage system. Journal of Glaciology 47, 472–480.

Leuschen C, Gogineni P, Rodriguez-Morales F, Paden J, Allen C, 2010. IceBridge MCoRDS L2 Ice Thickness, Version 1. Boulder, CO USA: NASA DAAC: NASA DAAC at National Snow and Ice Data Center: NASA National Snow and Ice Data Center Distributed Active Archive Center. doi:10.5067/GDQ0CUCVTE2Q

Lindbäck K, Pettersson R, Doyle S H, Helanow C, Jansson P, Kristensen S S, Stenseng L, Forsberg R, Hubbard A L, 2014. High-resolution ice thickness and bed topography of a land-terminating section of the Greenland Ice Sheet. Earth System Science Data 6, 331–338.

Lüthi M, Funk M, Iken A, Gogineni S, Truffer M, 2002. Mechanisms of fast flow in Jakobshavn Isbrae , West Greenland : Part III. Measurements of ice deformation , temperature and cross-borehole conductivity in boreholes to the bedrock. Journal of Glaciology 48, 369–385.

MacGregor J A, Fahnestock M A, Catania G A, Aschwanden A, Clow G D, Colgan W T, Gogineni S P, Morlighem M, Nowicki S M J, Paden J D, Price S F, Seroussi H, 2016. A synthesis of the basal thermal state of the Greenland Ice Sheet. Journal of Geophysical Research: Earth Surface 121, 1328–1350.

Meierbachtol T W, Harper J T, Johnson J V, 2016a. Force balance along Isunnguata Sermia, West Greenland. Frontiers In Earth Science 4. doi:10.3389/feart.2016.00087

Meierbachtol T W, Harper J T, Humphrey N F, Wright P J, 2016b. Mechanical forcing of water pressure in a hydraulically isolated reach beneath Western Greenland's ablation zone. Annals of Glaciology 57, 62–70.

Meierbachtol T W, Harper J T, Humphrey N F, 2018. Short duration water pressure transients in western Greenland's subglacial drainage system. Journal of Glaciology 64, 171–174.

Person M, Bense V, Cohen D, Banerjee A, 2012. Models of ice-sheet hydrogeologic interactions: A review. Geofluids 12, 58–78.

Poinar K, Joughin I, Das S B, Behn M D, Lenaerts J T M, Broeke M R, 2015. Limits to future expansion of surface-melt-enhanced ice flow into the interior of western Greenland. Geophysical Research Letters 42, 1800–1807.

Thomsen H H, Olesen O B, 1990. Continued glaciological investigations with respect to hydro-power and ice-climate relationships at Pakitsoq, Jakobshavn, West Greenland. Rapport Grønlands Geologiske Undersøgelse 148, 83–86.

Thomsen H H, Olesen O B, 1991. Hydraulics and hydrology on the Inland Ice. Rapport Gronlands Geologiske Undersogelse 152, 36–38.

Thomsen H H, Olesen O B, Braithwaite R J, Bøggild C E, 1991. Ice drilling and mass balance at Pakitsoq, Jakobshavn, central West Greenland. Rapport Grønlands Geologiske Undersøgelse 152, 80–84.

van de Wal R S W, Smeets C J P P, Boot W, Stoffelen M, van Kampen R, Doyle S H, Wilhelms F, van den Broeke M R, Reijmer C H, Oerlemans J, Hubbard A, 2015. Self-regulation of ice flow varies across the ablation area in South-West Greenland. The Cryosphere 9, 603–611.

Walter F, Chaput J, Lüthi M P, 2014. Thick sediments beneath Greenland's ablation zone and their potential role in future ice sheet dynamics. Geology 42, 487–490.

Weertman J, 1957. On the sliding of glaciers. Journal of Glaciology 3, 33–38.

Wright P J, Harper J T, Humphrey N F, Meierbachtol T W, 2016. Measured basal water pressure variability of the western Greenland Ice Sheet: Implications for hydraulic potential. Journal of Geophysical Research: Earth Surface 121, 1134–1147.

Appendix A

Borehole measurements indicate hard bed conditions, Kangerlussuaq sector, Western Greenland Ice Sheet

(**Harper J T, Humphrey N F, Meierbachtol T W, Graly J A, Fischer U H, 2017.** Borehole measurements indicate hard bed conditions, Kangerlussuaq sector, Western Greenland Ice Sheet. Journal of Geophysical Research: Earth Surface 122, 1605–1618.)

A1 Abstract

The hydrological processes and sliding dynamics of the Greenland Ice Sheet are closely linked to the structural framework of its bed. Establishing whether the ice mass rests on bedrock relatively clear of rock debris, a thick deformable till layer, or some intermediate combination, is therefore key to understanding the ice sheet response to changes in meltwater inputs. Here we report on direct observations of the ice-bed interface along a flow-line transect in the ablation zone of the Western Greenland Ice Sheet. Our measurements are derived from a network of 32 boreholes that vary from ~100 m deep near the ice margin to 830 m deep, 46 km up flow from the terminus. We performed a suite of experiments and sampling techniques in the holes to investigate the bed conditions. In contrast to previous geophysical and drilling studies elsewhere in Greenland which have suggested the ice rests on a thick layer of sediment, we find no evidence for a thick sediment cover on the bed of the Kangerlussuaq sector of the ice sheet. Our observations imply this area has a relatively clean and hard bed and that this facilitates a basal hydraulic system governed by ice-bedrock interactions. The lack of sediment cover on the bed could be due to recent deglaciation and advance of this sector of the ice sheet, and/or variable rates of erosion and preferential routing of sediment through bedrock troughs.

A2 Introduction

The physical structure of the basal boundary of an ice sheet strongly controls the storage and flow of water at the ice-bed interface. The bed conditions are central to many ice sheet processes such as the mechanics of ice motion at the basal boundary, heat transfer between the solid earth and the ice mass, and the fluxes of sediment and chemical elements to the oceans. Further, the characteristics of the bed are the nexus of the processes driving subglacial hydrology.

A spectrum of bed conditions can exist with a corresponding continuum of hydrological conditions. At one end of the spectrum, the ice rests on a ‘soft’ bed characterised by a thick and continuous layer of sediment (e.g. Alley et al. 1986). Slow water flow occurs through the porous sediment which has relatively low hydraulic conductivity (e.g. 10^{-5} m s^{-1}), driven by pressure gradients as in Darcy flow. Alternatively, a system of canals incised into the top of the sediment layer (e.g. Walder and Fowler 1994) could be a primary pathway for water, in which case flow would be relatively fast.

The other end of the spectrum is termed a ‘hard bed’, and consists of ice resting on mostly sediment free bedrock (e.g. Weertman 1972). A subglacial drainage system develops at the ice-rock interface. The pathways for water flow on a hard bed arise from the separation between ice and bed due to ice sliding over bumps, and from melting of the ice roof due to heat generated by water flow (Iken 1981, Kamb 1987, Walder 1986). Water flow has potential to be fast, particularly when large channels form (e.g. Röthlisberger 1972).

Both seismic experiments and borehole drilling have been used to infer bed conditions at scattered locations around the Western Greenland Ice Sheet. Across the main axis of the Jakobshavn Isbræ trough, seismic reflection coefficients suggest the bed is comprised of a layer of lodged till (Clark and Echelmeyer 1996). However, drill holes to the bed at the edges of the trough implied basal water motion in a fast drainage system rather than by Darcy flow through porous sediment (Iken et al. 1993), or inferred hydraulic transmissivities between 10^{-5} and 10^{-4} m^2 s^{-1} that are indicative of coarse grained sand (Lüthi et al. 2002). Modeling of seismic P wave receiver functions collected at a site a few 10s of km north of Jakobshavn Isbræ suggests a remarkably thick basal sediment layer is present: 80 m at minimum, with the best model fit to data suggesting a sediment layer 160 m thick

(Walter et al. 2014). Borehole drilling appeared to confirm a soft bed in this area (Ryser et al. 2014). Further south in the Kangerlussuaq sector two seismic studies also suggested till exists at the ice-bed interface (Booth et al. 2012, Dow et al. 2013), although neither study employed methods capable of determining the sediment layer thickness.

While observations of bed conditions are sparse and can often be ambiguous, multiple locations along the flanks of west/central Greenland have been interpreted to have a sediment covered bed. The assumption of soft sediment at the bed has been adopted as the basis for modeling ice sheet motion by till deformation (Aschwanden et al. 2016, Bougamont et al. 2014). In contrast, the linkages between melt variations and surface velocity have been interpreted to hinge on conditions and processes typical of a hard bed (Bartholomew et al. 2012, Cowton et al. 2013, Doyle et al. 2015, Sundal et al. 2011). Constraining the subglacial framework is thus first and foremost to interpreting the basal hydrological and basal motion processes. Here we investigate the bed conditions along a flow line through the ablation zone of Western Greenland. We present multiple lines of mechanical and hydrological experimental evidence collected in a transect of boreholes drilled to the base of the ice sheet, and then use the in situ observations to interpret the physical framework of the ice-bed interface.

A3 Methods

Our investigation is focused on a ~50 km long transect in the ablation zone of the Kangerlussuaq sector of Western Greenland, where we drilled 32 boreholes to the bed of the ice sheet between 2010–2015 (Figure A-1). We used hot water drilling methods, with computer monitored load to adjust drilling speed to ensure boreholes were drilled vertically using a free-hanging drill stem (Humphrey and Echelmeyer 1990). The holes are located at six different sites, with 2 to 10 boreholes drilled at each site. The depth of the holes ranges from just under 100 m at locations less than 1 km from the ice sheet margin, to 830 m at a location about 46 km inland from the terminus of Isunnguata Sermia (Table A-S1).

The basal topography of this region of the ice sheet is dissected by several deep troughs. Our boreholes sample topographic domains that include a relatively flat region, a ridge between troughs, and one trough of relatively minor depth and length (Figure A-2). The region also contains a bifurcating trough of exceptional depth, which we have not fully penetrated with a drill hole. Measurements of ice temperature (Harrington et al. 2015) as well as borehole observations of hydrological conditions (Wright et al. 2016), reveal that all locations have basal ice at the pressure melting point and have an active water system at the bed.

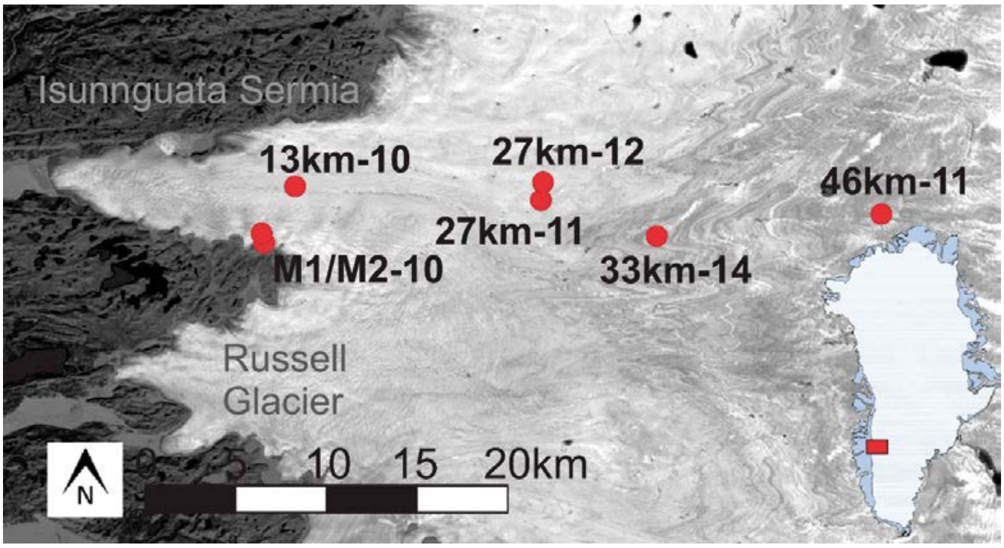

Figure A-1. Map showing sites where boreholes were drilled in Western Greenland. Site names represent distance from terminus of Isunnguata Sermia outlet glacier, with dashed extension signifying the year holes were drilled. The basal topography of the region is shown in Figure A-2.

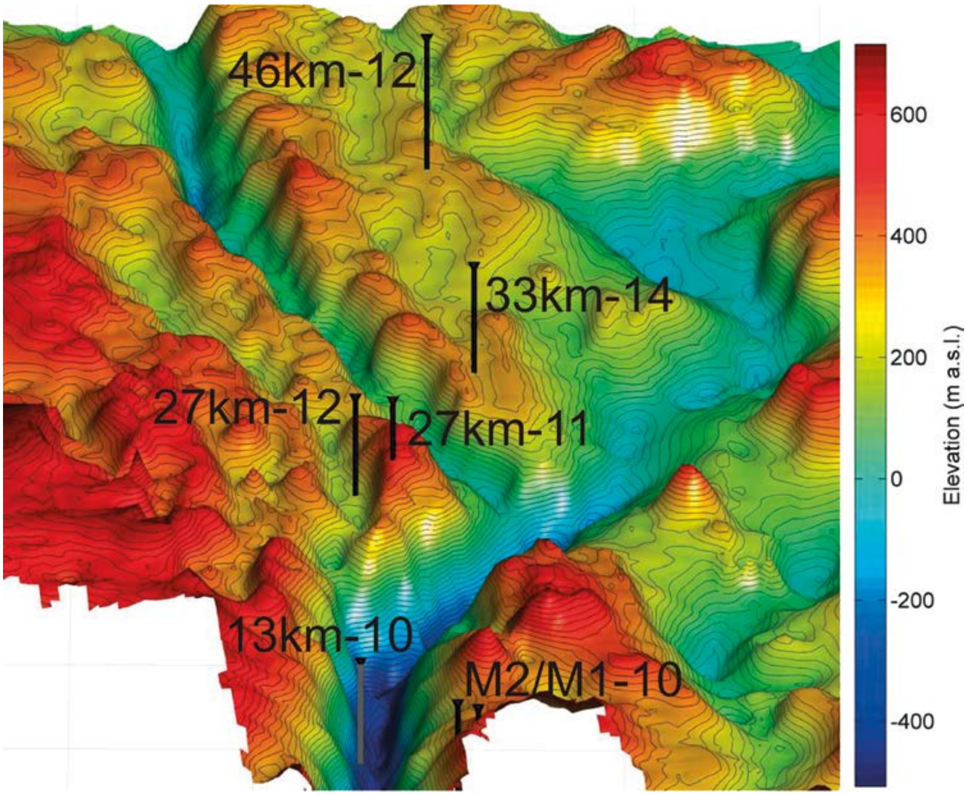

Figure A-2. *Bed elevations of study reach from DEM of Lindbäck et al. (2014). Vertical black lines indicate drilling sites; labels indicated distance in km from terminus of Isunnguata Sermia (see Figure A-1) and year the holes were drilled. Color bar shows elevation above sea level. The depth of trough at 13 km is poorly constrained; two holes were drilled there to 750 m depth, but they did not intersect the bed. Sites M2 and M1 are 1.5 and ~1 km from the ice edge, respectively. Note that the view contains vertical and perspective distortions.*

Although boreholes allow a direct observation of the bed, they only sample a small region of the bed, which may have been disturbed by the drilling process. Therefore, no single measurement or experiment yields an indication of the conditions at the bed that is completely unambiguous and capable of rendering all other evidence unnecessary. To address this problem, we employed a suite of different types of observations in the boreholes (Figure A-S1) which are then compared and evaluated for consistency. Due to the limited time the holes remain open after drilling – they refreeze in just 2–3 hours in some cases – not every type of measurement could be conducted in every borehole (Table A-S1).

A3.1 Drilling action

The behavior of the drilling system yields diverse information about the ice-bed contact when the stem of a hot water drill first encounters the bed. The jet of 1 000 psi water issuing from a ~80 kg drill stem provides details regarding the abruptness, erodibility, and hydrological characteristics of the glacier substrate. To record this information, two factors are closely monitored.

Load on drill tower. The weight of the drill stem and hose hanging from the drill tower was measured with a digital load cell embedded in the tower's drive wheel. The load increased steadily throughout drilling as additional hose was lowered into the borehole. The load was nearly completely relieved from the tower when the drill stem encountered the bottom of the hole. The load cell signified this change, which could be confirmed by the appearance of slack in the hose. A soft and erodible bed causes a gradual load reduction whereas a very abrupt loss of load results from a hard bed. Further, when the drill was backed-up and re-advanced, the load loss appears at the same position with a hard bed, but a soft bed will permit continued progression as the drill penetrates deeper into the sediment.

Back-pressures in the pumping system. Once the drill tip has reached the bed, sudden pulses of water pressure occur due to inhibited outflow of drilling water if the ice-bed contact is abrupt and non-erodible. The pressure pulses occur as the high pressure jet bounces against the bed and the drill orifice is solidly blocked. Alternatively, if the bed is soft and erodible, back pressuring is noticeably absent. We observed these events with non-recording pressure gauges on the pumps. Permanent records were obtained using water pressure transducers in the actual borehole, which captured the pressure pulses from expansion/contraction of the drill hose.

A3.2 Penetrometer experiments

Damage, or lack thereof, to the drill stem as it encountered the bed provided information about the hardness and penetrability of the bed. Several aspects of stem damage were examined, including impact damage to the exit nozzle and scratches on the 2 m long stainless steel housing on the drill stem. In addition, attempts were made in several boreholes to drive a penetrometer tool into the bed with a percussion hammer (e.g. Blake et al. 1992, 1994).

A3.3 Decay of thermal perturbations

Independent information about bed conditions was provided by measurements of the temperature drop between drilling water and borehole water during the drilling process. The temperature of the drilling water exiting the stem, and the temperature of water within the borehole 1.5 m above the exit nozzle, were both recorded by a datalogger. These data are used to quantify the heat exchange of the hot water jet. While drilling through clean glacier ice, heat transfer to the ice is relatively constant and temperature records of the water returning up the borehole are smooth and predictable. Warmer return flow indicates less drill water in contact with ice, in turn implying the water jet has impinged on low effective heat capacity material, such as rock or till. Cool return water could be caused by mixing with cold basal water in a cavity or loss of water to the basal drainage system.

A3.4 Sampling and photography

Samples of bed material and basal water were collected in nine boreholes, ranging in depth from 100 m to 830 m. The cable-operated sediment sampler consists of a stainless steel tube, with an internal brass weight and flap valves on the top and bottom to permit entry of sediment and expulsion of water (Graly et al. 2014). A cable to the surface was used to pull water and sediment into the sampler and then expel the water fraction, and this process was repeated 10–20 times to accumulate a sediment sample. The maximum opening on the sampler inlet excluded particles larger than 1.25 cm.

Thirteen boreholes were photographed with a borehole video camera that was lowered and raised to capture video images of the ice walls and bed. Two holes were photographed with a still camera with a signal wire that was frozen into the hole, thus permitting time-lapse images of the bed. Each of these boreholes was located within several km of the ice margin.

A3.5 Hydrological conditions

Several aspects of subglacial hydrology are used to infer the characteristics of the subglacial pathways for water routing. Data collected include both active impulse experiments and passive observational time series.

Hole drainage. During the drilling process boreholes filled with water to the surface as drill water was continuously added to the hole, giving the base of the borehole a relatively high head (110 %) with respect to the ice overburden pressure. When the advancing borehole intersected the bed, one of three scenarios occurred: 1) a sudden draining of the borehole and equalization of the borehole pressure to that of the subglacial drainage system; 2) delayed draining, fast or slow, and eventual equilibration of the hole with bed pressure; or, 3) no draining with the hole maintaining static and high head indefinitely. Water pressure transducers in the boreholes measured the duration of drainage events, and using the diameter of the holes the volume of water drained was calculated. The characteristics of borehole drainage are a reflection of hydraulic transmissivity of the basal layer, such as slow porous flow through a sediment matrix or high flux through open channels. Holes sometimes fail to drain at all because no connection was established with a water-transmissive region of the bed.

Impulse tests. We artificially perturbed the borehole head after the initial drainage of the hole and establishment of equilibrium with the surrounding subglacial system. The head was increased above equilibrium by adding water into the borehole. This was accomplished as either a sudden spike of water dumped down the hole in 10s of seconds, or as a steady flow of water pumped into the hole over a period of hours. Water levels were monitored in the borehole, and in many cases also in adjacent boreholes located 10s of meters away. The response to the head perturbation reveals information about the transmissivity and stability of the subglacial drainage layer (e.g. Kulessa et al. 2005).

Water pressure gradients. Water pressure was measured in boreholes using down-hole pressure transducers and was recorded for periods of up to several years (Wright et al. 2016). Time series of pressure variations and gradients between boreholes yield information about the nature of basal water flow, and therefore the nature of the substrate hosting the subglacial drainage system.

Dye tracing. Drilling water was spiked with a known concentration of rhodamine dye as the hole was being drilled. Immediately after the hole was completed, a water pressure transducer and rhodamine sensitive flourometer were installed at the bed for long term recording of basal water pressure and changes in dye concentration relative to the original value (Meierbachtol et al. 2016). The initial dilution of the rhodamine by subglacial waters provides constraint on the volume of water in the subglacial drainage system. Subsequent time series of dye concentration reveal flow of basal water.

A4 Results

A4.1 Bed penetrability and erodibility

Drilling action. As the drill contacted the bed, we encountered very large pressure spikes with back pressuring in the pumps of up to +/− 1 000 psi. Pressure pulsing of drill hose was evident in borehole pressure transducer recordings (Figure A-3). As boreholes intersected the bed, the load on the drill tower was relieved abruptly rather than gradually. Raising the drill stem terminated the pressure pulses and reestablished the load, thus providing confirmation that the bed had been encountered. Advancing the drill again confirmed the position of the bed. This process was repeated several times with the bed consistently identified at a fixed depth. In several holes, some indication on the load cells or vibration in the drill hose was noticed up to 1–2 m above the obvious bed. This behavior was likely due to minor debris entrained in the basal ice, as we have observed with borehole photography.

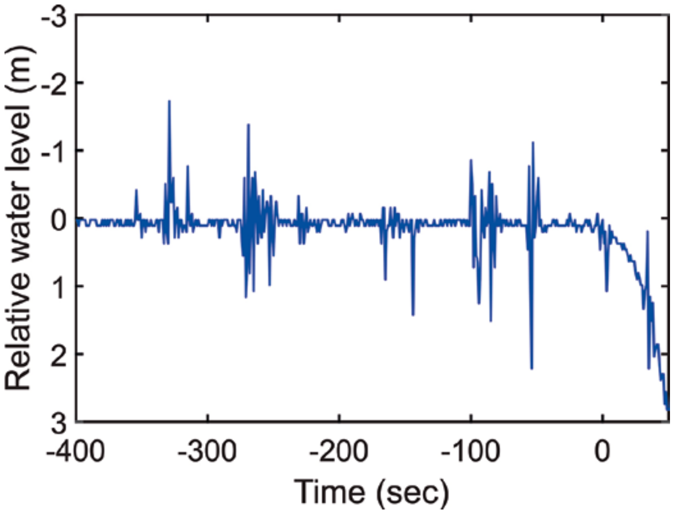

Figure A-3. *Water pressure pulses in a borehole recorded when drill stem encountered the bed at 700 m depth at site 27km-12. Pulses were measured by a borehole pressure transducer located near the surface of the hole. The water level axis is relative to the initial water level in the borehole, and the time axis is relative to drainage initiation in the hole. Oscillations of up to 2 m head result from pressure pulses on the long length of hose in the borehole as the high pressure water jet on the drill stem bounces against a non-penetrable surface on the bed, temporarily blocking the orifice. The borehole began draining at time = 0.*

Penetration tests. The nozzles at the end of the drill stem all exhibited substantial damage due to blunt-force impact with a hard surface at the bed (Figure A-4a). The drill stem clearly encountered a hard surface rather than a soft (e.g. clay or sand rich) layer. The damage occurred with near-perpendicular impact, rather than as penetrating and oblique collisions with multiple clasts. The nozzles often became pitted, which we assume was due to abrasion from sand sized sediment stirred by the high pressure jet of water. Importantly, the abrasion was limited to the nozzles and the lowest few centimeters of the drill stem. Higher up the drill stem, abrasion or scratches were notably absent (Figure A-4b) implying the stem never penetrated more than a few cm into a sediment layer. Previous drilling into known till beds has shown significant scratching and gouging at least 2 m up the stem (e.g. Humphrey et al. 1993). Penetrometer tests in several boreholes also failed to show signs of a penetrable bed (Figure A-4c), even with repeated hammer drops.

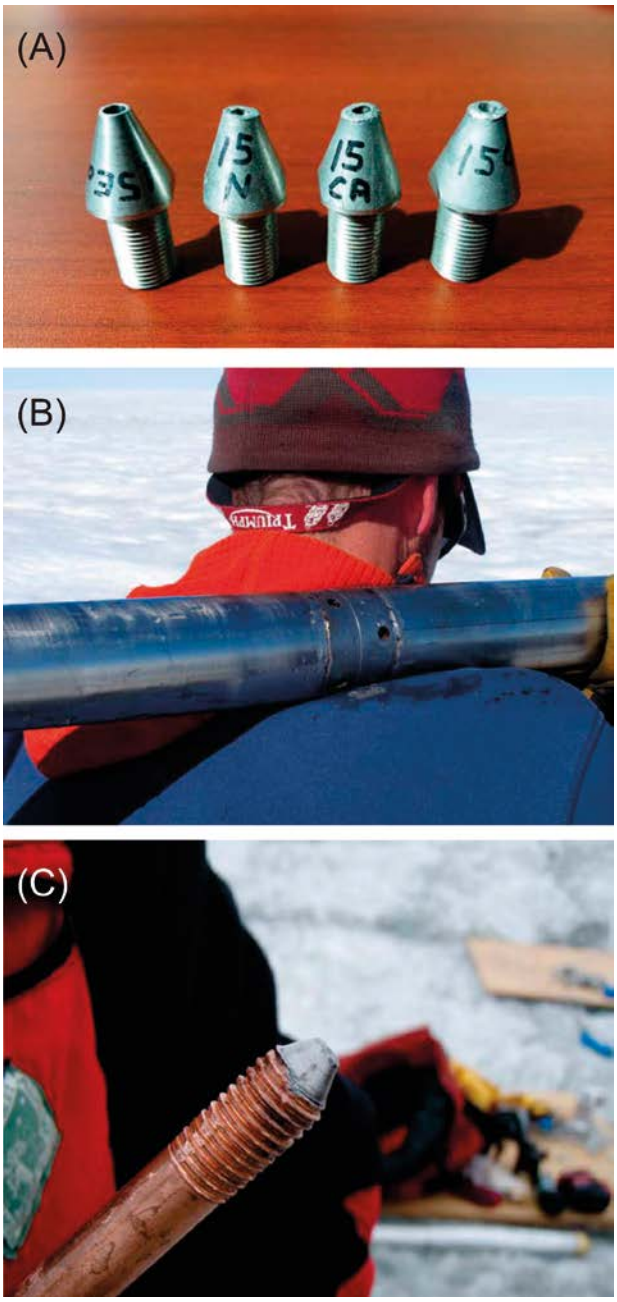

Figure A-4. *Penetration of drill stem and penetrometer into the bed. A) drill nozzles showing damage resulting from near perpendicular impact with the bed. For comparison, the left most nozzle was used to drill >1 km in several different boreholes, but was never in place when intersecting the bed. B) stainless steel drill stem notably lacking scratches or signs of abrasion after intersecting the bed in 31 boreholes. C) Penetrometer after it was forced into the bed with a sliding hammer on a cable with six hard blows. Note impact damage to the tip, but the lack of scratches to the soft brass threads just above tip.*

Thermal decay. Time series of borehole water temperatures provide an additional test of the abruptness of the basal boundary. The example shown in (Figure A-5) demonstrates the information revealed by the thermal measurements. The borehole water temperature adjacent to the top of the drill stem was relatively steady as the borehole advanced through the ice mass. But at the bed, the temperature in the borehole became elevated as warm drilling water was reflected from the bed and up the borehole. This indicates heat in drill water was not used to melt ice, and was not evacuated away from the hole through a drainage pathway. The temperature adjacent to the drill stem quickly cooled as the drill was pulled back up hole into colder water, and warmed after again advancing to the bed. The re-advance lead to an even greater temperature rise since the drill had likely created a rock floored hole that reflected the hot water jet up the hole. Soon the hole connected to a transmissive drainage system and water rapidly exited the borehole. The water adjacent to the drill stem become cold as the water from higher in the borehole drained toward the bed.

A4.2 Bed covering

Relief. Considerable variability of the ice thickness was observed in boreholes located only 10s of meters apart with little surface slope between them. For example, the depths of four boreholes, drilled at a site located 27 km from the terminus with nominal 700 m depth, varied by up to 20 m between holes (Table A-1). These holes were separated horizontally by ~25–60 m, meaning the slope of the basal interface between them was up to ~35 degrees. The ice-bed contact was thus characterised by high roughness and relief, rather than a smooth boundary between ice and the bed.

Table A-1. Short length scale relief on bed indicated by borehole drilling depths.

Hole	Depth (m)	Separations	Distance (m)	Difference (m)	Slope (deg)
GL12-2A	700	2A to 2B	29	15	27
GL12-2B	715	2A to 2C	57	5	5
GL12-2C	695	2A to 2D	48	1	1
GL12-2D	701	2B to 2C	28	20	36
		2B to 2D	24	14	30
		2C to 2D	25	6	13

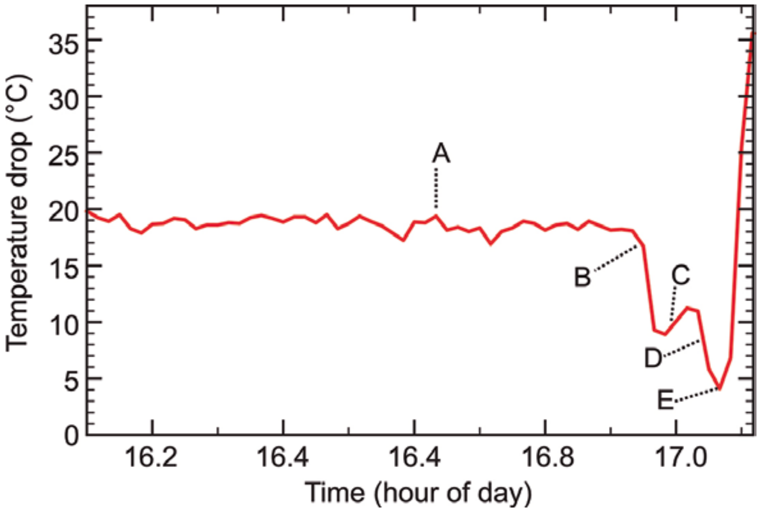

Figure A-5. *Time series of borehole water temperature showing temperature difference between the drill tip and water in borehole 1.5 m above. The data were recorded in a borehole at site 33km-14, as the drill encountered the bed at 671 m depth and provide evidence of a hard impenetrable bed. A) relatively constant water temperature as the drill advanced through ice and the heat of drilling water was used to melt ice; B) increased water temperature when the bed was encountered and hot drilling water circulated up the borehole; C) decreased water temperature when the stem was pulled several meters up the borehole; D) increased water temperature when the drill encountered the bed a second time; E) decreased water temperature when the borehole drained, bringing colder water down the borehole.*

Photography. Borehole video and time-lapsed images with a fixed camera revealed that in some cases sediment was entrained in the lowest 1–2 m of ice above the bed (Figure A-6a). A mantling of relatively coarse sediment (i.e. lacking fine grained particles such as clays) was observed resting on the bed. Further, the relatively clear water points to an absence of the fine fraction of sediment at the bed. Some of the observed sediment on the bed was likely deposited as the borehole drilled through overlying ice and freed entrained debris. Time lapse images of the bed did not reveal overturning or other signs of deformation of the sediment on the bed, but instead showed steady motion of the bed past the borehole (Figure A-S2).

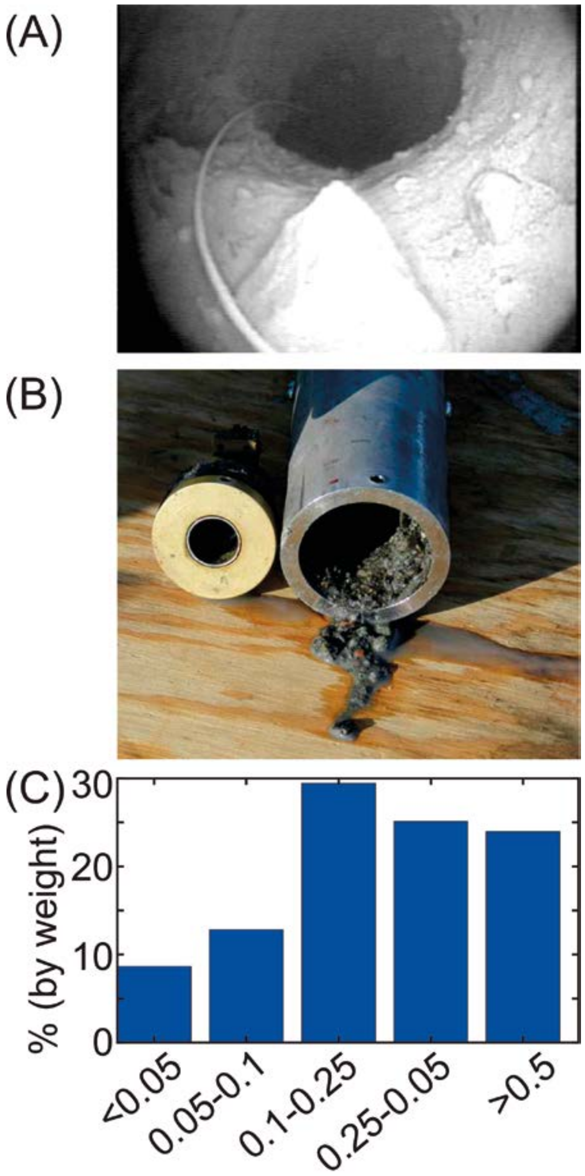

Figure A-6. *Sampling and photography of basal sediment. A) Image from borehole video camera showing sediment entrained into ice ~0.75m above the bed. Wire extending down borehole is 5.1 mm diameter. B) image of bed sampler with sand and fine gravel retrieved from the bed at 701 m depth. C) Size distribution of sediment samples retrieved from ice/bed contact. Combined results are shown for samples retrieved from 7 different boreholes ranging from 100 m to 830 m depth. Two additional boreholes were sampled but produced only trace amounts of sediment. The sampler does not collect particles larger than 1.25 cm diameter.*

Sampling. Direct samples from the bed retrieved primarily sand and fine gravel and were generally lacking in fine material (Figure A-6b), which would normally stick to a sampler. The geochemistry of these samples are discussed in detail by Graly et al. (2014, 2016). The most dominant grain size was 0.1 to 0.25 mm, and fine grains such as clay and perhaps some silt have been flushed from the distribution (Figure A-6c). The chemical mass balance of the samples compared to bedrock and water chemistry is also consistent with the physical removal of clays (Graly et al. 2016). The volume of material recovered was highly variable, ranging from ~50–850 grams, and two of the boreholes produced only trace amounts of sediment. We know of no reason why the sampler would not collect a sample if sediment was indeed present. While we cannot rule out this possibility, we believe the most likely scenario was that no retrievable sediment was present.

A4.3 Hydrologic properties

Hole drainage. Instant and rapid drainage was a common occurrence when the drill stem neared the bed during the drilling procedure. In about half of the cases, the drainage occurred when the drill stem was in temperate basal ice above the bed; typically a few meters above the bed, but in several cases the draining events occurred when the advancing hole was 25–35 m above the bed. The hole either connected to the bed by hydro-fracturing due to the artificially high pressure in the water-filled drill hole, or the hole intersected a pre-existing opening such as a basal crevasse. Other observations as described above imply the drill advanced through ice and not sediment after the drainage event.

The subglacial drainage system easily accommodated the water added from the borehole during drainage events. The volume of water drained from the hole generally scaled with the depth of the ice and thus the overburden water pressure (Figure A-7). In other words, the deeper the ice, the more water drained from the hole in order for the water level in the hole to lower to the depth equivalent to ice overburden pressure. However, the water volume varied by up to ~40 % for a given hole depth, which likely reflects local pressure gradients at the bed and variable transmissivities of pathways in the drainage system. Rapid drainage of holes demonstrates high transmissivity at the basal interface. For example, borehole water levels dropped by as much as 125 m in 72 seconds. Measurements in multiple holes separated by 10s of meters showed pressure variations in response to the drainage of the drill hole in some nearby holes, whereas other holes had no response whatsoever. Thus, detectable flow was not radial away from the base of the draining hole.

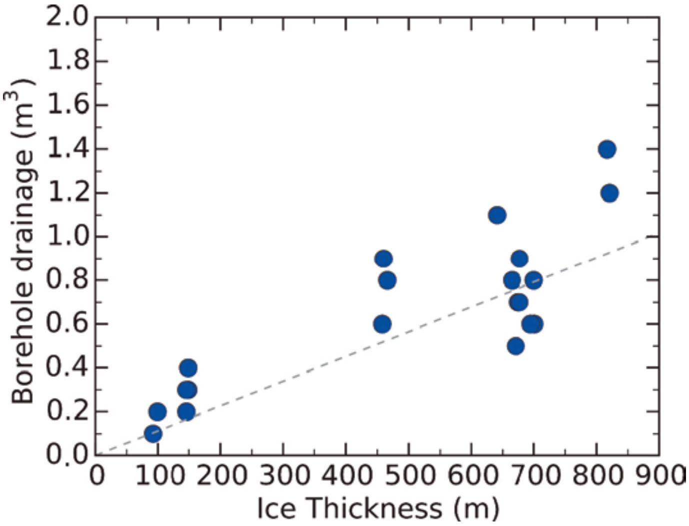

Figure A-7. *Relationship between depth of ice drilled through and the volume of water drained from borehole to basal drainage system upon intersection of the borehole with the bed. Dashed line shows drainage required for equalization of the borehole to ice overburden pressure.*

At sites <1.5 km from the ice sheet margin, where the drainage system near the margin is dominated by a few very large channels that discharge water at the ice edge, five of 13 boreholes drilled failed to drain at all. Because the ice near the margin is entirely temperate, these holes remained open for more than one month and were filled with water to the surface the entire time. In addition, several boreholes drilled at site 33 km drained rapidly, but only after a delay over various time intervals from other indicators of having reached the bed.

Impulse response. Impulse tests also indicated the bed was transmissive but with discrete pathways and variable responses. A sudden slug added to a borehole would commonly result in a sloshing action with water exchange into an adjacent borehole located 10 or 20 m away. The result was oscillating water levels in one or more boreholes (Figure A-8b; Figure A-S3). Similar to the borehole drainage events, however, the transmissive pathways to adjacent boreholes were variable: one nearby hole would oscillate in response to a slug while another would not.

Pressure gradients. Time series of basal water pressure reveal substantial water pressure gradients between adjacent boreholes spaced 10s to 100s of meters apart. While a constant pressure gradient of ~20 kPa m^{-1} between holes just 20 m apart was observed for more than a month at site 46km-11 (Wright et al. 2016), more typically the magnitude of gradients tended to be transient over periods of many weeks (Figure A-9).

Dye dilution and transport. Direct tracing of basal water flow yielded results consistent with water flow through discrete and high transmissivity passageways. An example time series of basal dye concentration is shown in Figure A-10. This borehole initially intersected a stagnant but relatively large water body at the bed, the volume of which was determined by dilution of the dyed drilling water to be on the order of 1–7 m^3 (Meierbachtol et al. 2016). Dye concentrations indicated little-to-no water flux into or out of the cavity for a period of weeks. Then, in a matter of minutes, the cavity connected to active drainage and all water containing dye was evacuated.

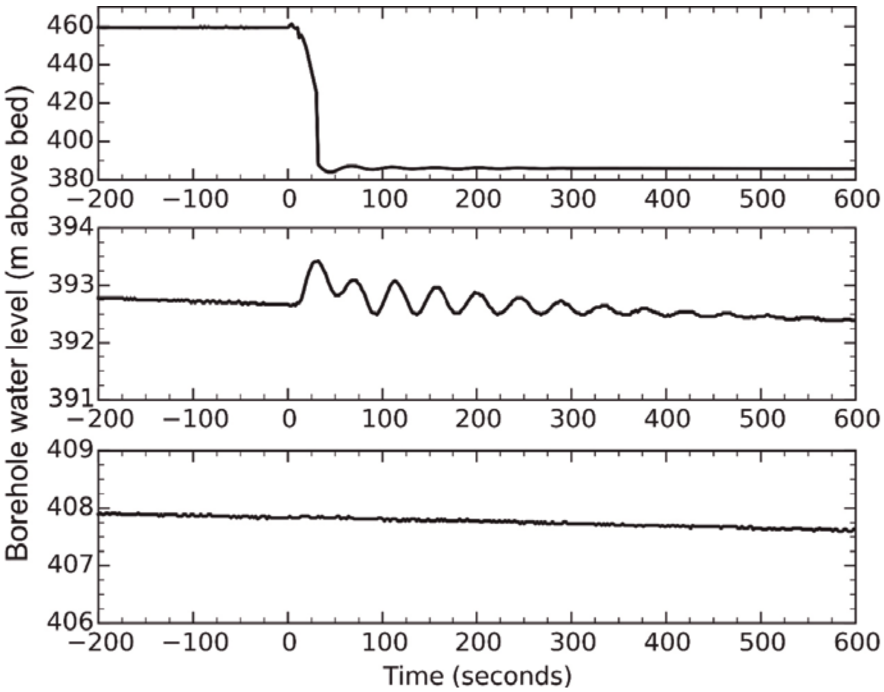

Figure A-8. *Heterogeneous water level variations in three different boreholes during drainage of a drill hole as the drill stem encountered the bed. Vertical axis shows meters of water in borehole above the bed; time axis is plotted with zero at the initiation of borehole drainage A) water level drop of ~75 m in the drill hole as water drains from borehole into subglacial drainage system; B) water level oscillations in borehole located 20 m south in response to drainage of drill hole. Underdamped oscillations represent highly transmissive connection between the two boreholes; C) no water level response in a borehole located 20 m west of drill hole, suggesting no transmissive connection between the two holes.*

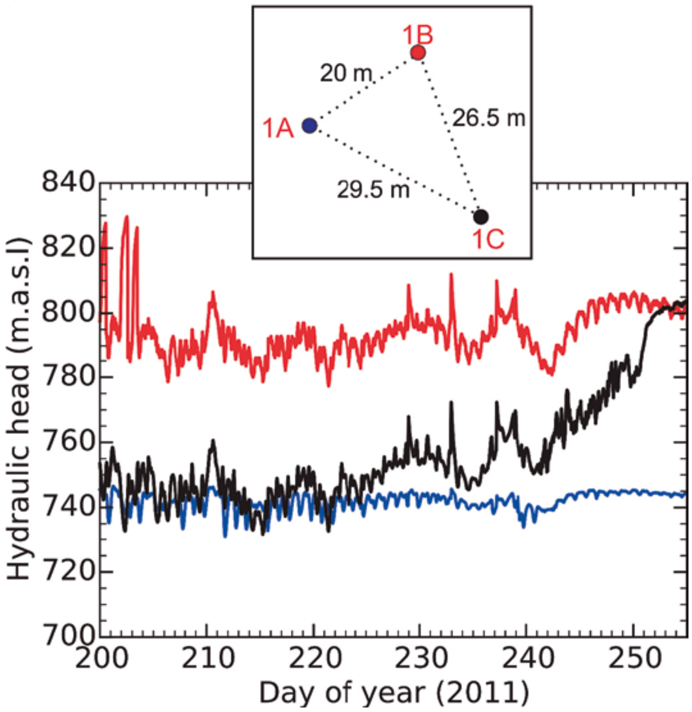

Figure A-9. *Time series of three borehole water pressure records showing spatial gradients of subglacial water pressure. The three boreholes are located at site 27km-11, and are located 20–30 m apart as shown in inset at top; data colors refer to hole names in inset. Large head differences of up to ~60 m are established between the boreholes, but vary over time.*

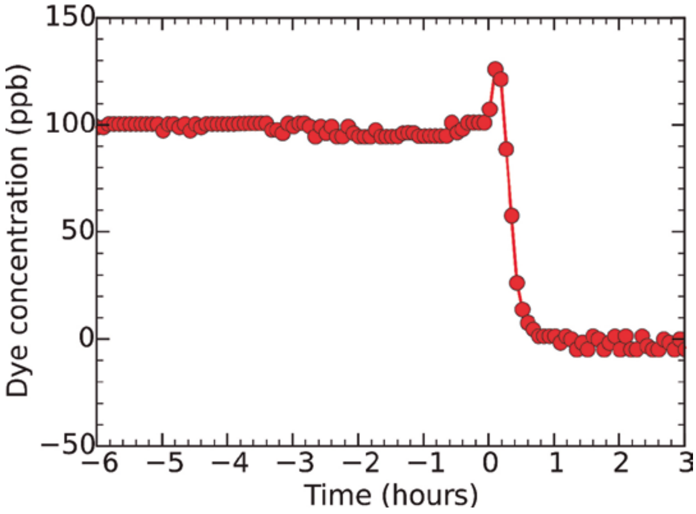

Figure A-10. *Time series showing the concentration of dye injected into basal water. Drilling water was spiked with a known concentration of Rhodamine dye; dilution of the drilling water by basal water suggested the borehole intersected a cavity of basal water of ~1–7 m*^{3} *volume. Dye concentration was steady for a period of 12 days (not shown in graph) before the step decrease in dye concentration which occurred over ~0.5 hours. Time axis is relative to the initiation of this decrease.*

A5 Discussion

A5.1 Conceptualisation of basal interface

Our array of borehole tests and experiments collectivity yield five important observations of the bed in our study locations:

1. The ice sheet bed is an abrupt boundary which is impenetrable at the scale of decimeters by a 1 000 psi water jet or a sliding hammer penetrometer (revealed by drilling action, thermal decay of drilling water, and penetrometer tests).
2. Roughness elements of the ice-bed interface larger than several meters amplitude over 10–20 m horizontal distance are not submerged by a sediment layer (revealed by depth variability of boreholes).
3. Fine grained sediment such as clays and fine silts at the ice-bed contact are lacking (revealed by borehole photography and sampling of bed material).
4. Water pressure gradients of 10s of kPa m^{-1} are persistent at the ice-bed contact (revealed by borehole water pressure time series).
5. Water flow at the bed has highly transmissive pathways and non-transmissive regions (revealed by drilling tests and impulse tests).

Based on this body of evidence we conclude that there is no thick (i.e. >1–2 m) layer of sediment at the floor of our drill holes. We find no evidence for such a layer, and the contrary postulate that there is a thick layer of sediment fails tests against our observations. For example, the boundary between the ice and a sediment layer 10s of meters thick would need to sustain local slopes of ~35 degrees over length scales of 10s of meters; such slopes of the ice/sediment interface would somehow need to resist very high shear stress on the bed. Further, the sediment interface would need to be impenetrable to our drill stem (causing nozzle damage) and hammer-penetrometer, and would need to be erosion resistant to a 1 000 psi jet of water. That a thick layer of sediment could meet these stipulations is unlikely.

Our observations also lead us to conclude that the primary mechanism for water flow is through a system of discrete pathways rather than the pores of a sediment framework. We observe a system that maintains large spatial gradients in pressure, heterogeneous directionality of flow, and is capable of remarkably high transmissivity; each of which are inconsistent with porous media flow.

We consider several of our hydrological observations against alternative interpretations for water flow through sediment. First, pore water pressures in a till may show large spatial gradients as we observe, because the permeability of till can be wide ranging (Iverson 2010). However, we observed large pressure gradients in a basal water system undergoing strong time variability, suggesting transmissive pathways rather than flow through till pores with low conductivity. Second, rapid drainage of boreholes that have intersected till beds has been reported in the literature, and has been attributed to radial flow caused by sudden uplift of ice at the sediment interface (Engelhardt et al. 1990). In our case, however, this mechanism is unlikely due to the spatially variable responses we observed in nearby boreholes, both during drainage events and subsequent impulse tests. Finally, a simple back-of-the-envelope calculation demonstrates that Darcy flow through a till layer would be untenably slow to evacuate the copious water input from moulins located many 10s of km inland from the ice margin: driven by the high pressure gradients we observed in our boreholes (e.g. 20 kPa m^{-1}), and with a typical till permeability (1.6×10^{-15} m^2) (e.g. Clarke 1987) water transport would be less than 60 m yr^{-1}.

Our observations of high transmissivity, taken alone, could be attributed to flow within a system of canals incised into the top of a sediment layer (Ng 2000, Walder and Fowler 1994). A canal system, however, contradicts our drill penetration and sampling observations that imply our holes have not encountered a thick sediment layer. Further, other hydrological evidence is unsupportive of canals: for example, borehole dye tracing experiments show an isolated cavity of m^3 volume persisting for weeks, and then suddenly connecting to a transmissive flow system. This observation is commensurate with the theoretical dynamics of cavities on a hard bed, but we have no explanation for such behavior in a canal system.

A summary of our conceptualisation of the ice-bed interface is as follows (Figure A-11). The bed is effectively 'hard' with respect to hydrologic and sliding processes as it is characterised by meter scale bedrock roughness with a relatively thin mantling of coarse sediment. Sediment on the bed is decimeters to perhaps meters thick in places, but is not many meters to 10s of meters thick. Fine grained silt and clay have mainly been flushed from the bed. Some sediment is entrained into the ice, but limited to the lowest few meters. The hydrological properties of the bed consist of discrete pathways of highly transmissive water flow, separated by regions of the bed which are effectively non-transmissive. We envision a system of dynamic cavities and linkages. Coarse sediment likely occupies portions of cavities and perhaps chokes linkages with gravel and boulders, but the lack of fine grains permits high transmissivity of basal water.

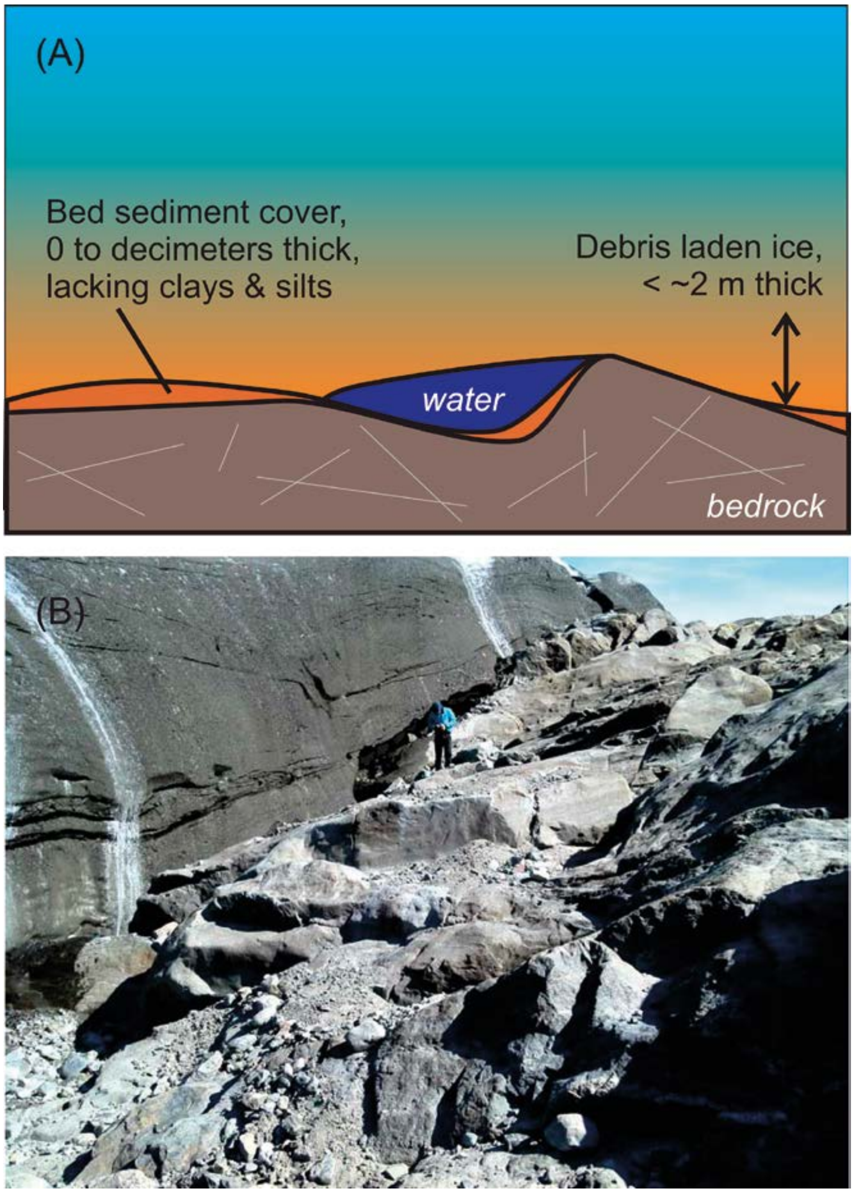

Figure A-11. *Conceptualization of bed conditions developed from the suite of experiments and observations. A) Cartoon depicting a relatively thin and spatially variable mantling of course sediment on bedrock. Elements of subglacial drainage system are dictated by bed roughness. B) Photograph of recently deglaciated area near site M1 (Figure A-1) demonstrating conceptualization of subglacial conditions. Bed roughness exists at a range of scales, with course sediment accumulated in scattered patches. Subglacial locations likely have slightly thicker and greater areal distribution of sediment than depicted in photograph.*

A5.2 Comparison with other observations

Our observations of drilling action suggested an abrupt and hard interface was encountered at the base of all boreholes. These observations are distinctly different than that reported by Ryser et al. (2014) in boreholes located several 10s of km north of Jakobshavn Isbræ. Their hot water drill holes encountered a bed without an abrupt or constant boundary; rather, the bed produced a gradual release of load on the drill tower. Raising and advancing the drill stem again caused the depth of their holes to increase. And, pressure pulses in the drilling system were not observed when the high pressure jet intersected the bed. Our observations of borehole drainage are also different: their drill holes rarely drained and never during the drilling process, which they interpreted to be a strong indication that their boreholes intersected a sediment covered bed.

Importantly, further south on the very northern edge of the Jakobshavn Isbræ trough, Lüthi et al. (2002) report many observations with similarities to ours. At Lüthi's site D, the boreholes drained rapidly and water pressure pulses were observed between nearby holes. This behavior was distinctly different to that at their other sites, and interpreted to be quite suggestive of a bedrock basal boundary rather than thick sediment (Lüthi personal communication).

Closer to our borehole transect, two different seismic studies conducted 10s of km away concluded that the bed is covered by a till layer. Although neither study determined the thickness of the layer, both studies inferred a thicker till layer exists than we have identified with our boreholes. Booth et al. (2012) used seismic amplitude versus angle methods to characterise bed reflections at a site south of our transect and ~70 km inland. The acoustic impedance was indicative of a lodged till deposit with low porosity, but Poisson's ratio suggested a highly water-saturated substrate. Their explanation for this apparent discrepancy was that a thin (<2m) layer of dilatant till rests on top of a thicker lodged till; the thin layer is unresolvable but interferes with seismic wavelets. Similarly, a study conducted 13 km from the Russel Glacier terminus suggested a layer of porous sediment was present at the ice bed interface, although its thickness was undetermined (Dow et al. 2013).

Our conceptualisation is consistent with the thin layer of porous sediment proposed by Booth et al. (2012), but is not consistent with the existence of a thick underlying layer of lodged till. For example, we expect that our 1 000 psi water jet would have easily penetrated into the top of a lodged till, as was apparently the case with the drilling conducted by Ryser et al. (2014). Similarly, our results are consistent with the porous till reported by Dow et al. (2013), but only if the layer is much thinner than inferred in that paper.

Other studies have inferred bed conditions of this region based on modeling or observations of ice sheet motion. Our results are inconsistent with the 5 m thick layer of deforming till assumed in the modeling study by Bougamont et al. (2014). That work modeled till deformation across this region of the ice sheet driven by seasonal changes in pore water pressure. In addition to our failure to find evidence of a deforming till layer, we in fact observe high and sustained basal water pressure during the winter months (Wright et al. 2016), a period with relatively slower ice velocity (Palmer et al. 2011).

Our observations of the bed are consistent with the hard bed conditions interpreted from analysis of the seasonal changes in surface velocity (e.g. Bartholomew et al. 2012, Sundal et al. 2011) and assumed in models for subglacial drainage development along the margins of Greenland (Hewitt 2013, Schoof 2010, Werder et al. 2013). Our findings are also consistent with the melt water input driven uplift on bedrock cavities, interpreted from GPS vertical signals (Doyle et al. 2015). However, our other pressure data and analyses do not necessarily support previous interpretations that large channel growth results in reduced pressures during the melt season (Meierbachtol et al. 2013, Wright et al. 2016).

An obvious question is why the ice in our study region apparently rests on bedrock, whereas observations north of Jakobshavn Isbræ imply the ice sits on a sediment package many 10s of meters to >100 m thick (Ryser et al. 2014, Walter et al. 2014). We note several factors that are perhaps relevant. First, relative to elsewhere in Greenland, our study region experiences low winter accumulation paired with high summer melt (Ohmura and Reeh 1991). The surface mass balance produces a large meltwater flux, and this can be expected to result in high basal water fluxes. Second, our study region of the ice sheet experienced mid Holocene deglaciation, followed by a re-advance of the margin. The margin retreated for a period of about 6 000 years to an unknown point, but likely many

10s of km inland from present and encompassing our entire study domain, and then readvanced starting 4 000 years ago (Simpson et al. 2009, van Tatenhove et al. 1996). Perhaps this episode of retreat and advance stripped the bed relatively clean of sediment. Finally, whereas the Walter et al. (2014) study was conducted in a basal trough likely filled with sediments, we have mainly drilled on regions outside of deep troughs. This latter point is discussed in more detail in the next section.

The bed conditions need not be restricted to a single structural makeup across an entire glacier or ice sheet. The underlying geologic framework, historical ice variations, current and past ice flow dynamics and climate conditions are among the many factors that likely contribute to the derivation of particular bed conditions. Over the vast expanse of the Greenland Ice Sheet, for example, each of the above factors can differ substantially and so there is little to justify an assumption that the bed should have the same makeup in all locations. Similarly, there is little reason to suspect the physical structure of the bed is a steady state condition beyond perhaps a time scale of decades-to-centuries.

A5.3 Basal sediment flux

Our borehole observations of a thin-to-absent basal sediment cover along the study transect of the Kangerlussuaq sector creates a bit of a conundrum. We observe relatively little sediment at the base of our boreholes, and we find no evidence for an accumulating layer of basal sediment along our flow line transect. Yet, the proglacial valleys contain large sandurs (Figure A-S4) and have undergone relatively recent and large-scale in-filling (Storms et al. 2012). Further, one study argued that the Leverett Glacier stream outlet just to the south of our transect has high sediment flux due to rapid erosion of the ice sheet bed (Cowton et al. 2013).

We speculate the solution may revolve around the very deep trough that dissects the region (Figure A-2) and from which we have no observations of bed conditions. Either the areas adjacent to the trough generate little sediment relative to the trough itself, or any sediment generated is quickly routed to the trough. The trough is an obvious water routing pathway with water directed into its bottom by high gradients of hydraulic potential along its walls. Mobilisation of the concentrated sediment along the trough may be facilitated by both high water flux, and frequent variability in the direction and magnitude of potential gradients stemming from basal pressure variability (Wright et al. 2016). Another factor may be that during the last glacial maximum the shallower ice in highland areas may have been frozen to the bed, greatly reducing erosion (e.g. Staiger et al. 2005). Regardless, little water and sediment emerges from the ice across long reaches between the major outlets where deglaciated terrain includes widespread bedrock (granodioritic gneiss) ridges (Figure A-S5). Our work implies these conditions may extend under the ice for many 10s of km inland from the margin.

A6 Conclusions

Based on observations and experiments in 32 boreholes in the Kangerlussuaq sector of Western Greenland, the emergent view of bed and near-bed conditions across this region of the ablation zone is as follows: (a) the ice-bed interface is at the melting point and has high fluxes of liquid water; (b) sediment is commonly entrained into the lowermost few meters of ice; (c) the bed has heterogeneous sediment cover, with sediment decimeters thick in places, but not many meters thick. Some locations have no sediment cover; (d) the basal sediment consists mainly of sand and gravel. Most clay particles, and perhaps some silt particles, have been flushed; (e) Darcy flow through a permeable till layer is not a primary mechanism for water transport. Rather, water moves through discrete and high flux pathways, but not likely by flow through canals cut into sediment.

The subglacial drainage system along our transect of boreholes thus behaves as a hard bed with elements (e.g. cavities, orifices, conduits) that develop with respect to bedrock roughness and which are governed by hard bed physics. The recent history of deglaciation/advance, rapid routing of sediment to a deep bedrock trough by relatively high water flux, or relatively low erosion rates in the non-trough areas, may be reasons why this region has little basal sediment. Our results do not cast doubt on interpretations of a bed with thick sediment cover at other locations in Greenland. However, our findings clearly demonstrate that not all of Greenland can be considered to have a soft bed with ice flow dictated by deformation of a thick and mechanically weak basal sediment layer.

A7 Acknowledgments

This work is funded by Svensk Kärnbränslehantering AB, Stockholm Sweden; Posiva Oy, Eurajoki, Finland; Nuclear Waste Management Organization, Toronto, Canada; National Cooperative for the Disposal of Radioactive Waste, Wettingen, Switzerland, and; the U.S. National Science Foundation (PP-ANS grants 0909495/1203451). Data sets and accompanying descriptive information are published by the Swedish Nuclear Waste Management Company referenced by the Greenland Analogue Project at the following web address: http://www.skb.com/publications/.

A8 References

Alley R B, Blankenship D D, Bentley C R, Rooney S T, 1986. Deformation of till beneath ice stream B, West Antarctica. Nature 322, 57–59.

Aschwanden A, Fahnestock M A, Truffer M, 2016. Complex Greenland outlet glacier flow captured. Nature Communications 7, 10524. doi:10.1038/ncomms10524

Bartholomew I, Nienow P, Sole A, Mair D, Cowton T, King M A, 2012. Short-term variability in Greenland Ice Sheet motion forced by time-varying meltwater drainage: Implications for the relationship between subglacial drainage system behavior and ice velocity. Journal of Geophysical Research 117, F03002. doi:10.1029/2011JF002220

Blake E, Clarke G K C, Gérin M C, 1992. Tools for examining subglacial bed deformation. Journal of Glaciology 38, 388–396.

Blake E W, Fischer U H, Clarke G C K, 1994. Instruments and methods: Direct measurement of sliding at the glacier bed. Journal of Glaciology 40, 595–599.

Booth A D, Clark R A, Kulessa B, Murray T, Carter J, Doyle S, Hubbard A, 2012. Thin-layer effects in glaciological seismic amplitude-versus-angle (AVA) analysis: Implications for characterising a subglacial till unit, Russell Glacier, West Greenland. The Cryosphere 6, 909–922.

Bougamont M, Christoffersen P, Hubbard A L, Fitzpatrick A A, Doyle S H, Carter S P, 2014. Sensitive response of the Greenland Ice Sheet to surface melt drainage over a soft bed. Nature Communications 5, 5052. doi:10.1038/ncomms6052

Clark T S, Echelmeyer K, 1996. Seismic-reflection evidence for a deep subglacial trough beneath Jakobshavns Isbrae, West Greenland. Journal of Glaciology 43, 219–232.

Clarke G K C, 1987. Subglacial till: A physical framework for its properties and processes. Journal of Geophysical Research 92, 9023–9036.

Cowton T, Nienow P, Sole A, Wadham J, Lis G, Bartholomew I, Mair D, Chandler D, 2013. Evolution of drainage system morphology at a land-terminating Greenlandic outlet glacier. Journal of Geophysical Research: Earth Surface 118, 29–41.

Dow C F, Hubbard A, Booth A D, Doyle S H, Gusmeroli A, Kulessa B, 2013. Seismic evidence of mechanically weak sediments underlying Russell Glacier, West Greenland. Annals of Glaciology 54, 135–141.

Doyle S H, Hubbard A, Van De Wal R S W, Box J E, Van As D, Scharrer K, Meierbachtol T W, Smeets P C J P, Harper J T, Johansson E, Mottram R H, Mikkelsen A B, Wilhelms F, Patton H, Christoffersen P, Hubbard B, 2015. Amplified melt and flow of the Greenland ice sheet driven by late-summer cyclonic rainfall. Nature Geoscience 8, 647–653.

Engelhardt H, Humphrey N, Kamb B, Fahnestock M, 1990. Physical conditions at the base of a fast moving Antarctic ice stream. Science 248, 57–59.

Graly J A, Humphrey N F, Landowski C M, Harper J T, 2014. Chemical weathering under the Greenland Ice Sheet. Geology 42, 551–554.

Graly J A, Humphrey N F, Harper J T, 2016. Chemical depletion of sediment under the Greenland Ice Sheet. Earth Surface Processes and Landforms 41, 1922–1936.

Harrington J A, Humphrey N F, Harper J T, 2015. Temperature distribution and thermal anomalies along a flowline of the Greenland ice sheet. Annals of Glaciology 56, 98–104.

Hewitt I J, 2013. Seasonal changes in ice sheet motion due to melt water lubrication. Earth and Planetary Science Letters 371–372, 16–25.

Humphrey N, Echelmeyer K, 1990. Hot-water drilling and bore-hole closure in cold ice. Journal of Glaciology 36, 287–298.

Humphrey N, Kamb B, Fahnestock M, Engelhardt H, 1993. Characteristics of the bed of the Lower Columbia Glacier, Alaska. Journal of Geophysical Research: Solid Earth 98, 837–846.

Iken A, 1981. The Effect of the subglacial water pressure on the sliding velocisty of a glacier in an idealized numerical model. Journal of Glaciology 27, 407–421.

Iken A, Echelmeyer K, Harrison W, Funk M, 1993. Mechanisms of fast flow in Jakobshavns Isbrae, West Greenland: Part I. Measurements of temperature and water level in deep boreholes. Journal of Glaciology 39, 15–25.

Iverson N R, 2010. Shear resistance and continuity of subglacial till : Does hydrology trump rheology ? Journal of Glaciology 56, 1104–1114.

Kamb B, 1987. Glacier surge mechanism based on linked cavity configuration of the basal water conduit system. Journal of Geophysical Research 92, 9083–9100.

Kulessa B, Hubbard B, Williamson M, Brown G H, 2005. Hydrogeological analysis of slug tests in glacier boreholes. Journal of Glaciology 51, 269–280.

Lindbäck K, Pettersson R, Doyle S H, Helanow C, Jansson P, Kristensen S S, Stenseng L, Forsberg R, Hubbard A L, 2014. High-resolution ice thickness and bed topography of a land-terminating section of the Greenland ice sheet. Earth System Science Data 6, 331–338.

Lüthi M, Funk M, Iken A, Gogineni S, Truffer M, 2002. Mechanisms of fast flow in Jakobshavn Isbrae , West Greenland : Part III. Measurements of ice deformation , temperature and cross-borehole conductivity in boreholes to the bedrock. Journal of Glaciology 48, 369–385.

Meierbachtol T, Harper J, Humphrey N, 2013. Basal drainage system response to increasing surface melt on the Greenland ice sheet. Science 341, 777–779.

Meierbachtol T W, Harper J T, Humphrey N F, Wright P J, 2016. Mechanical forcing of water pressure in a hydraulically isolated reach beneath Western Greenland's ablation zone. Annals of Glaciology 57, 62–70.

Ng F S L, 2000. Canals under sediment-based ice sheets. Annals of Glaciology 30, 146–152.

Ohmura A, Reeh N, 1991. New precipitation and accumulation maps for Greenland. Journal of Glaciology 37, 140–148.

Palmer S, Shepherd A, Nienow P, Joughin I, 2011. Seasonal speedup of the Greenland Ice Sheet linked to routing of surface water. Earth and Planetary Science Letters 302, 423–428.

Röthlisberger H, 1972. Water pressure in subglacial channels. Journal of Glaciology 2, 177–203.

Ryser C, Luthi M P, Andrews L C, Catania G A, Funk M, Hawley R, Hoffman M, Neumann T A, 2014. Caterpillar-like ice motion in the ablation zone of the Greenland ice sheet. Journal of Geophysical Research: Earth Surface 119, 2258–2271.

Schoof C, 2010. Ice-sheet acceleration driven by melt supply variability. Nature 468, 803–806.

Simpson M J R, Milne G A, Huybrechts P, Long A J, 2009. Calibrating a glaciological model of the Greenland ice sheet from the Last Glacial Maximum to present-day using field observations of relative sea level and ice extent. Quaternary Science Reviews 28, 1631–1657.

Staiger J K W, Gosse J C, Johnson J V, Fastook J, Gray J T, Stockli D F, Stockli L, Finkel R, 2005. Quaternary relief generation by polythermal glacier ice. Earth Surface Processes and Landforms 30, 1145–1159.

Storms J E A, de Winter I L, Overeem I, Drijkoningen G G, Lykke-Andersen H, 2012. The Holocene sedimentary history of the Kangerlussuaq Fjord-valley fill, West Greenland. Quaternary Science Reviews 35, 29–50.

Sundal A V, Shepherd A, Nienow P, Hanna E, Palmer S, Huybrechts P, 2011. Melt-induced speed-up of Greenland ice sheet offset by efficient subglacial drainage. Nature 469, 521–524.

van Tatenhove F G M, van der Meer J J M, Koster E A, 1996. Implications for deglaciation chronology from new AMS age determinations in central west Greenland. Quaternary Research 45, 245–253.

Walder J S, 1986. Hydraulics of sub glacial cavities. Journal of Glaciology 32, 439–445.

Walder J S, Fowler A, 1994. Channelized subglacial drainage over a deformable bed. Journal of Glaciology 40, 3–15.

Walter F, Chaput J, Lüthi M P, 2014. Thick sediments beneath Greenland's ablation zone and their potential role in future ice sheet dynamics. Geology 42, 487–490.

Weertman J, 1972. General theory of water flow at the base of a glacier or ice sheet. Reviews of Geophysics and Space Physics 10, 287–333.

Werder M A, Hewitt I J, Schoof C G, Flowers G E, 2013. Modeling channelized and distributed subglacial drainage in two dimensions. Journal of Geophysical Research: Earth Surface 118, 2140–2158.

Wright P J, Harper J T, Humphrey N F, Meierbachtol T W, 2016. Measured basal water pressure variability of the western Greenland ice sheet: Implications for hydraulic potential. Journal of Geophysical Research: Earth Surface 121, 1134–1147.

A9 Supporting information

Table A-S1 provides overview of all borehole locations, depths and types of measurements made. Figures A-S1 to A-S5 display supporting results from additional experiments and observations to those presented in the main text.

Table A-S1. Borehole locations, depths, and the types of measurements collected in them.

Year	Number	Site	Hole	Date	"Depth (m)"	"Latitude (WGS 84)"	"Longitude (WGS 84)"	"Elevation (m)"	Nozzle	Stem	Pulses	Load	Drainage	Impulse	Sampler	Photo	Dye	Thermal	"Pw series"
2010	1	M1-10	GL10-1A	6-12-2010	98	67.162213	−50.06427	520	X	X	X	X	X			X			
	2	M1-10	GL10-1B	6-13-2010	92.5	67.162137	−50.06443	519	X	X	X	X	X			X			
	3	M1-10	GL10-1C	6-14-2010	91	67.162518	−50.06326	523	X	X	X	X	X	X		X			
	4	M1-10	GL10-1D	6-14-2010	98.5	61.162385	−50.06331	523	X	X	X	X	X	X		X			X
	5	M1-10	GL10-1E	6-16-2010	91.9	67.162524	−50.06291	525	X	X	X	X	X	X		X			
	6	M1-10	GL10-1F	6-17-2010	102	67.162662	−50.06204	532	X	X	X	X	X			X			
	7	M2-10	GL10-2A	6-20-2010	144	67.167033	−50.06654	554	X	X	X	X	X			X			
	8	M2-10	GL10-2B	6-21-2010	148.7	67.167093	−50.06654	554	X	X	X	X	X	X		X			X
	9	M2-10	GL10-2C	6-23-2010	146.3	67.167043	−50.06633	555	X	X	X	X	X	X		X			X
	10	M2-10	GL10-2D	6-23-2010	145.6	67.167119	−50.06617	555	X	X	X	X	X	X		X			
	11	M2-10	GL10-2E	6-25-2010	148.7	67.167147	−50.06639	556	X	X	X	X	X	X		X			
2011	12	27 km-11	GL11-1A	7-2-2011	457.5	67.195175	−49.71952	848	X	X	X	X	X	X	X				X
	13	27 km-11	GL11-1B	7-4-2011	466	67.195272	−49.71913	850	X	X	X	X	X	X	X				X
	14	27 km-11	GL11-1C	7-6-2011	459.5	67.19505	−49.71892	849	X	X	X	X	X	X	X				X
	15	46 km-11	GL11-2B	7-14-2011	821	67.201432	−49.2888	1092	X	X	X	X	X	X					X
	16	46 km-11	GL11-2C	7-17-2011	816	67.201284	−49.2893	1087	X	X	X	X	X		X				
	17	46 km-11	GL11-2D	7-18-2011	814.5	67.201336	−49.2891	1088	X	X	X	X	X	X					X
2012	18	M3-12	GL12-1A	6-7-2012	116.65	67.1593	−50.05928	482	X	X	X	X	X		X				X
	19	M3-12	GL12-1B	6-7-2012	114.45	67.1593237	−50.05911	483	X	X	X	X	X						X
	20	27 km-12	GL12-2A	6-13-2012	695.5	67.2042167	−49.71793	822	X	X	X	X	X		X				X
	21	27 km-12	GL12-2B	6-15-2012	710.5	67.20395	−49.71787	823	X	X	X	X	X	X	X				
	22	27 km-12	GL12-2C	6-17-2012	688	67.2037	−49.71778	827	X	X	X	X	X	X	X				X
	23	27 km-12	GL12-2D	6-20-2012	696	67.20386	−49.71807	825	X	X	X	X	X	X	X				X
2014	24	33 km-14	L14-South-	7-17-2014	674	67.181076	−49.57001	953	X	X	X	X	X	X			X	X	X
	25	33 km-14	L14-South-	7-19-2014	677	67.181044	−49.56972	952	X	X	X	X	X					X	X
	26	33 km-14	L14-West-H	7-22-2014	661	67.182086	−49.57238	953	X	X	X	X	X				X	X	X
	27	33 km-14	L14-North-	7-26-2014	641	67.183071	−49.5697	940	X	X	X	X	X					X	X
2015	28	33 km-15	15-C-A	7-6-2015	671	67.182104	−49.5695	948	X	X	X	X	X					X	X
	29	33 km-15	15-C-B	7-8-2015	675	67.182013	−4.96E+01	948	X	X	X	X	X					X	X
	30	33 km-15	15-S	7-11-2015	677	67.180939	−49.56666	948	X	X	X	X	X				X	X	X
	31	33 km-15	15-E-B	7-15-2015	665	67.181866	−49.56403	955	X	X	X	X	X				X	X	X
	32	33 km-15	15-N	7-17-2015	640	67.183124	−49.56691	963	X	X	X	X	X				X	X	X

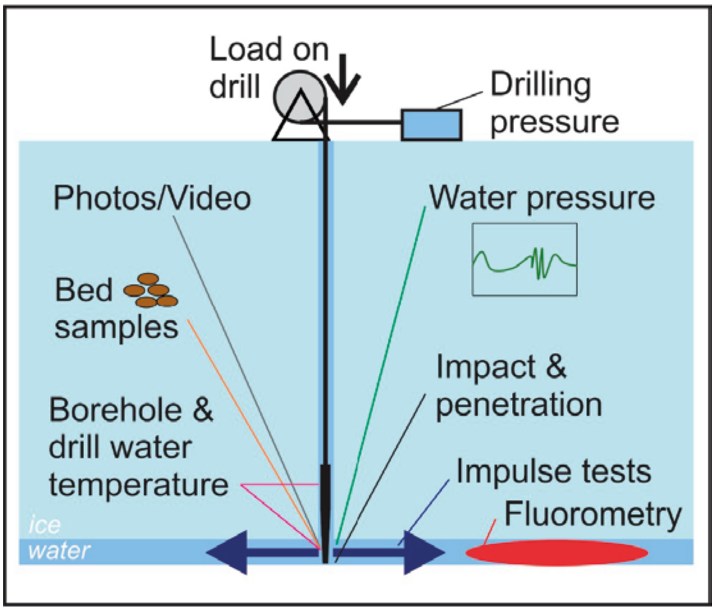

***Figure A-S1.** Overview of the various types of measurements used to reveal character of the interface between ice and bed.*

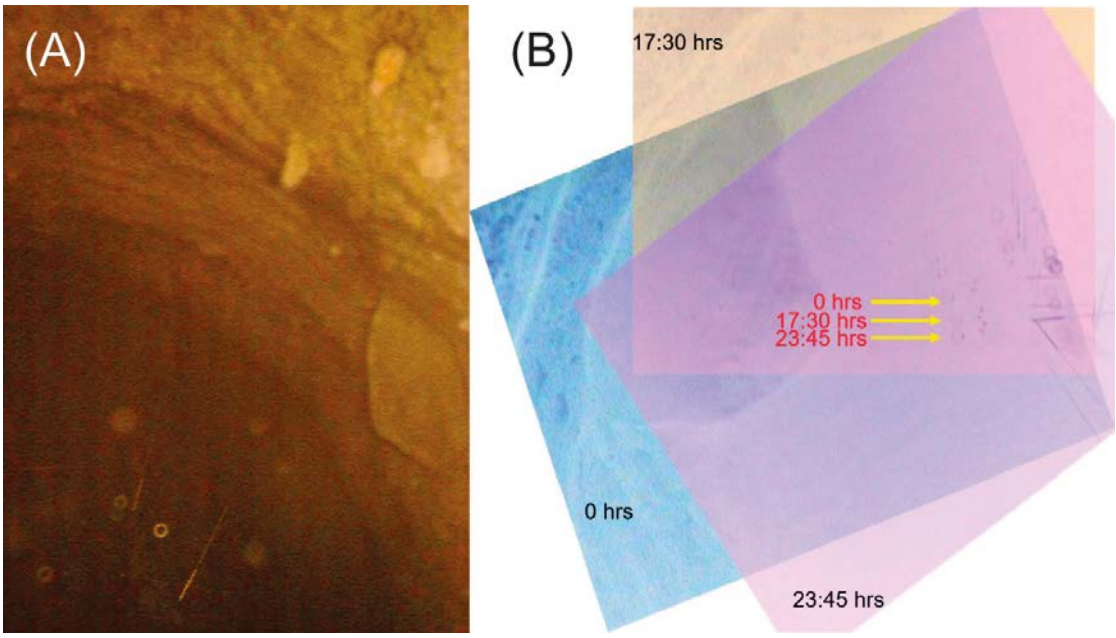

***Figure A-S2.** Example of time-lapse images of the bed used to observe basal sliding. Images are from site M2, located about 2 km from the ice margin where the ice depth is only 130 m. Images collected with a lighted waterproof still camera with data transmitted to the surface using RS-485 protocol via cat5e cable. A) Borehole camera image showing about 25 % of the borehole's circumference near the bed. The borehole walls in the lowest meter near the bed are composed of dirty ice. Various sized gravel protrudes from the borehole wall and the bed is visible at the lower left. Several nuts and bolts have been dropped down the hole to provide scale and are lying on the bed. The visible bolts are 7.6 cm (3 inches) long. Repeated viewing of the nuts, bolts and other key clasts indicates no deformational overturning of the basal sediment layer. B) Sequence of processed images showing displacement over a 24 hour period. The images have been color shifted and made transparent to allow overlapping comparisons. Each image has been registered with respect to borehole wall, which enables the relative motion of the bed to be determined using the nuts and bolts as reference points. The sliding speed over the 24 hour period was 2.6 cm per day, with negligible difference in speed in the two time periods delineated by the images.*

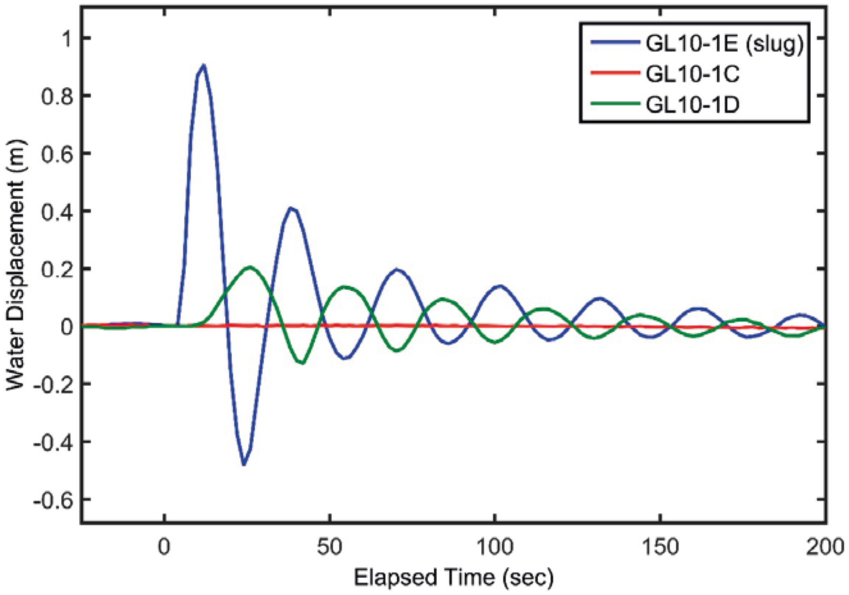

Figure A-S3. *Results of impulse test demonstrating variable transmissivity of subglacial pathways between boreholes. A 150 l slug of water was added to borehole GL10-1E in ~20 seconds (located at site M2). Out-of-phase oscillations occurred between the slugged borehole and Borehole GL10-1D, located 25 m away. These are interpreted to be 'sloshing' between the boreholes via a transmissive basal drainage system pathway. However, borehole GL10-1C, located 16 m away, showed no transmissive connection to the other two boreholes.*

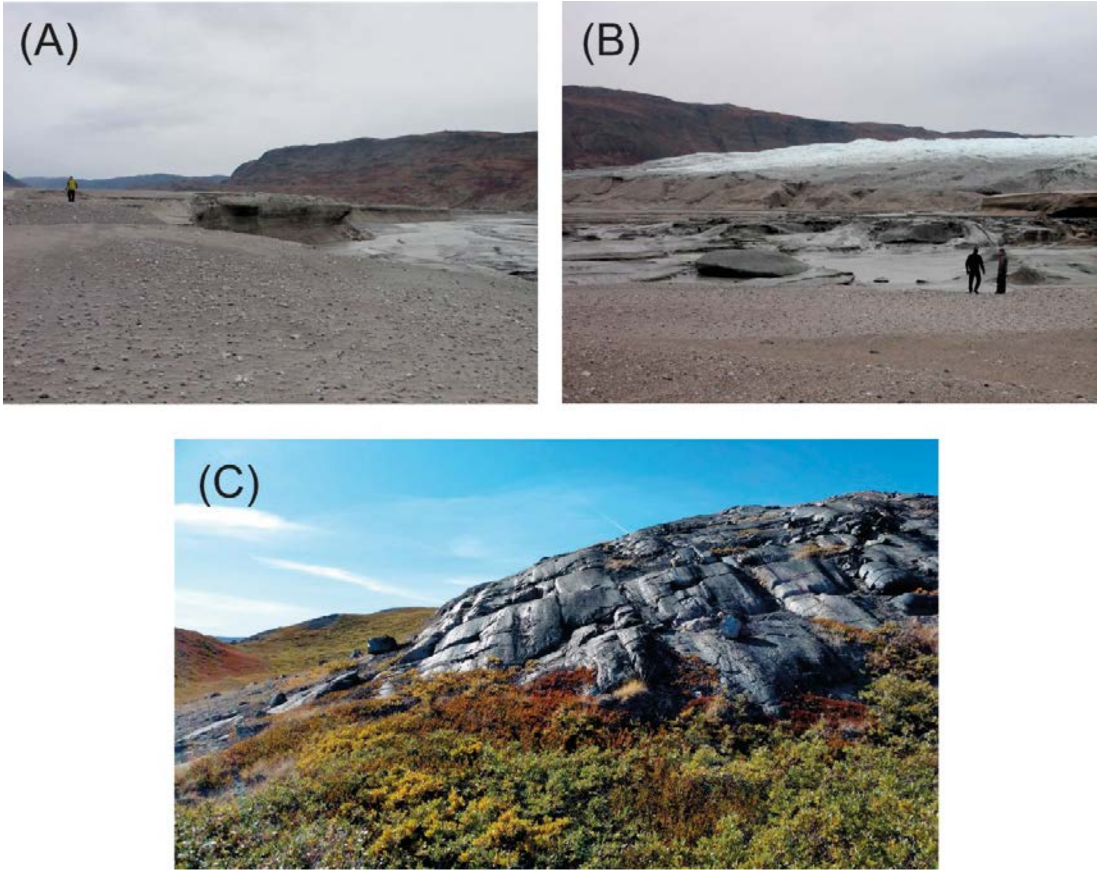

Figure A-S4. *Photographs showing end members of the glacial sediment observed at ice sheet margin in study area. (A) and (B) show high sediment flux from major outlet stream of Issunguata Sermia, the outlet of the deep bedrock trough extending under the ice of the study region; (C) shows an example of the common outcrops of glaciated bare bedrock at a location 0.5 km from the current ice margin near site M1.*

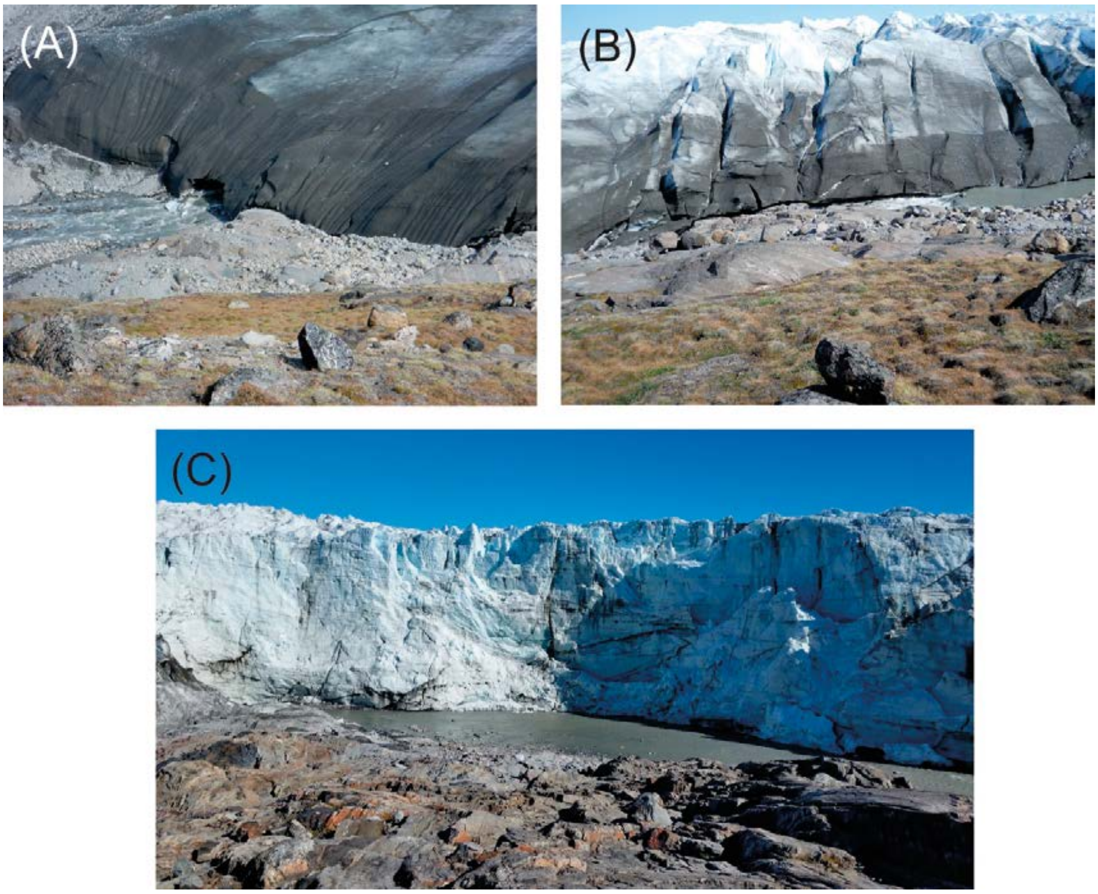

***Figure A-S5.** Photographs showing basal ice exposed at the ice sheet margin. (A) and (B) show margin area (near site M1) and (C) shows ice exposed at Russell Glacier located several km south of the study area.*

Appendix B

Measured basal water pressure variability of the Western Greenland Ice Sheet: implications for hydraulic potential

(**Wright P J, Harper J T, Humphrey N F, Meierbachtol T W, 2016.** Measured basal water pressure variability of the Western Greenland Ice Sheet: Implications for hydraulic potential. Journal of Geophysical Research: Earth Surface 121, 1134–1147.)

B1 Abstract

The gradient of the hydraulic potential field at the ice-bedrock interface beneath the Greenland Ice Sheet (GrIS) dictates the routing and energetics of subglacial water, thereby influencing drainage system characteristics and sliding dynamics. In the ablation zone of the GrIS, variable water pressure due to an active subglacial drainage system and basal topography with high relief potentially interact to drive unknown spatial patterns and temporal changes in the hydraulic potential field. Here we present a suite of water pressure measurements collected in thirteen boreholes along a 46 km transect on the western GrIS to investigate the role of spatial and temporal basal water pressure adjustments in hydraulic potential gradient dynamics. All borehole sites show pressures with similar seasonality, having relatively steady and high values during winter, variable and irregular behavior during spring and fall, and diurnal cycles that can persist for multiple weeks during the peak melt season. Despite much higher variability during the melt season, the median pressure of the summer period is nearly the same as the median pressure of the winter period. However, time variability of water pressure due to basal drainage processes can force changes in the magnitude and orientation of the hydraulic potential field over diurnal periods. We find the basal water pressure across the transect generally mimics the ice thickness field, but with superimposed large pressure gradients that develop at shorter scales within the basal drainage system. This leads to a complex hydraulic potential field across regions of similar ice thickness.

B2 Introduction

The subglacial drainage system imparts a key control on the sliding speed of the Greenland Ice Sheet (GrIS) by dictating the variability of basal water pressure and areas of coupling between the ice sheet and its bed. The drainage system evolves seasonally (e.g. Hoffman et al. 2011) in response to input of surface melt, which rapidly reaches the bed via moulins and crevasses (Catania and Neumann 2010, Das et al. 2008, McGrath et al. 2011). Active subglacial drainage systems likely evolve inward from the margin (e.g. Chandler et al. 2013), establishing networks of channelised and distributed drainage elements which define drainage basin areas. The routing of water in these networks is set by the direction and magnitude of the hydraulic potential gradient. In order to determine potential gradients, and hence the broad constraints on basal water flow, the bed topography and basal water pressure field must be well known (see Section B3).

Several reviews of subglacial hydrology in alpine glacier settings (e.g. Fountain and Walder 1998, Hooke 1989, Hubbard and Nienow 1998) have evaluated seasonal evolution of borehole water pressure records and provided interpretations for water routing and glacier sliding. Although a wide body of previous work has established important foundations for understanding subglacial water flow, prior alpine glacier findings have uncertain application to large ice sheets where thick ice can induce rapid creep closure, water flows at the bed over many 10s of km, and critically, relatively shallow surface slopes (e.g. often 1° or less) drive water flow, sometimes over high relief bed topography. Early borehole measurements in GrIS revealed basal water pressure near overburden, but records typically spanned only a few days (Iken et al. 1993, Thomsen and Olesen 1990, 1991, Thomsen et al. 1991). Only recently have measurements become more temporally and spatially extensive, and have demonstrated that water pressure undergoes diurnal cycles and seasonal variability (Andrews et al. 2014, Lüthi et al. 2002, Meierbachtol et al. 2013, van de Wal et al. 2015).

Recent development of bed DEMs using radar and mass conservation techniques have revealed basal topography beneath the GrIS with much greater relief than previously assumed (Bamber et al. 2013, Lindbäck et al. 2014, Morlighem et al. 2014). In particular, the ablation zone of the western GrIS is characterised by reaches with steep-walled bedrock troughs. The ice surface remains relatively smooth in these regions, with shallow surface slopes and only muted expressions of bedrock topography, resulting in highly variable ice thickness. Despite the increasing fidelity of topographic data, however, a lack of constraints on basal water pressure continues to invoke large uncertainty in hydraulic potential gradients.

In this study we use measurements collected in thirteen boreholes to assess temporal and spatial scales of basal water pressure variability along a 46 km transect in Western Greenland. Borehole records collected during 2010–2015 span summer and winter periods and include six sites ranging from near-margin to inland conditions. As such, the records permit assessment of spatial pressure gradients at the site- to regional-scale as well as temporal changes over daily and seasonal periods. We use these results to examine the sensitivity of the potential gradient field to variability in water pressure.

B3 Gradients of water pressure and hydraulic potential

Hydraulic potential is composed of an elevation potential and a pressure potential

$$\phi_h = \rho_w g z_b + P_w \tag{B-1}$$

where P_w is water pressure, Z_b is the bed elevation, ρ_w is density of water, and g is the acceleration due to gravity. Multiplying P_w in Equation (B-1) by (P_i/P_i) allows the pressure term to be equivalently expressed as a fraction of the ice overburden pressure

$$\phi_h = \rho_w g z_b + \rho_i g H \frac{P_w}{P_i} \tag{B-2}$$

where H is ice thickness $(z_s - z_b)$, P_i is ice overburden pressure, and ρ_i is ice density. The hydraulic potential gradient is then defined by the negative gradient of ϕ_h

$$-\nabla\phi_h = -\rho_w g \nabla z_b - \rho_i g \nabla H \frac{P_w}{P_i} - \rho_i g H \nabla\left[\frac{P_w}{P_i}\right] \tag{B-3}$$

The third term on the right side of the expression is nearly always neglected by invoking the assumption that basal water pressure gradients are solely a function of the ice overburden. The basal water pressure is then either set equal to the ice pressure, or is sometimes allowed to deviate as a spatially invariant fraction of overburden pressure. Equation (B-3) is then commonly approximated (e.g. Cuffey and Paterson 2010, Shreve 1972) by

$$-\nabla\phi_h = -\rho_i g\left[\frac{P_w}{P_i}\nabla z_s + \left[\frac{\rho_w}{\rho_i} - \frac{P_w}{P_i}\right]\nabla z_b\right] \tag{B-4}$$

The above expression relates basal water pressure gradients directly to changes in ice thickness, as derived from surface and bed topography via ∇z_s and ∇z_b. In other words, Equation (B-4) represents situations where the water pressure field mimics the ice thickness field, or some spatially invariant fraction thereof. Equation (B-4) has been applied to Greenland at the basin scale (e.g. Lindbäck et al. 2015, Tedstone et al. 2014) and the ice sheet scale (Lewis and Smith 2009, Liston and Mernild 2012, Livingstone et al. 2013) to delineate drainage basins and associated sediment and water fluxes. Adjustment of water pressure has been found to strongly impact the computed potential gradients (Lindbäck et al. 2015).

In situations where bed slopes are steep and pressures are high, the critical role of water pressure in determining potential gradients is illustrated by a comparison of the ratio of the surface gradient multiplier $[P_w/P_i]$ to the bed gradient multiplier $[(\rho_w/\rho_i) - (P_w/P_i)]$ under varying water pressure (Figure B-1). The relationship is highly nonlinear such that small changes in water pressure at values near overburden result in large changes in the hydraulic potential gradient if the disparity between surface and bed slopes is substantial. As shown later, these conditions are common in Western Greenland.

A second complication to hydraulic potential gradients of Western Greenland stems from the basal drainage system, which may develop strong water pressure gradients that are unrelated to ice thickness: i.e. the third term in Equation (B-3) may be large. Strong pressure gradients in the subglacial drainage system are often induced by basal processes such as water flux imbalances, melt-back of ice walls, creep closure of the ice roof, and cavity opening from sliding. Pressure gradients have been observed by direct measurement (e.g. Andrews et al. 2014, Meierbachtol et al. 2013) implying active basal processes in Greenland, and have also been inferred from physics-based modeling of drainage system evolution (e.g. Hewitt 2013, Hewitt et al. 2012, Werder et al. 2013). Modeling work has also suggested that water pressure gradients can be induced from spatially variable normal stress in the ice resulting from stress transfer between slippery and sticky patches at the bed (Ryser et al. 2014a, b). Furthermore, these spatial water pressure gradients are subject to the additional complication that water pressure may vary in time due to seasonally and diurnally varying melt input.

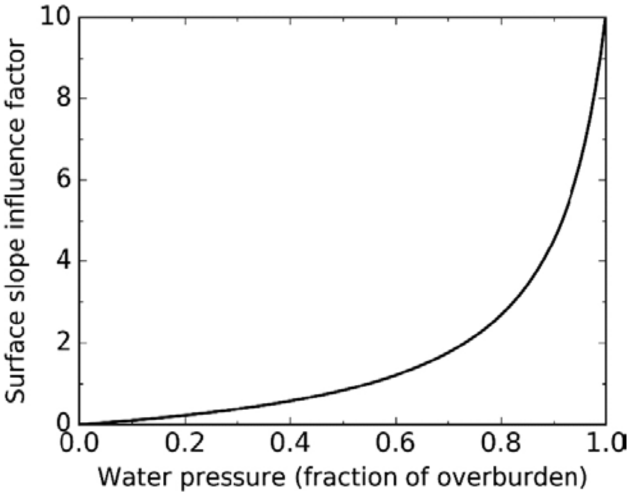

***Figure B-1.** Influence of ice surface slope on the total hydraulic potential gradient as a function of basal water pressure. "Surface slope influence factor" of 1 indicates that surface slope and bed slope contribute equally to the total potential gradient. A factor of 10 indicates that the surface is 10x more influential than the bed.*

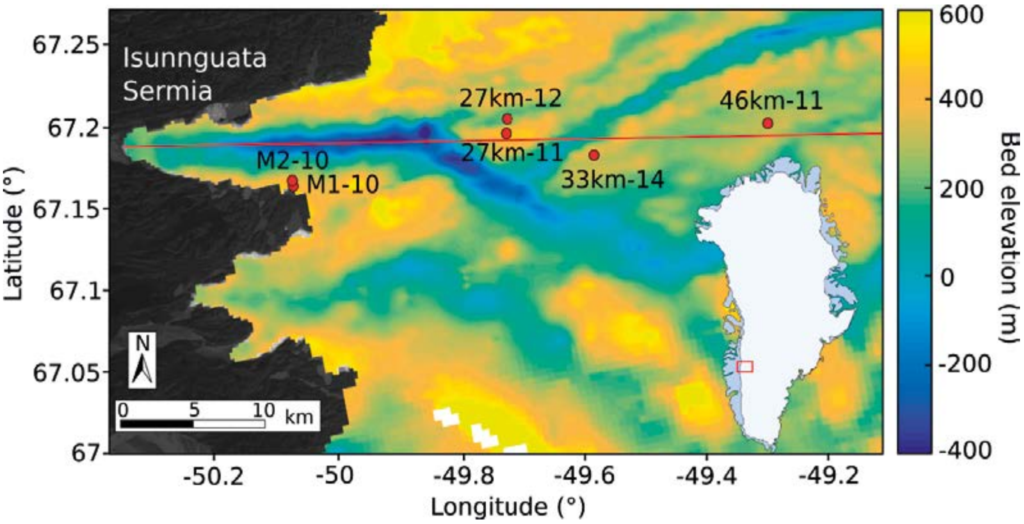

***Figure B-2.** Locations of borehole sites along the study transect in Western Greenland, shown with 250-m resolution bed topography (Lindbäck et al. 2014). Red line indicates the profile line in Figure B-11.*

The hydraulic potential gradient at the bed of GrIS is therefore expected to be strongly controlled by details of the water pressure field and its time and space gradients: $\nabla\phi_h$ should be sensitive to small changes in the magnitude of pressure because of steep bed slopes, and $\nabla\phi_h$ may also be sensitive to non-overburden related pressure gradients which arise from basal processes and seasonal development of a basal drainage system. Our working knowledge of these details, however, is quite limited owing to few observations of subglacial water pressure.

B4 Methods

Boreholes were drilled using hot water methods at six locations along a transect moving inland from Isunnguata Sermia, on the southwest margin of the GrIS (Figure B-2). For the borehole locations described below, all distances inland are reported as distance from the terminus of Isunnguata Sermia. Boreholes are named as [distance]-[2-digit year][letter], according to distance inland (km), 2-digit year of drilling, and a letter identifier for multiple boreholes at each site.

Three boreholes drilled in 2010 at two near-margin locations are identified separately (M1-10, M2-10A, and M2-10B). These sites are approximately 12 km from the terminus of Issunguata Sermia, however they are located very near the lateral margin at a point where Isunnguata Sermia exits the main body of the ice sheet. Boreholes M2-10A and M2-10B are co-located within ten m, and are approximately 1 km from the lateral margin (ice depth ~150 m), and borehole M1-10 is located approximately 450 m from the lateral margin (ice depth ~100 m).

Sites 27km-11 and 27km-12 are located approximately 27 km inland (drilled in 2011 and 2012, respectively). 27km-11 overlies a ridge in bedrock topography (ice depth ~460 m), and is located approximately 1 km south of site 27km-12, which overlies a bedrock trough (ice depth ~700 m). Three boreholes at each site are co-located within 20–30 m. Site 33km-14 (ice depth ~670 m) has two boreholes co-located within 150 m and overlies a high plateau in bedrock topography with a major northeast-southwest trending bedrock trough north of the site. Site 46km-11 (ice depth ~820 m) has two boreholes co-located within 20 m, and is located ~30 km below the long term equilibrium line altitude (ELA) (van de Wal et al. 2012). Appropriate drilling speed determined by monitoring the drill stem's load on the drill tower ensures that boreholes are drilled vertically with a free-hanging lead drill stem (Humphrey and Echelmeyer 1990), such that distances between co-located boreholes at the surface are equivalent to distances at the bed. Distance inland, latitude, longitude, ice depth, and length of record for each borehole are listed in Table B-1.

Hole depth was confirmed with three independent measurements: depth marks on the drill hose, depth marks on instrumentation cable lowered down the borehole, and depth from a digital odometer on the drill. From these measurements, we estimate the accuracy of reported borehole depths to be <1.5 % of total ice thickness (±2 m for margin locations, ±12 m for inland locations). Additional details of borehole drilling and instrumentation methods are described by Meierbachtol et al. (2013) (supplementary material).

Boreholes were instrumented near the bed with pressure transducers logging at 5 or 15 minute intervals during summer and 15 or 30 minute intervals during winter. Pressure transducers were lowered to a position ~25–50 cm above the bed, with boreholes then freezing shut except near the bed where temperature measurements at each site show the ice is temperate (Harrington et al. 2015). The length of pressure records is limited by the connection of the sensor cables, which can fail due to stretching or rupture from crevassing at near-margin locations.

Water pressure is most commonly reported in this study as a fraction of overburden (OB) pressure. For all calculations, we assume an ice density of 910 kg m^{-3}. However, ice density can vary due to air bubbles, liquid water, or debris and impurities, and can commonly range between 880–917 kg m^{-3} (Cuffey and Patterson 2010). Uncertainty is analyzed for the combined maximum and minimum errors due to pressure transducer resolution (±0.1 m), ice depth measurements, and ice density. Resulting uncertainty in scaled overburden calculations varies slightly as a function of ice depth, with a maximum range from all error sources for our deepest borehole of −0.022 OB to +0.047 OB. This uncertainty is predominantly a function of the possible range in values for ice density. If the range of ice density is constrained to 900–917 kg m^{-3}, the maximum range in uncertainty is reduced to −0.022 OB to +0.026 OB.

Table B-1. Location, ice depth, and length of record for all boreholes.

Borehole[a, b]	Latitude (°)	Longitude (°)	Ice Depth (m)	Length of Record (yyyy-mm-dd) (# days)
M1-10	67.162	−50.063	99	2010-06-15 to 2010-09-20 (98)
M2-10A	67.167	−50.067	149	2010-06-22 to 2010-09-20 (91)
M2-10B	67.167	−50.066	146	2010-06-26 to 2010-09-11 (78)
27km-11A*	67.195	−49.720	458	2011-07-10 to 2012-07-10 (367)
27km-11B	67.195	−49.719	466	2011-07-10 to 2011-09-14 (67)
27km-11C	67.195	−49.719	460	2011-07-10 to 2011-09-14 (67)
27km-12A*	67.204	−49.718	696	2012-06-16 to 2013-07-23 (403)
27km-12B*	67.204	−49.718	688	2012-06-17 to 2013-07-16 (395)
27km-12C*	67.204	−49.718	696	2012-06-21 to 2013-07-16 (391)
33km-14A	67.182	−49.575	674	2014-07-17 to 2014-08-08 (23)
33km-14B*	67.182	−49.575	661	2014-07-27 to 2015-04-22 (270)
46km-11A	67.201	−49.289	821	2011-07-15 to 2011-09-14 (62)
46km-11B	67.201	−49.289	815	2011-07-20 to 2011-09-14 (57)

a Borehole ID format is: [distance]-[2-digit year][multiple borehole letter], where M1 and M2 are near-margin sites, distance (km) for remaining sites is distance from Issunguata Sermia terminus, and 2-digit year indicates beginning of record for each borehole.

b (*) indicates boreholes with over-winter records shown in Figures B-3 and B-8.

B5 Water pressure results

B5.1 Seasonal phases

Borehole water pressure throughout the transect shows characteristic seasonal phases, with a clear distinction between melt season and winter behavior (Figure B-3). Winter water pressure is characterised by a confined range that dominates for nearly eight months of the year. Pressure during winter commonly shows low-frequency variability over weeks and months, although in one case bimodal behavior is observed, with a sudden increase of nearly 0.07 OB (44 m head) over a five day period (borehole 27km-12B; Figure B-3c). The winter record for borehole 33km-14B (Figure B-3e) is an outlier in behavior from other winter records, showing two cycles with a range of 0.12 OB (75 m head) evolving over 2–3 month periods.

The melt season includes an initial spring phase, a period of regular diurnal cycles, and a fall “shut-down” phase. In the spring the winter-melt season transition is distinct, characterised by a sudden sharp increase in pressure usually occurring in early June. In two boreholes (27km-11A, 27km-12A) the spring activation event is 0.005–0.02 OB in magnitude (3–6 m head), which is subsequently followed within days or weeks by further pressure increases. The spring event in two boreholes, 27km-12B and 27km-12C, consists of a single rapid increase of 0.03–0.04 OB (17–26 m head). Spring events often record the maximum pressure values for an annual period; for example, the spring activation event in 2013 for borehole 27km-12B (Figure B-3c) reaches a maximum pressure of 1.08 OB.

The period of summer diurnals weakens and becomes more irregular in late August or September, defining a transition to fall behavior. The fall phase is often characterised by an evolution to higher pressures and a dampening of diurnal variability over a period of weeks until a relatively constant pressure is reached and sustained into winter, indicating the melt season-winter transition.

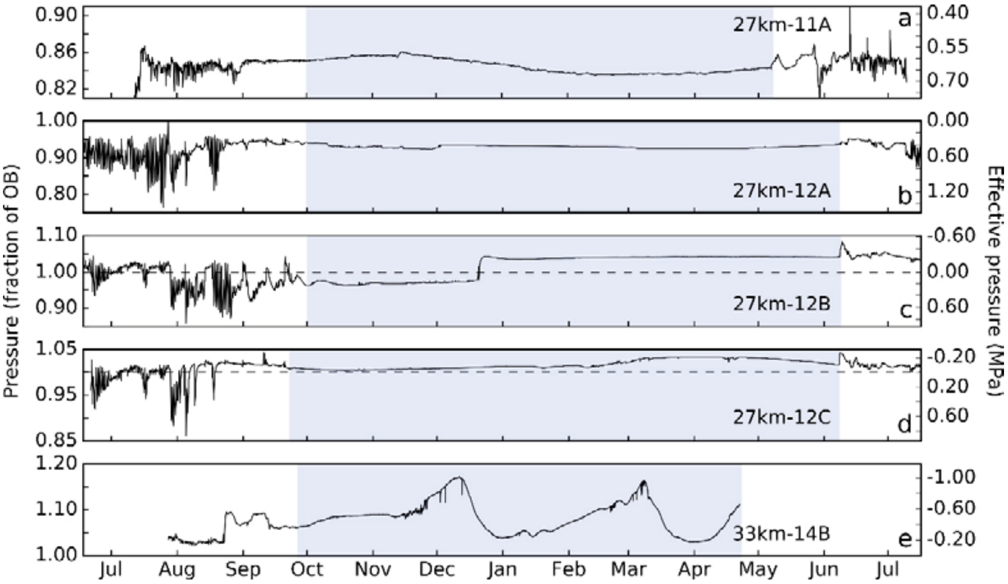

Figure B-3. *Annual water pressure records from boreholes 27km-11A (Panel a), 27km-12A (Panel b), 27km-12B (Panel c), 27km-12C (Panel d), and 33km-14B (Panel e). The characteristic winter period for each record is shaded in blue. Note that y-axis scales differ between panels to highlight details of individual records.*

B5.2 Diurnal cycles

All boreholes show periods of regular diurnal variability during mid-summer (Figures B-3, B-4). However, the magnitude and range of diurnal swings can be highly variable between boreholes, and does not necessarily follow a perfect sinusoid. For example, three distinct end-member types of diurnal cycles were observed: a symmetric mode where time is equally partitioned across the pressure range; a high-pressure dominated mode, where higher pressures occupied a greater fraction of the day; and a low-pressure dominated mode, where more of the day was occupied by lower pressure (Figure B-5).

Histograms based on five-day detrended periods demonstrate the difference between the three cases in the time-distribution of water pressure. In the symmetric mode (Figure B-5a), water pressure resides at high and low magnitudes for approximately equal portions of the diurnal cycle (51 % below, 49 % above). In the high-pressure dominated mode (Figure B-5b) water pressure is sustained above the median value for 73 % of the period, and in the low-pressure dominated mode (Figure B-5c) pressure remains below the median value for 58 % of the period. There is no clear dominance of one type of behavior across the transect, however the mode that is established for an individual borehole tends to stay consistent throughout the summer diurnal period (Figure B-4).

Regardless of the shape of diurnal variability, 12 of the 13 boreholes show diurnal cycles that are predominantly confined to a distinct range of 0.8–1.1 OB (Figure B-6). Once diurnal cycles are established, minimum pressures reached during July or August are typically the lowest pressures of the annual record for a borehole. A low pressure of 0.76 OB reached during late July in borehole 27km-12A (Figure B-3b) defines the minimum pressure recorded in the twelve-borehole suite. However, we see no evidence for consistent sub-seasonal decreasing trends in the magnitude of diurnal maximum or minimum pressures. Periods of diurnal cycles can show occasional multi-day trends of slightly increasing *or* decreasing pressure, but each pressure record remains constrained within the range throughout the melt season (Figure B-6).

Pressure data from borehole M1-10 are unique from the other 12 records. Located just 450 m from the lateral margin of Isunnguata Sermia with an ice depth of 99 m, water pressure records at this site show large diurnal pressure swings (68 m head), reaching a melt season minimum near 0.3 OB, yet with daily maximum pressures remaining above overburden throughout the melt season. Despite low minimum pressures, the median pressure for the entire record remains high at 0.86 OB, largely due to diurnal maximums consistently near overburden throughout the melt season.

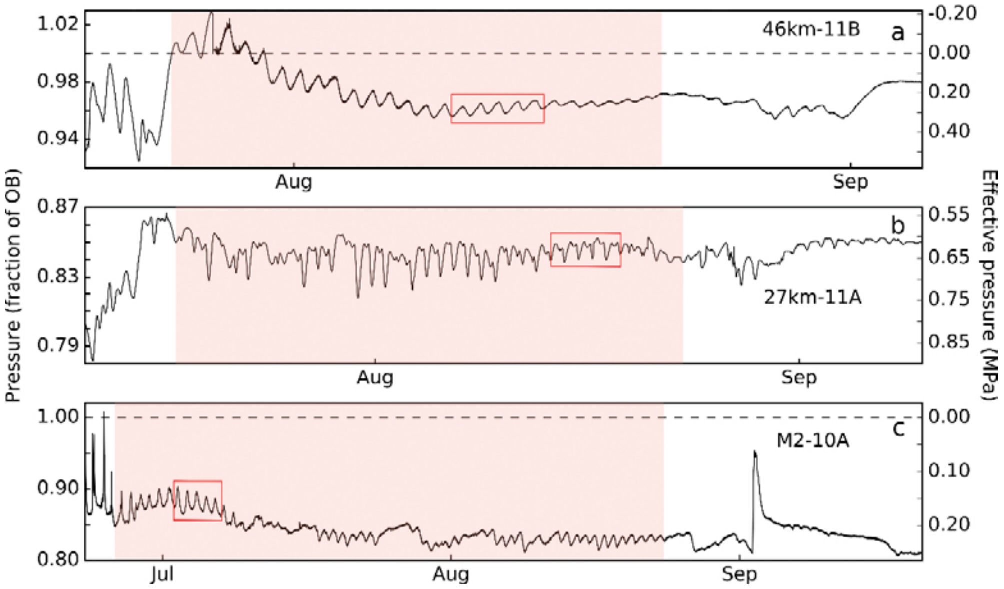

***Figure B-4.** Melt season water pressure records for boreholes 46km-11B (Panel a), 27km-11A (Panel b), and M2-10A (Panel c). The period representing "summer diurnals" for each record is shaded in red. Five day periods selected for diurnal analysis (Figure B-5) are indicated with red boxes. Note that y-axis scales differ between panels to highlight details of individual records.*

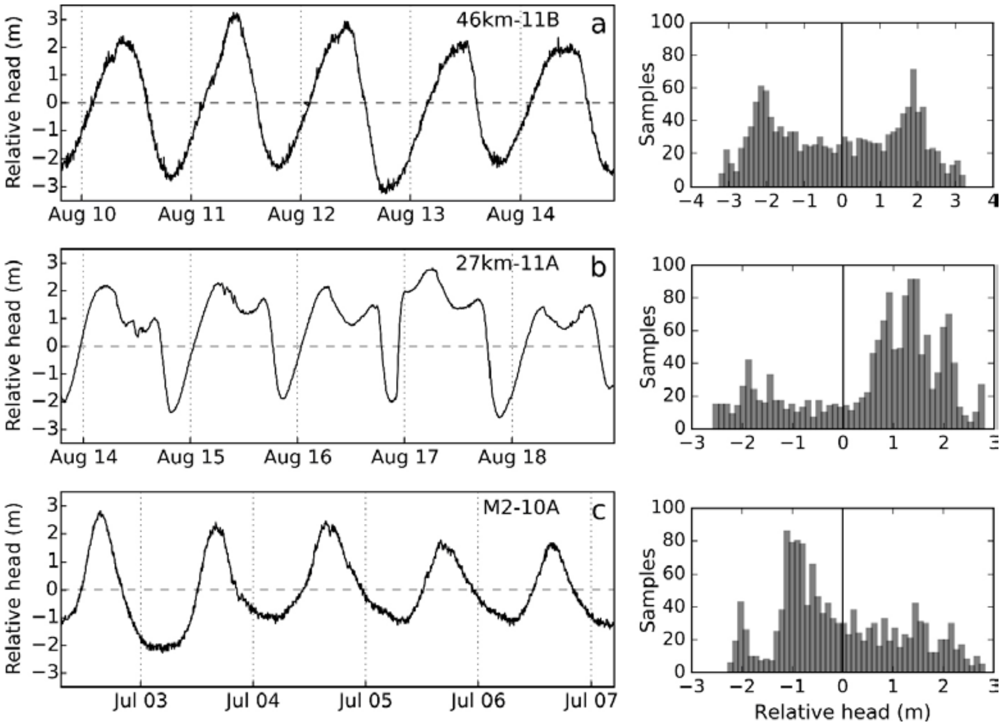

***Figure B-5.** Three modes of diurnal water pressure variability, corresponding to five day periods indicated in Figure B-4. Panel (a) represents a symmetric mode from site 46km-11B. Panel (b) represents a high-pressure dominated mode from site 27km-11A. Panel (c) represents a low-pressure dominated mode from site M2-10A. Corresponding histograms show distribution of data.*

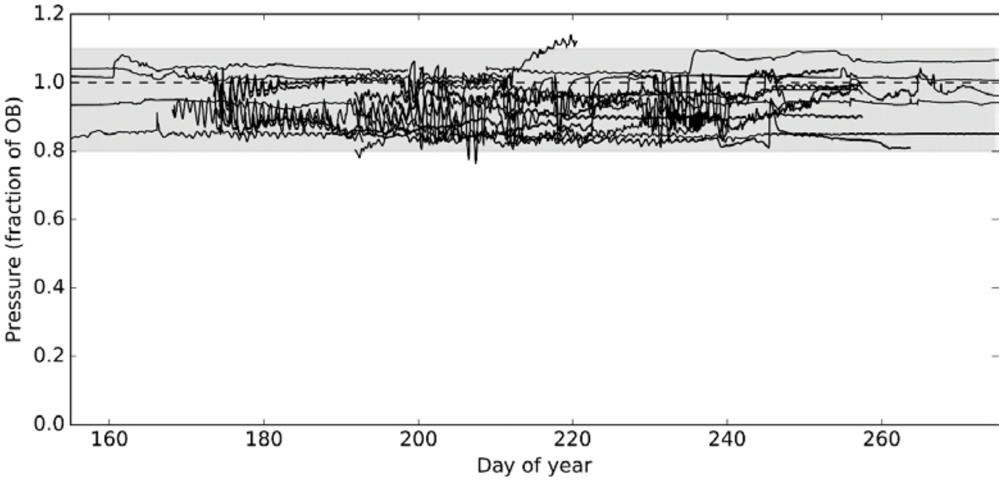

Figure B-6. Melt season basal water pressure records from all 12 boreholes showing limited range of variability. Near-margin, shallow-ice borehole M1-10 is interpreted to be an outlier as described in the text, and omitted here. All pressure records throughout the transect are confined to a range of approximately 0.8–1.1 of overburden pressure, as indicated by the shaded region.

B5.3 Spatial gradients

Our measurements demonstrate that substantial gradients in water pressure can exist between adjacent boreholes spaced 10s to 100s of m apart. Pressure differences arise from hole-specific temporal fluctuations occurring over time periods of hours to weeks. For example, boreholes 46km-11A and 46km-11B are co-located within 20 m and both boreholes show consistent diurnal cycles (Figure B-7). However, the two pressure records are consistently offset throughout the melt season by ~0.06 of OB (~40 m head). This difference in head represents a water pressure gradient of ~20 kPa m^{-1}. Because the ice thickness measured directly in the boreholes differs by only 6 m, these gradients can only be attributed to basal drainage system processes (the overburden pressure gradient is an order of magnitude less).

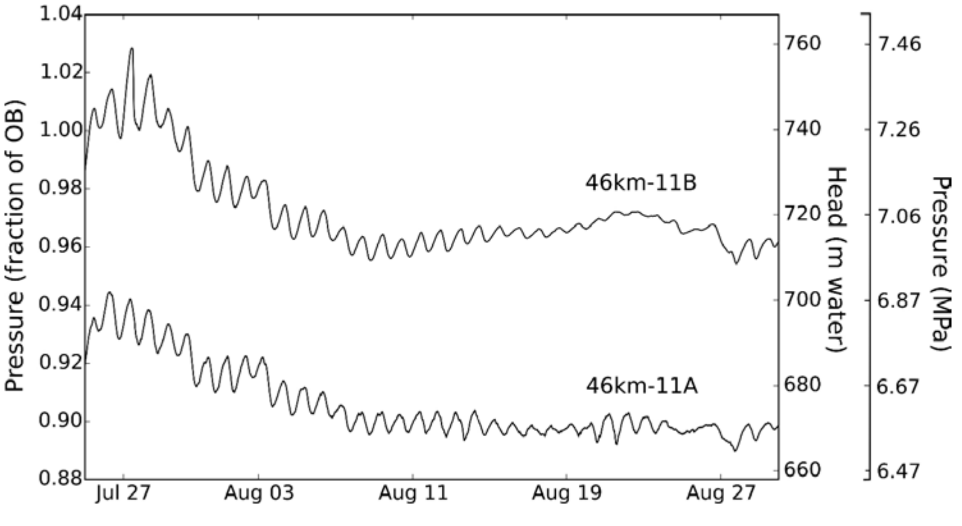

Figure B-7. Pressure records during 2011 from boreholes 46km-11A (ice depth 821 m) and 46km-11B (ice depth 815 m). Boreholes are co-located at the site within 20 meters.

Boreholes spaced 10s to 100s of m apart can show pressure differences within the same range of values (~0.8 to >1.0 OB) as sites 10s of km apart, when expressed as a fraction of the overburden pressure (the exception is the near margin hole, which we argue in Section 5.1 is a special case). The pressure potential, however, shows very large changes across the study domain driven by overall changes in ice sheet thickness. Long length scales between sites yield potential gradients averaging 0.16 kPa m^{-1} as ice thins towards the margins. Despite the fact that large local drainage system-driven pressure gradients are not upheld over longer inter-site length scales, very large changes in ice thickness, such as those existing along walls of steep bedrock troughs, can generate pressure gradients over 100s of m that are nearly 20 times greater than the overall transect gradient.

B5.4 Summary statistics

Box plots summarizing all pressure records from each borehole demonstrate no consistent trends in scaled overburden pressure as a function of ice thickness or distance inland from the margin (Figure B-8). In some cases, boreholes with thicker ice and greater distance inland clearly show higher pressures than more near-margin, shallower locations. For example, boreholes at sites 27km-12 and 33km-14 generally show pressures that are higher than at sites M2-10 and 27km-11. However, evidence for the opposite relationship is equally common. The melt season record of borehole M2-10B shows consistently higher pressure than two of three boreholes at site 27km-11, with ice thickness that is 300 m less and a location 15 km nearer to the margin. In addition, both boreholes at the most inland site (46km-11) show pressures that are lower than all boreholes at site 33km-14 and lower than two of three records at site 27km-12. Similarly, no spatial trends are obvious during the period of diurnal pressure swings (Figure B-9).

To assess seasonal evolution of water pressure from the winter to the melt season, we separate winter and melt season data for the five boreholes with annual records (indicated with shaded boxplot pairs in Figure B-8). For three of these boreholes there is essentially no change from winter to melt season median pressure (<0.01 OB), and in borehole 33km-14B the winter median pressure decreases by only 0.02 OB. This consistent seasonal behavior has exception only in borehole 27km-12B, showing a decrease from winter to melt season median pressure of 0.07 OB resulting from distinct bimodal winter behavior for this borehole which establishes a relatively high median for the winter record (Figure B-3c).

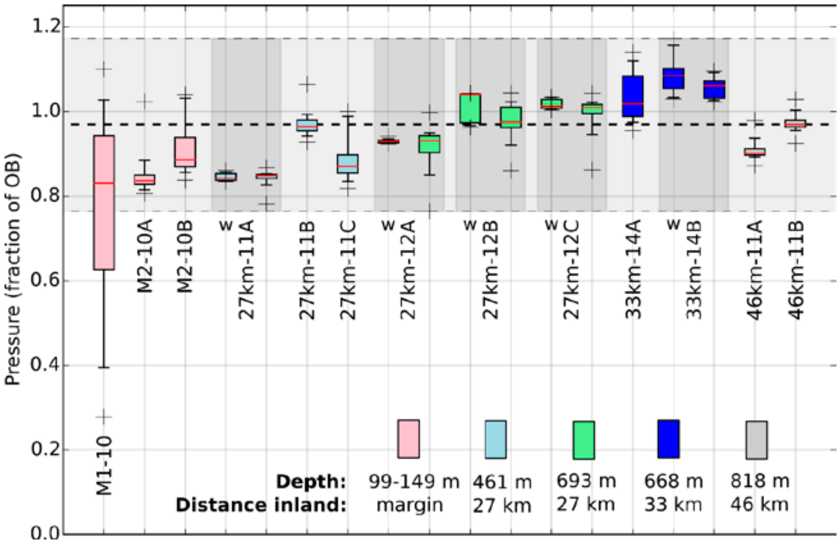

Figure B-8. *Box plots of basal water pressure data for all boreholes, where box color corresponds to distance from terminus (see Figure B-2). For boreholes with over-winter records, corresponding winter and melt season periods are shown in shaded pairs, where winter records are indicated with "w". For boreholes with only melt season records, all data in the record are represented. Box center lines are median, boxes span the 1st and 3rd quartiles, whiskers extend to 5th and 95th percentiles, and crosses indicate max and min points. Thick dashed line is the weighted annual mean and shaded region spans the minimum and maximum values of the 12-borehole suite (excepting hole M1-10).*

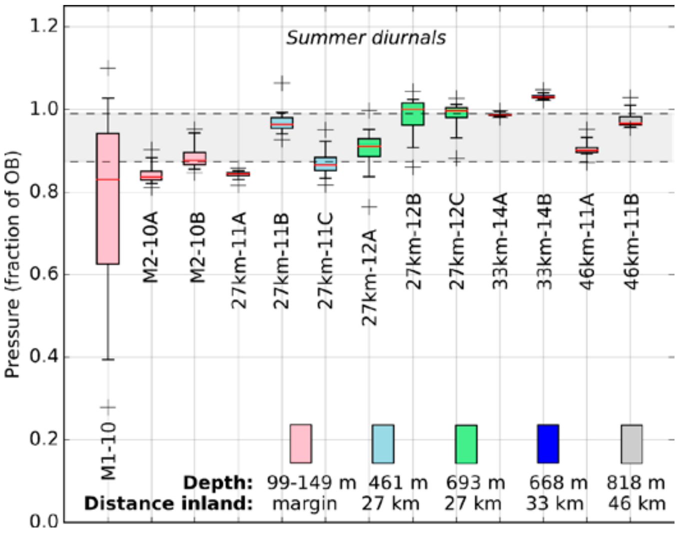

Figure B-9. *Box plots of water pressure data for the "summer diurnal" period, where box color corresponds to distance from terminus. Shaded region is the imposed diurnal range used for sensitivity testing of the hydraulic potential gradient (5th to 95th percentile from borehole 27km-12B, centered at the dataset mean median). Box center lines are median, boxes span the 1st and 3rd quartiles, whiskers extend to 5th and 95th percentiles, and crosses indicate max and min points.*

The minimum and maximum values recorded in the twelve-borehole suite are 0.76 OB and 1.17 OB, respectively (shaded region in Figure B-8). The annual weighted mean pressure for the transect remains near overburden at 0.97 OB (Figure B-8, thick dashed line). This calculation of the annual mean is supported by all data in the twelve-borehole suite (data from borehole M1-10 are not included for reasons discussed in Section 5.1), but this result may be biased by the weighting method (see Supplementary Information), where the winter and melt season are each assigned a fixed period of the year which may be an inaccurate representation of the actual seasonal timing for a given site. For comparison, we also present a simple calculation of annual mean pressure using only the four boreholes with year-long records. Averaging the median values of annual data re-sampled to thirty minute intervals for the full record of these boreholes, the annual mean is only 0.01 OB lower at 0.96 OB. Either treatment of the dataset therefore constrains the annual mean pressure between 0.96–0.97 OB.

B6 Discussion

B6.1 Representativeness of borehole pressures

The basal water pressure summary statistics presented here rely on borehole measurements that sample small areas of the bed at specific locations, and are limited to the seasonal characteristics that may be unique to the years of measurement. This brings into question how representative these results are in both time and space. Several lines of evidence, however, suggest our data are in fact broadly representative of the study region.

Borehole sites in our transect sampled multiple topographic regimes including a bedrock trough (27km-12), a bedrock ridge (27km-11), relatively flat bed areas away from troughs (33km-14 and 46km-11), and the wall of a major bedrock trough near the margin (M2-10) (Figure B-2). The boreholes also sampled a wide range of ice depths and distances inland from the margin (Table B-1). Across the range of locations sampled, borehole water pressure measurements throughout the transect show similar characteristic seasonal phases and variability within a confined range of values (Figures B-3, B-6, B-8). Further, no distinct trends in pressure as a function of distance inland or ice depth were identified. We have not, however, sampled the bottom of the very deepest bedrock trough, and the pressure regime along its main axis remains unknown.

Another concern is whether our measurements are biased by the melt conditions unique to the 2010–2015 seasons. In particular, the 2010 and 2012 melt seasons were both record warm years with large surface melt production (Nghiem et al. 2012, Tedesco et al. 2013, van As et al. 2012). Nevertheless, our results include three melt seasons with conditions more similar to the 20-year mean surface mass balance measurements of the K-transect, which passes near our transect of boreholes and likely reflects similar conditions (van de Wal et al. 2012). Further, our pressure records (including four boreholes with measurements spanning consecutive melt seasons during 2011–2012 and 2012–2013) show no systematic difference between water pressures measured in the high melt years and the average melt years (Figure B-8). Although our measurements are influenced by conditions unique to each season, the 5-year total span of the dataset is likely broadly representative of multi-year conditions.

Measurements of borehole water pressure at other locations across western GrIS also show similar results to those presented here (Table B-2). Van de Wal et al. (2015) report melt season water pressure from two boreholes (spaced 5 m apart) located approximately 15 km inland and 2 km south of our transect, ranging approximately 0.93–1.0 OB. Andrews et al. (2014) and Ryser et al. (2014a, b) report pressure for two melt seasons and two winters (2011–2012) from six boreholes located 20–30 km inland and 250 km northwest of our transect (~600–700 m depth). These records range approximately 0.90–1.13 OB, showing similar seasonal phases, and similar differences in magnitude and variability of pressure between closely spaced boreholes (30–40 m). Lüthi et al. (2002) measured water pressure for two months in two deep boreholes (830 m) spaced ~20 m apart, with weak diurnal cycles and pressure remaining steady near 1.0 OB. Earlier measurements (Iken et al. 1993, Thomsen and Olesen 1990, 1991, Thomsen et al. 1991), although only hours to days in duration, also agree with the observations reported here.

Table B-2. Summary data for all previous borehole water pressure measurements on the GrIS.

Study	Pressure range (fraction of OB)	Number of boreholes[a]	Distance inland (km)[b]	Ice depth (m)
This study, 12-borehole suite	0.76–1.17	13	0.5–46	146–821
van de Wal et al. (2015)	0.93–1.00	2	15	not reported
Andrews et al. (2014); Ryser et al. (2014a, b)	0.90–1.13	6	20–30	620–700
Lüthi et al. (2002)	1.00–1.01	2	55	830
Iken et al. (1993)	0.96–1.00	2	50	1600
Thomsen and Olesen (1990, 1991); Thomsen et al. (1991)	0.79–1.05	12	1–8	180–350

[a] Number of boreholes with published water pressure records.

[b] Distance inland is from the terminus of Issunguata Sermia (this study, exception to near-margin holes), or from the terminus of Jakobshavn Isbræ terminus (Iken et al. 1993, Lüthi et al. 2002). All other distances are approximate from the ice margin.

An important exception to the consistency of water pressures is the record from our near-margin borehole M1-10. These data clearly represent a separate hydraulic regime that is an outlier in our dataset (Figures B-8, B-9) and the observations of other workers. This borehole is likely not representative of overall ablation zone conditions as a result of the site location and shallow ice depth. The site is located only 450 m from the lateral ice sheet margin where subglacial conditions are likely well-channelised and tunnels emerge at atmospheric pressure. The relatively thin ice (<100 m) limits creep closure rates, allowing increased conduit cross-sectional area and lower diurnal water pressures (Röthlisberger 1972). The large diurnal range in pressure at this site is similar to water pressure measured in mountain glacier settings (e.g. Fudge et al. 2008).

To summarise, the consistency we find between multiple topographic regimes and years of measurement, as well as with all previous borehole pressure measurements for the GrIS, implies that our limited point measurements are likely broadly representative of regional conditions. With exception to our shallowest near-margin borehole, water pressures throughout the transect are confined within a distinct range of relatively high pressures (approximately 0.8–1.1 OB), and show consistent seasonal phases and a period of regular diurnal cycles. However, our results also show that within the limits of confinement, substantial local variability can be present that may not necessarily be individually upscaled to represent regional conditions.

B6.2 Implications for hydraulic potential gradient

Temporal variability

Our data identify winter water pressures that are relatively steady, suggesting that the limited basal flow during this period is probably constrained by a relatively constant $\nabla\phi_h$ field. Particularly relevant is that the summer pressure field averaged over the daily melt cycle also shows only minor difference from winter pressures (Figure B-8). Hence, over a long time average, the hydraulic potential gradient is essentially static. At shorter diurnal time scales, however, observed fluctuations in pressure have the capacity to induce substantial variations in the potential gradient field. This follows from the fact that pressures across the transect reside near overburden levels, so even small fluctuations influence the relative importance of bedrock and surface topography on the $\nabla\phi_h$ field (Figure B-1).

To illustrate a plausible impact on $\nabla\phi_h$ due to diurnal swings in the basal pressure field, we consider a semi-empirical conceptual model assuming potential gradients determined solely by the ice overburden as in Equation (B-4). We use surface and bed topography to perform two separate calculations of $\nabla\phi_h$ following Equation (B-4) for imposed values of daily minimum and maximum water pressure that are guided by our observations (see Supporting Information for details). Comparison of the two $\nabla\phi_h$ fields shows that large changes in both vector magnitude and direction are possible in response to only modest pressure variations (Figure B-10). In response to a pressure decline from 0.99 to 0.87 OB, vector magnitude increases over three quarters of the study area, with ~10 % of the area demonstrating changes of 2–3 fold (Figure B-10). Effects are greatest where bed slopes are steepest and corresponding surface slopes are nearly flat. Vector rotation over the diurnal cycle is controlled by the disparity between surface and bed slope aspects. This is commonly associated with the walls of deep bedrock troughs, which generally have an aspect that is normal to surface slope aspect. This analysis thus demonstrates that despite the relatively static $\nabla\phi_h$ when averaged over long time scales, basal water flow could be highly dynamic in response to the pressure changes that occur over shorter times scales during the melt season.

Spatial variability

Gradients in the hydraulic potential can arise from water pressure changes due to ice thickness variability, and from water pressure changes stemming from basal drainage system processes (Equation B-3). Our data reveal that both of the water pressure terms in Equation (B-3) make important contributions to the overall hydraulic potential and gradients therein. Yet, while basal processes modify the local overburden pressure, we also find that such modifications are not unlimited but fall within a restricted range. With the exception of locations very close to the margin, all time/space variability occurs within a fixed range of ~0.8 to 1.1 OB. As a result, at increasing spatial scales across the ice sheet, hydraulic potential change from ice thickness variation becomes larger than that from water pressure adjustments associated with basal processes. Hence, our transect of basal water pressure measurements implies that the far field $\nabla\phi_h$ mimics changes in ice thickness, but has superimposed local gradients from basal processes (Figure B-11). This suggests the validity of Equation (B-4) is strongly dependent on the spatial scale and the processes of interest.

Water pressure gradients within the drainage system are determined by the distance along flow pathways rather than straight line connections between two geographic locations (or DEM cells). The very conceptualisation of $\nabla\phi_h$ is therefore complicated by whether water pressure changes are defined in terms of a discretized topographic domain or along continuous elements of the basal drainage system. This is illustrated by the local gradients we calculate, which reach 20 kPa m^{-1}.

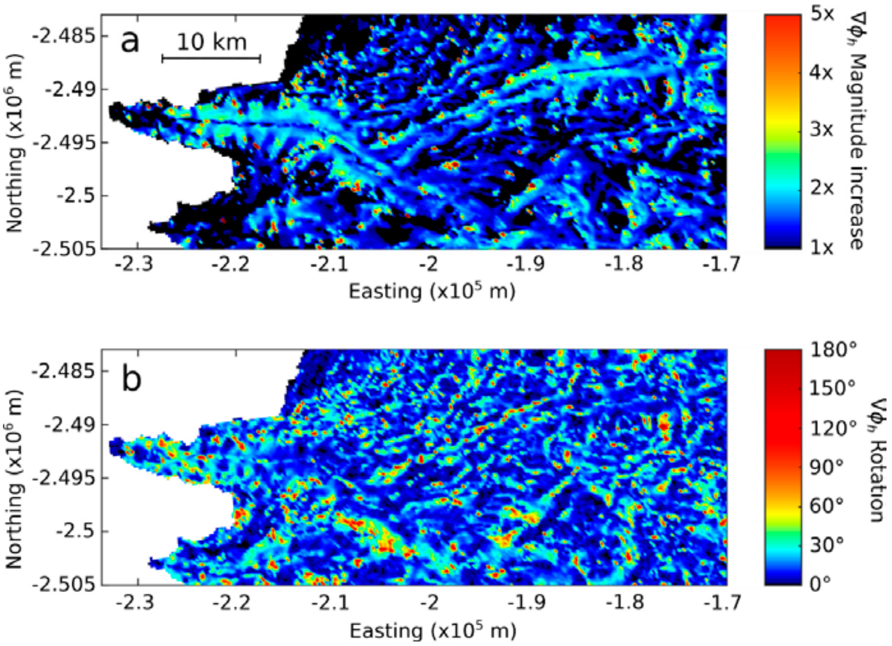

Figure B-10. *Calculated change in magnitude (Panel a) and rotation (Panel b) of hydraulic potential gradient vectors over a diurnal cycle, using the imposed range of basal water pressure shown by the shaded region in Figure B-9 (0.87 OB to 0.99 OB). Black areas in Panel (a) indicate a decrease in gradient magnitude (factor <1×).*

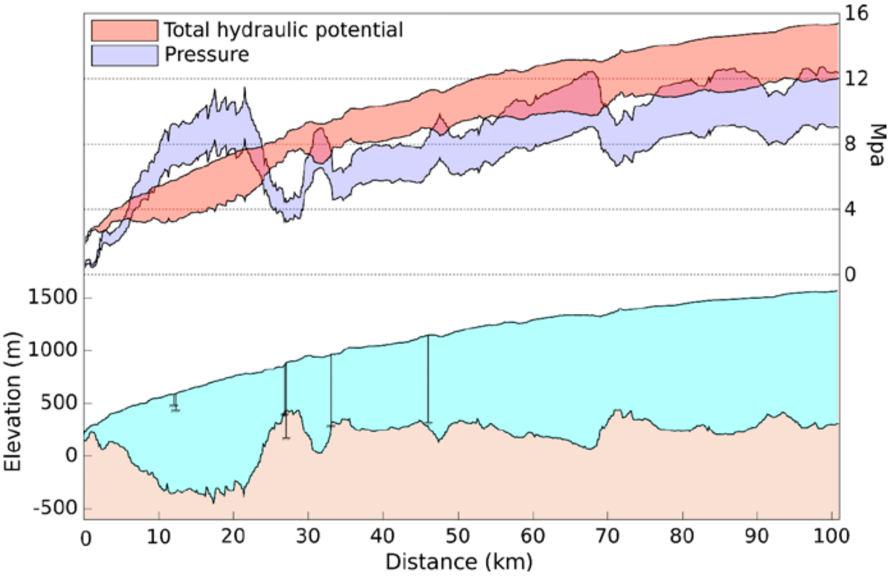

Figure B-11. *Basal water pressure and total hydraulic potential along the transect line shown in Figure B-2 extending to 100 km inland. Ice surface and bed topography along the profile are shown for context and borehole locations and depths have been projected into the plane of the profile. The shaded bands for both pressure and total hydraulic potential define along-glacier gradients (diminishing from right-to-left) where the range in values are derived from measured borehole water pressures, ranging 0.8–1.1 of OB. The shaded bands reflect changes in ice thickness and bed elevation combined with variable water pressure stemming from basal processes.*

Because the calculation is made using a straight line assumption with no knowledge of flowpath characteristics, our computed gradients should be viewed as a maximum. Robust and precise calculation of $\nabla\phi_h$ with inclusion of drainage system pressure gradients thus awaits a fuller understanding of the geometry and dynamics of the basal flow system.

Prior studies of hydraulic potential gradients in Western Greenland (e.g. Chu et al. 2016, Lewis and Smith 2009, Lindbäck et al. 2015, Tedstone et al. 2014) including our own analysis in Section 5.2.1, have neglected drainage system pressure gradients and flow paths; they are based solely on changes in ice thickness across a cellular topographic domain. Our in situ measurements of basal conditions heed caution to this approach. Despite our finding that far-field $\nabla\phi_h$ follows ice thickness changes, the degree to which our measured local basal process-driven pressure gradients facilitate or hinder broader drainage system reorganisation remains uncertain. Thus, specific channel systems, drainage basin areas, and processes related to basin piracy (e.g. Chu et al. 2016, Lindbäck et al. 2015) may not necessarily be captured by water pressure that is a spatially invariant fraction of overburden computed on a cellular topographic domain.

B7 Conclusions

Thirteen borehole water pressure records collected across a 46 km transect of the Western Greenland Ice Sheet show that basal water pressure undergoes characteristic seasonal phases and is confined within a limited range. Water pressures are relatively steady and high during winter, variable and irregular during spring and fall, and have diurnal cycles that can persist for multiple weeks during the peak melt season. Only a single borehole located 450 m from the ice sheet margin with ice depth <100 m shows relatively low water pressure, ranging between 0.3 to 1.05 of overburden (OB) during the melt season. This record likely represents a channelised hydraulic regime with highly variable meltwater flux and limited creep closure near the ice edge. The remaining twelve boreholes show pressures varying within a confined range, with minimum pressure predominantly greater than 0.8 OB and maximum pressure near or just above overburden. Despite diurnal pressure changes during the summer period, melt season median pressure varies by less than 0.02 OB from winter median pressure for four of five boreholes with overwinter records.

The basal water pressure across the high relief bed of our Western Greenland study area experiences gradients stemming from two sources: changes in ice thickness determining the overburden pressure, and changes arising from basal processes. Because water pressure varies within a relatively restricted fraction of overburden, the hydraulic potential gradient most closely mimics the ice thickness when considered over larger spatial scales and time steps that average diurnal swings in pressure. However, on sub daily time scales during the melt season, cycling of pressure can lead to substantial changes in the direction and magnitude of the hydraulic potential gradient. Furthermore, over length scales where the ice thickness does not change substantially, the hydraulic potential is strongly influenced by large gradients resulting from basal drainage system processes.

B8 Acknowledgments

This work is funded by SKB, Posiva, NWMO, and NAGRA, the U.S. National Science Foundation (PP-ANS grants #0909495/#1203451), and NASA (grant #NNX11AM12A). The authors thank editor Bryn Hubbard and reviewers Martin Lüthi and Peter Jansson for comments that greatly improved the manuscript. Many thanks to the graduate and undergraduate students from University of Montana and University of Wyoming who assisted in field work. Data sets are published by the Swedish Nuclear Waste Management Company referenced by the Greenland Analogue Project at the following web address: http://www.skb.com/publications/.

B9 References

Andrews L C, Catania G A, Hoffman M J, Gulley J D, Lüthi M P, Ryser C, Hawley R L, Neumann T A, 2014. Direct observations of evolving subglacial drainage beneath the Greenland ice sheet. Nature 514, 80–83.

Bamber J L, Griggs J A, Hurkmans R T W L, Dowdeswell J A, Gogineni S P, Howat I, Mouginot J, Paden J, Palmer S, Rignot E, Steinhage D, 2013. A new bed elevation dataset for Greenland. The Cryosphere 7, 499–510.

Catania G A, Neumann T A, 2010. Persistent englacial drainage features in the Greenland Ice Sheet. Geophysical Research Letters 37, 1–5. doi:10.1029/2009GL041108

Chandler D M, Wadham J L, Lis G P, Cowton T, Sole A, Bartholomew I, Telling J, Nienow P, Bagshaw E B, Mair D, Vinen S, Hubbard A, 2013. Evolution of the subglacial drainage system beneath the Greenland Ice Sheet revealed by tracers. Nature Geoscience 6, 195–198.

Chu W, Creyts T T, Bell R E, 2016. Rerouting of Subglacial Water Flow between Neighboring Glaciers in West Greenland. Journal of Geophysical Research: Earth Surface 121, 925–938.

Cuffey K M, Patterson W S B, 2010. The physics of glaciers. 4th ed. Oxford: Elsevier.

Das S B, Joughin I, Behn M D, Howat I M, King M a, Lizarralde D, Bhatia M P, 2008. Fracture propagation to the base of the Greenland Ice Sheet during supraglacial lake drainage. Science 320, 778–781.

Fountain A G, Walder J S, 1998. Water flow through temperate glaciers. Reviews of Geophysics 36, 299–328.

Fudge T J, Humphrey N F, Harper J T, Pfeffer W T, 2008. Diurnal fluctuations in borehole water levels: configuration of the drainage system beneath Bench Glacier, Alaska, USA. Journal of Glaciology 54, 297–306.

Harrington J A, Humphrey N F, Harper J T, 2015. Temperature distribution and thermal anomalies along a flowline of the Greenland ice sheet. Annals of Glaciology 56, 98–104.

Hewitt I J, 2013. Seasonal changes in ice sheet motion due to melt water lubrication. Earth and Planetary Science Letters 371–372, 16–25.

Hewitt I J, Schoof C, Werder M A, 2012. Flotation and free surface flow in a model for subglacial drainage. Part 2. Channel flow. Journal of Fluid Mechanics 702, 157–187.

Hoffman M J, Catania G A, Neumann T A, Andrews L C, Rumrill J A, 2011. Links between acceleration, melting, and supraglacial lake drainage of the western Greenland ice sheet. Journal of Geophysical Research, 116, F04035. doi:10.1029/2010JF001934

Hooke R L, 1989. Englacial and subglacial hydrology: a qualitative review. Arctic and Alpine Research 21, 221–233.

Hubbard B, Nienow P, 1998. Alpine subglacial hydrology. Quaternary Science Reviews 16, 939–955.

Humphrey N, Echelmeyer K, 1990. Hot-water drilling and bore-hole closure in cold ice. Journal of Glaciology 36, 287–298.

Iken A, Echelmeyer K, Harrison W, Funk M, 1993. Mechanisms of fast flow in Jakobshavns Isbrae, West Greenland: Part I. Measurements of temperature and water level in deep boreholes. Journal of Glaciology 39, 15–25.

Lewis S M, Smith L C, 2009. Hydrologic drainage of the Greenland Ice Sheet. Hydrological Processes 23, 2004–2011.

Lindbäck K, Pettersson R, Doyle S H, Helanow C, Jansson P, Kristensen S S, Stenseng L, Forsberg R, Hubbard A L, 2014. High-resolution ice thickness and bed topography of a land-terminating section of the Greenland ice sheet. Earth System Science Data 6, 331–338.

Lindbäck K, Pettersson R, Hubbard A L, Doyle S H, van As D, Mikkelsen A B, Fitzpatrick A A, 2015. Subglacial water drainage, storage, and piracy beneath the Greenland ice sheet. Geophysical Research Letters, 42(18), 7606–7614.

Liston G E, Mernild S H, 2012. Greenland freshwater runoff. Part I: A runoff routing model for glaciated and nonglaciated landscapes (HydroFlow). Journal of Climate 25, 5997–6014.

Livingstone S J, Clark C D, Woodward J, Kingslake J, 2013. Potential subglacial lake locations and meltwater drainage pathways beneath the Antarctic and Greenland ice sheets. The Cryosphere 7, 1721–1740.

Lüthi M, Funk M, Iken A, Gogineni S, Truffer M, 2002. Mechanisms of fast flow in Jakobshavn Isbrae , West Greenland : Part III . Measurements of ice deformation , temperature and cross-borehole conductivity in boreholes to the bedrock. Journal of Glaciology 48, 369–385.

McGrath D, Colgan W, Steffen K, Lauffenburger P, Balog J, 2011. Assessing the summer water budget of a moulin basin in the Sermeq Avannarleq ablation region, Greenland ice sheet. Journal of Glaciology 57, 954–964.

Meierbachtol T, Harper J, Humphrey N, 2013. Basal drainage system response to increasing surface melt on the Greenland Ice Sheet. Science 341, 777–779.

Morlighem M, Rignot E, Mouginot J, Seroussi H, Larour E, 2014. Deeply incised submarine glacial valleys beneath the Greenland ice sheet. Nature Geoscience 7, 418–422.

Nghiem S V, Hall D K, Mote T L, Tedesco M, Albert M R, Keegan K, Shuman C A, DiGirolamo N E, Neumann G, 2012. The extreme melt across the Greenland ice sheet in 2012. Geophysical Research Letters 39, 6–11. doi:10.1029/2012GL053611

Röthlisberger H, 1972. Water pressure in intra- and subglacial channels. Journal of Glaciology 11, 177–203.

Ryser C, Lüthi M P, Andrews L C, Catania G A, Funk M, Hawley R, Hoffman M, Neumann T A, 2014a. Caterpillar-like ice motion in the ablation zone of the Greenland ice sheet. Journal of Geophysical Research: Earth Surface 119, 2258–2271.

Ryser C, Lüthi M P, Andrews L C, Hoffman M J, Catania G A, Hawley R L, Neumann T A, Kristensen S S, 2014b. Sustained high basal motion of the Greenland ice sheet revealed by borehole deformation. Journal of Glaciology 60, 647–660.

Shreve R, 1972. Movement of water in glaciers. Journal of Glaciology 11, 205–214.

Tedesco M, Fettweis X, Mote T, Wahr J, Alexander P, Box J E, Wouters B, 2013. Evidence and analysis of 2012 Greenland records from spaceborne observations, a regional climate model and reanalysis data. The Cryosphere 7, 615–630.

Tedstone A J, Nienow P W, Gourmelen N, Sole A J, 2014. Greenland ice sheet annual motion insensitive to spatial variations in subglacial hydraulic structure. Geophysical Research Letters 41, 8910–8917.

Thomsen H H, Olesen O B, 1990. Continued glaciological investigations with respect to hydropower and ice-climate relationships at Pakitsoq, Jakobshavn, West Greenland. Rapp. Rapport Grønlands Geologiske Undersøgelse 148, 83–86.

Thomsen H H, Olesen O B, 1991. Hydraulics and hydrology on the Inland Ice. Rapport Gronlands Geologiske Undersogelse 152, 36–38.

Thomsen H H, Olesen O B, Braithwaite R J, Bøggild C E, 1991. Ice drilling and mass balance at Pakitsoq, Jakobshavn, central West Greenland. Rapport Gronlands Geologiske Undersogelse 152, 80–84.

van As D, Hubbard A L, Hasholt B, Mikkelsen a. B, van den Broeke M R, Fausto R S, 2012. Large surface meltwater discharge from the Kangerlussuaq sector of the Greenland ice sheet during the record-warm year 2010 explained by detailed energy balance observations. The Cryosphere 6, 199–209.

van de Wal R S W, Boot W, Smeets C J P P, Snellen H, van den Broeke M R, Oerlemans J, 2012. Twenty-one years of mass balance observations along the K-transect, West Greenland. Earth System Science Data 4, 31–35.

van de Wal R S W, Smeets C J P P, Boot W, Stoffelen M, Van Kampen R, Doyle S H, Wilhelms F, Van Den Broeke M R, Reijmer C H, Oerlemans J, Hubbard A, 2015. Self-regulation of ice flow varies across the ablation area in south-west Greenland. The Cryosphere 9, 603–611.

Werder M A, Hewitt I J, Schoof C G, Flowers G E, 2013 Modeling channelized and distributed subglacial drainage in two dimensions. Journal of Geophysical Research: Earth Surface 118, 2140–2158.

B10 Supporting information

B10.1 Introduction

Section B10.2 describes statistical techniques used to generate box plots and to calculate mean annual water pressure.

Section B10.3 and Figures B-S1 to B-S2 provide details of the methodology used in the analysis of hydraulic potential gradient sensitivity to diurnal pressure variations (as shown in Figure B-10).

B10.2 Statistical techniques

Box plots were generated to summarise seasonal and diurnal water pressure datasets. For seasonal analysis, seven records encompass part or all of a single melt season, and five records include winter data, with four of these records spanning slightly more than a year (Table B-1). For borehole records spanning part or all of a single melt season, box plots represent all data contained in the record, whereas the five records with winter data have been separated into box plot pairs for characteristic winter and melt season records, respectively. This approach allows for separate analysis of melt season and winter pressures, and allows calculation of an annual weighted mean pressure that incorporates data from all boreholes.

The borehole water pressure records show non-normal distributions, thus we use dataset medians as an indicator of central tendency for the temporal scale of interest. An annual mean value is calculated by weighting the mean melt season median among all boreholes to 3.5 months (0.29 yr), and the mean winter median among five boreholes to 8.5 months (0.71 yr). This weighting scheme allows the use of all records in the dataset, using a time span of characteristic melt season data for weighting that is generally consistent among all boreholes, from approximately June 15 to October 1. To avoid over-representation of periods with high sampling rates, all boxplots and reported median values are calculated from data re-sampled to the common long-term sampling rate (5 minute or 15 minute for melt season records, and 15 minute or 30 minute for winter records).

B10.3 Potential gradient sensitivity to diurnal pressure variations

In Discussion Section B6.2 we calculate $\nabla\phi_h$ vectors using Equation (B-4) with 250-m horizontal resolution bed and surface topography (Lindbäck et al. 2014), and with an imposed high and low pressure to represent a diurnal cycle. The imposed range in pressure is derived from the largest measured range (5th to 95th percentile) represented in the twelve-borehole suite (range of 0.12 OB, measured in borehole 27km-12B). To more accurately represent the distribution of pressure measured throughout the transect, we then center the imposed range at the mean diurnal pressure median for all boreholes, resulting in an imposed diurnal range of 0.87 to 0.99 OB (shaded region in Figure B-9).

Under this scenario, gradient vectors change both their magnitude and direction as a result of the diurnal pressure changes. Depending on the slope and aspect of underlying bed topography vectors can rotate up to 180° and both increase and decrease in magnitude. To demonstrate the limits of this process we initially explore the scenario for two borehole locations, testing both the imposed range of pressure and the maximum physically possible range of pressure (Figure B-S1).

We then apply the analysis to the entire study area at 250-m resolution using the imposed pressure range (represented by angle 2 in Figure B-S1). Resulting hydraulic potential vector pairs and the corresponding potential field contours for high and low pressure conditions are demonstrated for a section along the Issunguata Sermia trough wall (Figure B-S2). The ratio in magnitude and the rotation angle between the high and low pressure vectors is then calculated for the entire study area (Figure B-10). This analysis does not represent actual water flow paths at the bed (which are complicated by local pressure and stress fields), but is intended to illustrate plausible changes in the magnitude and direction of $\nabla\phi_h$ due to diurnal pressure swings.

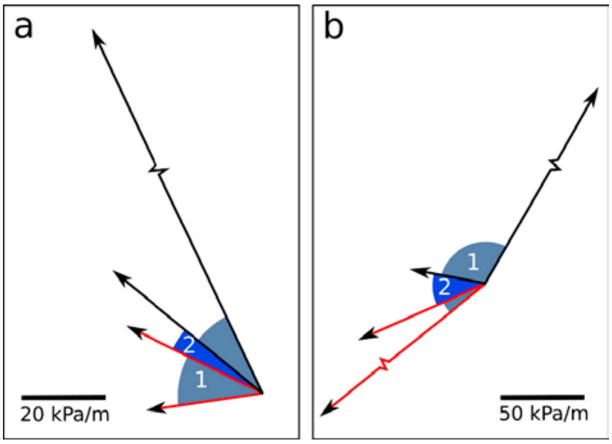

Figure B-S1. *Changes in magnitude and rotation of hydraulic potential gradient vectors resulting from the physically possible range of basal water pressure (angle 1, 0.0 OB to 1.17 OB), and for the imposed range of water pressure used for diurnal analysis (angle 2, 0.87 OB to 0.99 OB). Red vectors and black vectors correspond to high-pressure and low-pressure conditions, respectively. Panel (a) uses the bed and surface topography from site 27km-12A, representing conditions commonly found over steep sub-glacial trough walls where vector magnitudes increase with decreasing pressure. Panel (b) uses the bed and surface topography from site M2-10B, representing conditions of reverse bed slope (bed aspect opposed to surface slope aspect), resulting in a decrease in vector magnitude with decreasing pressure.*

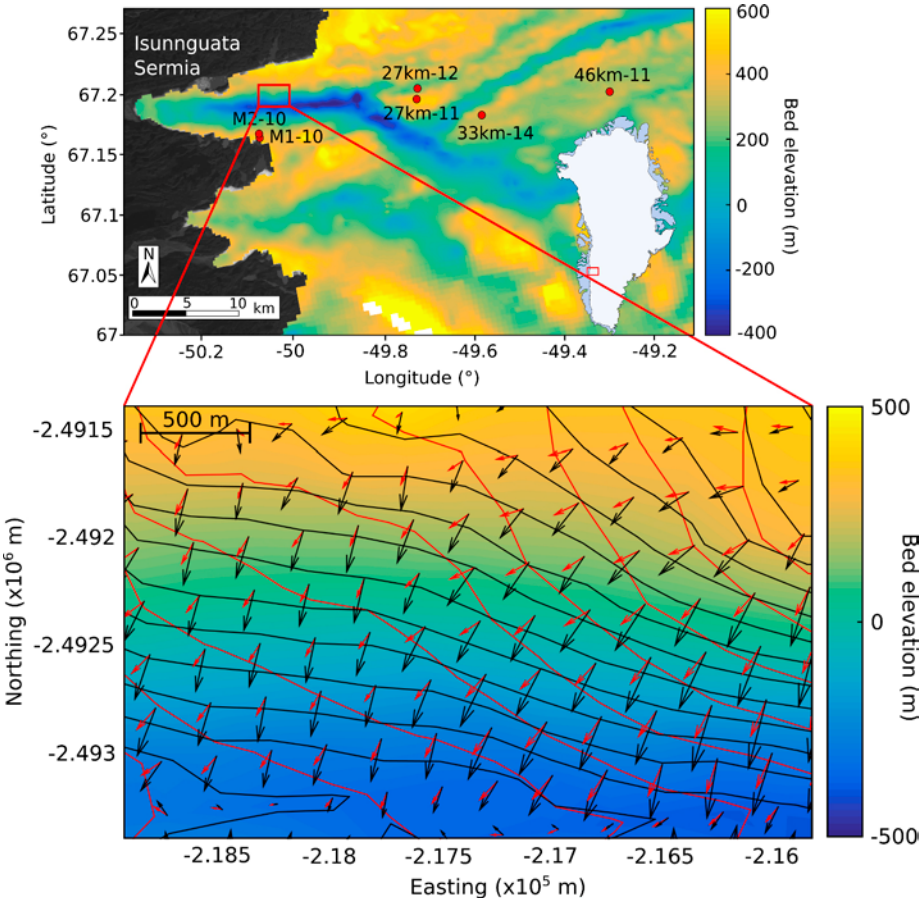

Figure B-S2. *Modification of hydraulic potential gradient magnitude and direction for a section along the Issunguata Sermia trough wall, as forced by an imposed diurnal pressure range of 0.87–0.99 OB. Base colormap is derived from 250-m resolution bed topography (Lindbäck et al. 2014). Red vectors and contours represent the hydraulic potential gradient and surface, respectively, for high pressure conditions. Black vectors and contours represent low pressure conditions. The imposed pressure range is constrained by borehole observations, as shown in Figure B-9.*

Appendix C

Short duration water pressure transients in Western Greenland’s subglacial drainage system

(**Meierbachtol T W, Harper J T, Humphrey N F, 2018.** Short duration water pressure transients in Western Greenland’s subglacial drainage system. Journal of Glaciology 64, 171–174.)

C1 Introduction

Attempts to measure short duration pressure changes in the subglacial drainage system are rare, but in all cases where pressure has been measured at high frequency, transient pressure pulse behavior has been common. Kavanaugh (2009) and Kavanaugh et al. (2010) measured thousands of subglacial pressure pulses on Trapridge and West Washmawapta glaciers that were pervasive through both winter and summer seasons, and with magnitudes exceeding the local ice overburden pressure. In other studies, pulse behavior was not directly measured, but inferred from pressure changes that were large enough to permanently deform the pressure transducer measurement diaphragm (Kavanaugh and Clarke 2000) or induce transducer failure (Kavanaugh and Clarke 2001). All existing measurements have been made beneath Canadian alpine glaciers with till beds. Frequent pulse behavior therefore appears to be a robust feature of soft-bedded glaciers, and may be a potential indicator of basal conditions (Kavanaugh et al. 2010). Furthermore, such changes in water pressure may influence glacier erosion rates by changing basal stress conditions that drive quarrying processes (Cohen et al. 2006, Hallet 1996, Iverson 1991). The relevance of short duration pressure pulses to these basal processes consequently motivates investigation of their presence and distribution on the larger Greenland Ice Sheet.

Here, we present observations of subglacial water pressure measured at high frequency in two boreholes penetrating the full ice column in Western Greenland’s ablation zone. The data provide a unique opportunity to compare the presence and magnitude of pulse behavior in the ice sheet setting to the only other available observations on small alpine glaciers, which have shown pressure pulses to be common occurrences.

C2 Methods

During the 2014 and 2015 melt seasons, nine boreholes were drilled to the ice sheet bed at a site ~34 km east of the land terminating Isunnguata Sermia outlet glacier (site 33km-14 in Wright et al. 2016; see Meierbachtol et al. 2013 for borehole drilling methods) (Figure C-1). Temperature measurements in each borehole identify temperate conditions at the bed but no measurable temperate basal layer (Hills et al. 2017). Cold ice reaching −12 °C resulted in borehole freezing within days of drilling, effectively sealing the lower borehole column from the surface.

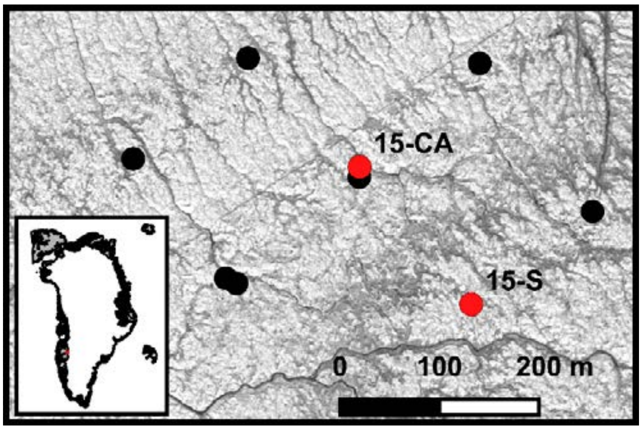

Figure C-1. *Site setting. Boreholes chosen for high frequency pressure measurements are shown in red. Background is a Worldview image from July, 2012 (Copyright 2011, DigitalGlobe, Inc.).*

Boreholes were instrumented with 2 000 psi, Omega PX309 current output pressure transducers, installed at the ice sheet bed as part of a downhole instrumentation package. In July, 2015, transducers in two boreholes (hereafter referred to as 15-S and 15-CA) were continuously powered, sampled at 4 Hz frequency, and logged to a central Campbell Scientific CR6 datalogger. Two 12V batteries, wired in series and charged by two 10W solar panels, provided power to the logger and transducer measurement system. Factory reported transducer accuracy, including repeatability, linearity and hysteresis, is 0.25 % of the full pressure span, or approximately 3.5 m. Ice depths from drilling were 678 m and 673 m at 15-S and 15-CA, respectively (borehole depth uncertainty is <1.5 %), and the holes were spaced 180 m apart (Figure C-1).

C3 Results

The pressure transducer in hole 15-S functioned for 52 days (day of year 192–244), resulting in a record composed of ~19 million measurements (Figure C-2). The 143-day record in hole 15-CA spanned July 6, 2015 to April 11, 2016 (an extended period without data is due to power loss during the winter when solar charging is absent), and contains nearly 49 million measurements (Figure C-2). Pressure persisted near or above local overburden level through the full time series in both boreholes.

The definition of a pressure 'pulse' is somewhat arbitrary, but implies a pressure deviation from and recovery to a longer term trend over a short duration. Data records from the two boreholes show low amplitude noise of ~1 m (e.g. Figure C-3b). We arbitrarily define a pulse to be five times greater than this noise level, and define 'short duration' to be less than one minute. We therefore consider pressure excursions with amplitudes of at least 5 m, and which return to the long term trend within one minute, to be pulses. Four pressure pulses are measured in hole 15-CA which meet our pulse criteria (an additional one on day-of-year 190 results from drainage of a nearby borehole during drilling and does not reflect a natural perturbation to the basal system) (Figure C-2, Table C-1). One pulse event is measured in 15-S (Figure C-2, Table C-1). A sharp increase in pressure is also observed on day of year 229 but subsequently decays over more than eight hours.

All measured pulses occur as pressure drops with amplitudes ranging from 9.6 m to more than 73 m, equivalent to pressure changes of 0.09–0.72 MPa (Table C-1). Diurnal pressure variations in the boreholes are no greater than 5–7 m during the melt season; the pressure events can therefore be an order of magnitude larger than measured daily pressure variability.

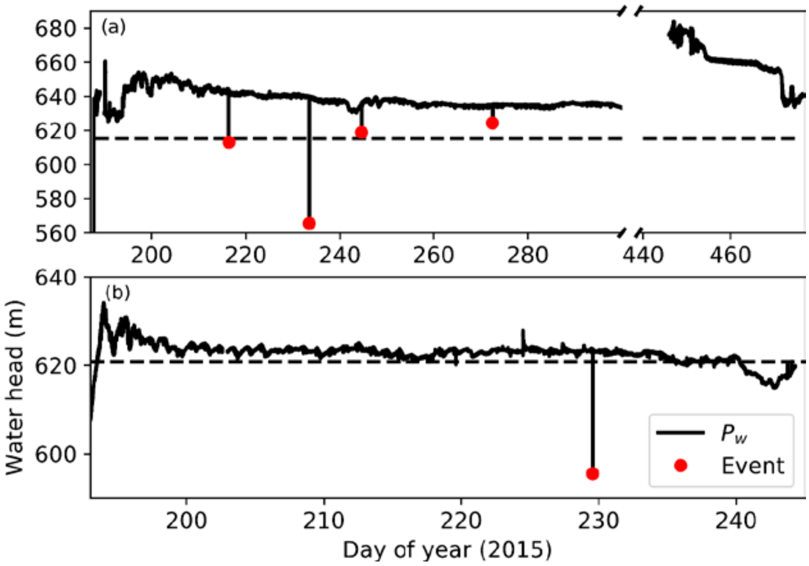

Figure C-2. *Pressure record from boreholes GL15-CA (a), and GL15-S (b) with identified pressure events (red dots). Broken axes in (a) obscure the winter period for which there is no data. Horizontal dashed line is the local overburden pressure, assuming an ice density of 917 kg m*$^{-3}$*. Note the different time and pressure scales in each panel.*

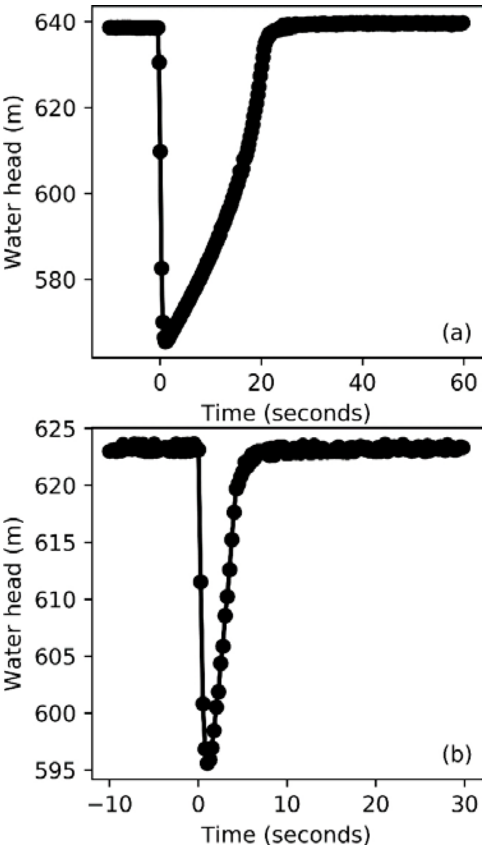

Figure C-3. Pressure pulse examples from GL15-CA (a) and GL15-S (b), measured on days of year 233 and 229 respectively. X-axes are approximate time from the start of the pressure change.

Table C-1. Pressure pulse statistics for the five events measured in holes GL15-CA and GL15-S. Pulse magnitude as a percentage of overburden ice pressure (% OB) is computed assuming an ice density of 917 kg m^{-3}.

Hole			Time to Peak	Recovery Time	Amplitude		
	Pulse Number	Day of Year	(s)	(s)	(m)	(% OB)	(MPa)
GL15-CA	1	216	1.	11.	−29.8	4.8	0.29
	2	233	1.5	26.	−73.3	11.9	0.72
	3	244	1.25	11.	−16.1	2.6	0.16
	4	272	1.	9.	−9.2	1.5	0.09
GL15-S	5	229	1.	7.	−27.7	4.5	0.27

The shape of pressure events is asymmetric; pressure falls in 1.5 s or less, and recovery is many seconds to tens of seconds (e.g. Figure C-3). While the sample size is small, there is no clear relationship between the magnitude of pressure decline and recovery time. The largest documented event also displays the longest recovery (26 seconds), but a pressure drop of 27.7 m recovers in 7 seconds, while a smaller pulse of magnitude 16.1 m recovers in 11 seconds. None of the pulse events are transmitted between boreholes.

C4 Discussion

During a 231 day interval on Trapridge Glacier, Kavanaugh (2009) measured 1 467 pressure pulses in one borehole with magnitudes greater than 4.7 m; 70 of these had magnitudes greater than the local ice overburden pressure of 47.2 m. On West Washmawapta Glacier, a total of 199 260 pulses were measured in a single borehole with magnitudes >0.5 m over a 290 day period (Kavanaugh et al. 2010). Visual inspection shows that more than 1 000 of these pulses had magnitudes >5 m (see

Kavanaugh et al. 2010, Figure 8c). The large numbers of pulses measured in the two studies that have focused on transient pressure variations may suggest that such pulse behavior is a characteristic feature of the basal drainage system. Common pressure sampling intervals of multiple minutes or more in Greenland borehole studies (e.g. Andrews et al. 2014, Wright et al. 2016) could alias these variations, therefore failing to capture details of the system with implications for basal processes.

Our measurements in Western Greenland do not record such ubiquitous pressure pulse behavior, confirming that frequent, rapid fluctuations in pressure are not universal occurrences at the bed. However, brief pressure deviations are not wholly absent from our time series' either. Furthermore, our observations show that the magnitude of pulse events can be large.

C4.1 Pressure pulse causality

Pulse behavior could arise from a multitude of processes, and there is no a priori reason to believe that events in a given record must be generated by just one mechanism. The primary aim of this manuscript is to report their presence on the GrIS; detailing the exact mechanism(s) generating pulse behavior is an unconstrained exercise. Nevertheless, their presence compels us to briefly explore potential processes, and our data allow some bounding constraints.

Importantly, none of the measured pulses are transmitted between two boreholes 180 m apart. This result demonstrates that measured pressure pulses are localised events occurring over length scales much less than an ice thickness, in contrast to widespread pressure waves that have been observed elsewhere and interpreted to reflect failure of a spatially extensive sticky spot (c.f. Kavanaugh and Clarke 2001).

The cause of local pressure events may depend on whether the immediate drainage system to which the boreholes are connected is open or closed. If the system is open, and drainage elements are transmitting water, pressure pulses could result from brief decreases in water flux. A change in water input from the surface is an unlikely cause, even in the situation of stream capture, because the events are so brief and spatially limited. A more likely scenario might be a nearly instantaneous change in hydraulic connection at the bed. We would expect temporary blockage of a water-transmitting orifice from loose sediment to yield a pressure curve that slowly declines as the orifice is blocked and rapidly recovers as the blockage is flushed. This conceptualised asymmetry is opposite of the measured pulse curves. Alternatively, pressure disturbances could be caused by connection to an adjacent cavity at lower pressure. In this scenario the asymmetric pulse curve would reflect establishment of a hydrologic connection that occurred much more quickly than the subsequent pressure equilibration from water flow.

If the local system is closed, then it is possible to generate pulses through small volume changes in water cavity volume at the bed (Kavanaugh 2009, Kavanaugh et al. 2010). Explaining the pressure drops we measure through volume change requires an expansion of $\sim 10^{-2}$ %. The consistently high pressures we measure satisfy a critical requirement for basal crevassing (van der Veen 1998), but appealing to basal crevasses as a volume expansion mechanism is only reasonable if the crevasse volume is an extremely small fraction of the isolated drainage system. Direct observations in a different borehole at the site identified isolated cavity volumes on the order of 1–7 m^3 (Meierbachtol et al. 2016). If we assume that this volume is characteristic of cavities at the site, then expansion by basal crevassing requires that fractures are much smaller than those previously observed on smaller alpine glaciers (e.g. Harper et al. 2010).

Rather than expanding the drainage system by generating new void space from basal crevasses, small volume expansion could occur from mechanical forcing through brief stress transients in the ice. Kavanaugh (2009) and Kavanaugh et al. (2010) interpreted the frequently observed pulses on Trapridge and West Washmawapta glaciers to reflect these stress transients, generated by episodic failure along the ice-bed interface. Both of these glaciers are underlain by soft sediment, implying that failure was controlled by coulomb-plastic behavior of the subglacial till. In contrast, drilling tests and borehole experiments at our site indicate predominantly hard bed conditions, with perhaps a thin and discontinuous mantle of sediment (Harper et al. 2017). There is no reason why stick-slip motion should not occur beneath hard-bedded glaciers as well (e.g. Cohen et al. 2005, Hubbard 2002). However, if slip-induced stress transients are the cause of observed pulses, this implies that local stick-slip behavior at the bed is rare, supporting Kavanaugh's (2009) assertion that frequent pulse behavior may be characteristic of soft-bedded glaciers and can be revealing of bed conditions.

C4.2 Implications for erosion processes

Regardless of their cause, considering that our data support a hard bedded setting at our study site, then even the infrequent occurrence of pressure pulses may still have implications for bedrock quarrying processes. By controlling local basal water pressure beneath Engabreen, Norway through pumping experiments, Cohen et al. (2006) showed that acoustic emissions associated with a known preexisting fracture in a bedrock step increased in response to reductions in basal water pressure on the step's lee side. These results indicated that water pressure fluctuations promoted quarrying by causing stress requirements for bedrock fracture to be exceeded.

Cohen's findings supported earlier work by Iverson (1991) and Hallet (1996), who investigated the role of water pressure fluctuations in quarrying processes from modeling perspectives. Through finite element modeling of the stress state in a bedrock step with a water cavity in its lee side, Iverson (1991) showed that a pressure reduction in the cavity removed back-stress on the bedrock lee face, and increased the normal ice pressure on the bedrock just upstream. This generated deviatoric stresses within the bedrock that were sufficient to overcome fracture criteria in preexisting bedrock cracks.

Hallet (1996) reached a similar conclusion using an analytical model based on the spatially averaged stress state of bedrock in contact with ice over a bedrock ledge. His results showed that the stress concentration in bedrock arising from the difference between ice normal pressure on the bedrock ledge and water pressure in its lee side cavity was sufficient to propagate bedrock fractures.

Model set-up in Iverson's (1991) simulations was guided by field observations, and illustrated that conditions for bedrock fracture were reached when cavity pressure was reduced by 0.6 MPa. More generally, Hallet (1996) indicated that a cavity water pressure reduction of 1 MPa could induce a deviatoric stress of nearly 10 MPa when basal water coverage is extensive. These values bound the largest pressure head drop we measure, at 0.72 MPa. The exact conditions required to exceed the bedrock fracture threshold are of course unknown and depend on local conditions, such as water coverage along the bed. Nevertheless, combined with the observation that pulses are spatially discrete, the magnitude of pressure pulses we measure at the bed illustrate that it is plausible for such pressure transients to generate deviatoric stress conditions that are favorable to bedrock fracture propagation.

Crack growth rates in bedrock are a highly non-linear function of the stress state in the bedrock (Hallet 1996). Hence, even rare water pressure deviations at the bed can influence long term bedrock fracture rates, particularly when such deviations are large.

As example, Hallet (1996) found that for a given time period, long term crack growth rates can be doubled when background tensile stresses in bedrock are perturbed by 25 % for a small fractional duration (10^{-4}). Extension of this result to our observations suggests that, despite their rare occurrence and short duration, the pressure transients we measure could enhance long term fracture propagation rates.

Large pressure diurnals are commonly associated with active regions of the basal drainage system (e.g. Hubbard et al. 1995, Murray and Clarke 1995). The presence of measured pulses over areas of the bed that are not prone to large diurnal pressure fluctuations suggests that pressure variations can occur in passive regions as well, indicating that significant pressure changes at the bed can be spatially widespread. Over time, the accumulated damage facilitated by pulse behavior could therefore provide a mechanism to enhance basal erosion over Greenland's ablation zone; a region where basal erosion rates have recently been estimated to be orders of magnitude greater than previously thought (Cowton et al. 2012).

C5 Acknowledgments

Insightful reviews by P. Moore and J. Kavanaugh improved the clarity and content of this paper. This work is funded by SKB, Nagra, Posiva, NWMO, and the U.S. National Science Foundation (PP-ANS grants 0909495/1203451). Pressure data are available upon request to the authors.

C6 References

Andrews L C, Catania G A, Hoffman M J, Gulley J D, Lüthi M P, Ryser C, Hawley R L, Neumann T A, 2014. Direct observations of evolving subglacial drainage beneath the Greenland ice sheet. Nature 514, 80–83.

Cohen D, Iverson N R, Hooyer T S, Fischer U H, Jackson M, Moore P L, 2005. Debris-bed friction of hard-bedded glaciers. Journal of Geophysical Research: Earth Surface 110, F02007. doi:10.1029/2004JF000228

Cohen D, Hooyer T S, Iverson N R, Thomason J F, Jackson M, 2006. Role of transient water pressure in quarrying: A subglacial experiment using acoustic emissions. Journal of Geophysical Research: Earth Surface 111, F03006. doi:10.1029/2005JF000439

Cowton T, Nienow P, Bartholomew I, Sole A, Mair D, 2012. Rapid erosion beneath the Greenland ice sheet. Geology 40, 343–346.

Hallet B, 1996. Glacial quarrying: a simple theoretical model. Annals of Glaciology 22, 1–8.

Harper J T, Bradford J H, Humphrey N F, Meierbachtol T W, 2010. Vertical extension of the subglacial drainage system into basal crevasses. Nature 467, 579–582.

Harper J T, Humphrey N F, Meierbachtol T W, Graly J A, Fischer U H, 2017. Borehole measurements indicate hard bed conditions, Kangerlussuaq sector, western Greenland ice sheet. Journal of Geophysical Research: Earth Surface122, 1605–1618.

Hills B H, Harper J T, Humphrey N F, Meierbachtol T W, 2017. Measured horizontal temperature gradients constrain heat transfer mechanisms in Greenland ice. Geophysical Research Letters 44, 9778–9785.

Hubbard B, 2002. Direct measurement of basal motion at a hard-bedded, temperate glacier: Glacier de Tsanfleuron, Switzerland. Journal of Glaciology 48, 1–8.

Hubbard B P, Sharp M J, Willis I C, Nielsen M K, Smart C C, 1995. Borehole water-level variations and the structure of the subglacial hydrological system of Haut Glacier d'Arolla, Valais, Switzerland. Journal of Glaciology 41, 572–583.

Iverson N R, 1991. Potential effects of subglacial water-pressure fluctuations on quarrying. Journal of Glaciology 37, 27–36.

Kavanaugh J L, 2009. Exploring glacier dynamics with subglacial water pressure pulses: Evidence for self-organized criticality? Journal of Geophysical Research: Earth Surface 114, F01021. doi:10.1029/2008JF001036

Kavanaugh J L, Clarke G K C, 2000. Evidence for extreme pressure pulses in the subglacial water system. Journal of Glaciology 46, 206–212.

Kavanaugh J L, Clarke G K C, 2001. Abrupt glacier motion and reorganization of basal shear stress following the establishment of a connected drainage system. Journal of Glaciology 47, 472–480.

Kavanaugh J L, Moore P L, Dow C F, Sanders J W, 2010. Using pressure pulse seismology to examine basal criticality and the influence of sticky spots on glacial flow. Journal of Geophysical Research 115, F04025. doi:10.1029/2010JF001666

Meierbachtol T, Harper J, Humphrey N, 2013. Basal drainage system response to increasing surface melt on the Greenland Ice Sheet. Science 341, 777–779.

Meierbachtol T W, Harper J T, Humphrey N F, Wright P J, 2016. Mechanical forcing of water pressure in a hydraulically isolated reach beneath Western Greenland's ablation zone. Annals of Glaciology 57, 62–70.

Murray T, Clarke G K C, 1995. Black-box modeling of the subglacial water system. Journal of Geophysical Research 100, 10231–10245.

van der Veen C, 1998. Fracture mechanics approach to penetration of bottom crevasses on glaciers. Cold Regions Science and Technology 27, 213–223.

Wright P J, Harper J T, Humphrey N F, Meierbachtol T W, 2016. Measured basal water pressure variability of the western Greenland ice sheet: Implications for hydraulic potential. Journal of Geophysical Research: Earth Surface 121, 1134–1147.

Appendix D

Mechanical forcing of water pressure in a hydraulically isolated reach beneath Western Greenland's ablation zone

(**Meierbachtol T W, Harper J T, Humphrey N F, Wright P J, 2016.** Mechanical forcing of water pressure in a hydraulically isolated reach beneath Western Greenland's ablation zone. Annals of Glaciology 57, 62–70.)

D1 Abstract

A suite of surface and basal measurements during and after borehole drilling is used to perform in situ investigation of the local basal drainage system and pressure forcings in Western Greenland. Drill and borehole water temperature were monitored during borehole drilling, which was performed with dyed hot water. After drilling, borehole water pressure and basal dye concentration were measured concurrently with positions in a GPS strain diamond at the surface. Water pressure exhibited diurnal changes in anti-phase with velocity. Dye monitoring in the borehole revealed stagnant basal water for nearly two weeks. The interpretation of initial connection to an isolated basal cavity is corroborated by the thermal signature of borehole water during hot water drilling. Measurement-based estimates of cavity size are on the order of cubic meters, and analysis indicates that small changes in its volume could induce the observed pressure variations. It is found that longitudinal coupling effects are unable to force necessary volume changes at the site. Sliding-driven basal cavity opening and elastic uplift from load transfer are plausible mechanisms controlling pressure variations. Elastic uplift requires forcing from a hydraulically connected reach, which observations suggest must be relatively small and in close proximity to the isolated cavity.

D2 Introduction

Basal processes can force large changes in ice motion over short time scales. On the Greenland Ice Sheet (GrIS), observations have established a link between surface melt input and dynamical ice motion over daily to seasonal periods (Bartholomew et al. 2010, Hoffman et al. 2011, Zwally et al. 2002). This forcing on velocity by surface input is attributed to the subglacial drainage system, which modulates sliding by adjusting the balance of forces at the bed through changes in drainage system pressure distribution and water coverage. To date, efforts have focused predominantly on the evolution of active drainage elements at the ice sheet bed (i.e. those that transport meltwater along the base) which permits direct assessment of pressure changes in response to imposed surface fluxes (e.g. Hewitt 2013, Werder et al. 2013). Less attention, however, has been diverted to the isolated end-member component of the subglacial system, which may have important implications for basal water storage and traction.

Weertman (1964) and Lliboutry (1976) identified cavitation and acknowledged that cavities on the lee sides of bedrock bumps may be water-filled and isolated in nature. Iken and Truffer (1997) posited that such isolated cavities may have a modulating effect on glacier flow variability. If water pressure in the active system rises, subsequent increase in velocity would drop pressure in isolated cavities, causing them to act as 'sticky spots'. Alternatively, the persistence of isolated water bodies could promote continued sliding when pressure drops in the active system or the fraction of the bed covered by water-routing elements decreases. Over diurnal time scales, Ryser et al. (2014a) reproduced in situ deformation measurements and out-of-phase surface velocity and basal water pressure with a numerical model, and concluded that isolated, slippery reaches of the bed likely respond in a passive manner to daily changes in basal traction along a connected reach of the drainage system. Over longer scales, it has been hypothesised that the seasonal slow-down in Greenland during the melt season is the result of the incorporation of isolated basal cavities by more interconnected reaches of the ice sheet drainage network (Andrews et al. 2014).

Isolated cavities thus appear to be a relevant component in the feedback between surface melt forcing, drainage development and sliding dynamics. However, their importance is likely a function of their size and distribution, processes influencing their pressure, and proximity to water-routing elements along the ice sheet bed. These remain poorly constrained beneath all glaciers, including the GrIS. Here, we present in situ measurements of borehole water pressure, temperature, and dye concentration, and augment these with GPS positions in a strain diamond from a site in the ablation zone of western GrIS. We use these data to characterise a reach of the basal drainage network, with focus on isolated elements. From independent dye and thermal dilution considerations, we estimate local drainage network geometry. Finally, we explore plausible processes inducing the observed pressure behavior in the context of the interpreted basal drainage conditions.

D3 Site and methods

D3.1 Site setting

The experiment was conducted in western GrIS' ablation zone at a site located ~34 km east of the terrestrial terminus of Isunnguata Sermia (Figure D-1). The experimental borehole was one of nine drilled at the site which are included in an east-west transect of 32 boreholes drilled to the bed during 2010–2015 as part of a multi-faceted investigation of basal hydrology and ice dynamics in the region (Graly et al. 2014, Harrington et al. 2015, Meierbachtol et al. 2013, 2015). Ice thickness at the study site ranges from 641–675 m. Similar to other borehole sites along the transect, the ice temperature is coldest at mid-depth and has a temperate basal layer tens of meters thick (see Harrington et al. 2015). IceBridge radar data (Leuschen et al. 2010) indicate the bed is relatively flat with a slight reverse bed slope, although an east-west trending, 1 000 m deep basal trough exists about 1.8 km north of the site.

D3.2 Borehole drilling

Hot water drilling methods permitted direct access to the ice sheet bed (see Meierbachtol et al. 2013 for description). Surface melt water, temporarily housed in a 7.7 m^3 tank, was used for drilling. While radar data established the approximate depth to the bed, in the field we used drill water pressure, drill tower load, and borehole water level as indicators of contact with the ice-bed interface. The cold ice temperatures at depth caused refreezing of the borehole, allowing just 2–3 hours of working time to install instrumentation after borehole completion. Depth marks on the drilling hose and sensor cable string constrain hole depth with an uncertainty of <1 % (5 m).

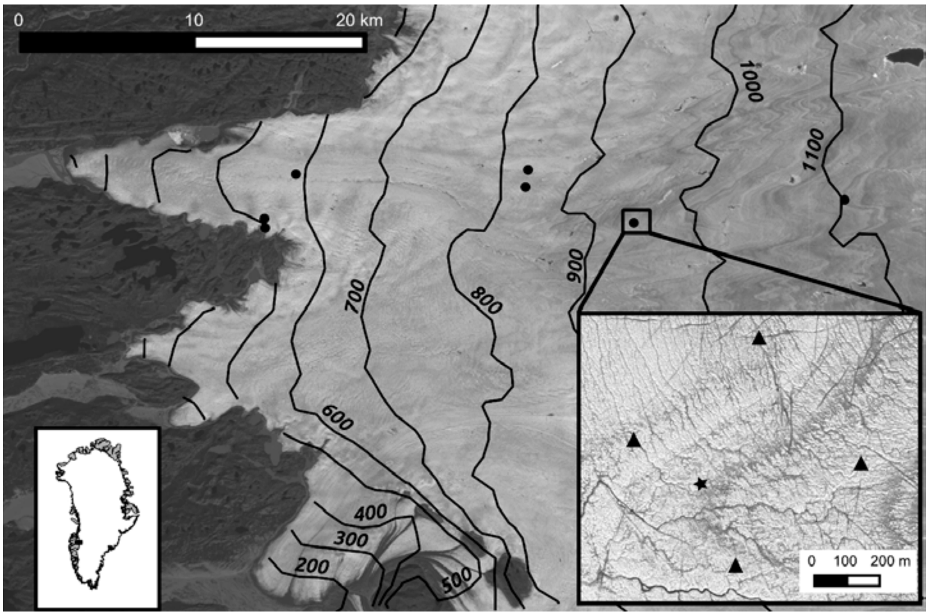

Figure D-1. Western Greenland site setting. Study site and drill sites from previous field investigations (Meierbachtol et al. 2013) are shown as black circles for reference. Surface contours are generated from the surface digital elevation model from Bamber and others (2013), overlaid on a LANDSAT 8 image from July, 2014. Detailed study area is shown in the inset image. Triangles in the inset show locations of GPS stations and star shows borehole location overlaid on a Worldview image from July, 2012 (Copyright 2011, DigitalGlobe, Inc.).

D3.3 Dye tracing

When the advancing drill was approximately 5–10 m above the expected bed depth, a known volume of 20 % Rhodamine WT (RWT) dye was added to the drilling water reservoir. Dye concentration of the drilling water was confirmed by measurement after thorough mixing. The dyed hot water was pumped through the drill until the borehole terminated at the bed, and during drill recovery from the hole, resulting in a dye profile along the entire borehole length. The final dye concentration is strongly influenced by the drilling advance/extraction rate. Rapid drill extraction rates of ~25 m min^{-1} mean small volumes of dye were added higher in the borehole column facilitating greater dilution. Further, because we held the drill steady at the bed for 20 minutes in attempts to confirm basal intersection, dye concentrations should have been highest near the bottom of the borehole, approaching the concentration in the surface storage tank.

After hole completion, we lowered a Turner Designs Cyclops 7 fluorometer down the borehole, logging RWT concentration to capture a dye profile along the borehole column. The fluorometer was then fixed in place just above the bed so that long term dye concentrations at the ice-bed interface could be logged to a surface datalogger at 5 minute intervals. To overcome signal degradation over the ~750 m cable lengths, we converted fluorometer voltage output to current. Current output was converted back to a differential voltage at the surface. Lab calibration confirmed a linear response of the modified voltage output across the 0–800 parts per billion (ppb) measurement range of the fluorometer. Our modified circuit limited the measurement precision and introduced a slight sensitivity to temperature change in the datalogger box. As a result, we estimate the accuracy of the fluorometer measurements to be ~10 ppb.

D3.4 Thermal tracing

Two temperature sensors were embedded in the drill stem to track heat transfer between the drilling water and the borehole during drill advance and extraction (Figure D-2a). One sensor was located on the inside wall of the drill stem to measure the temperature of the drilling water prior to exiting the nozzle, and another was pressed against the outside wall of the stem to measure borehole water temperature. Temperatures were logged at 1 min intervals by a data logger located in the hollow drill stem cavity. Sensor resolution is 0.065 °C.

Assessing the accuracy of temperature measurements is complicated by thermal gradients between hot water flowing through the drill and the colder water in the borehole, facilitating heat conduction through the instrumented drill stem. Comparison of the inner sensor temperature to the drill water temperature exiting the diesel heaters at the surface prior to drilling indicates that the sensor measurement is within ~3 °C of the water temperature traveling through the drill hose. The degree to which the outer sensor is affected by thermal conduction through the instrumented stem from hot drill water is difficult to constrain. In calculations below, as with the inner sensor, we assume the outer sensor is biased by 3 °C from true borehole water temperature, and estimate an uncertainty of +/− 3 °C in error calculations. In doing so, we inherently assume that the measured drill water and borehole water temperatures are minima and maxima, respectively.

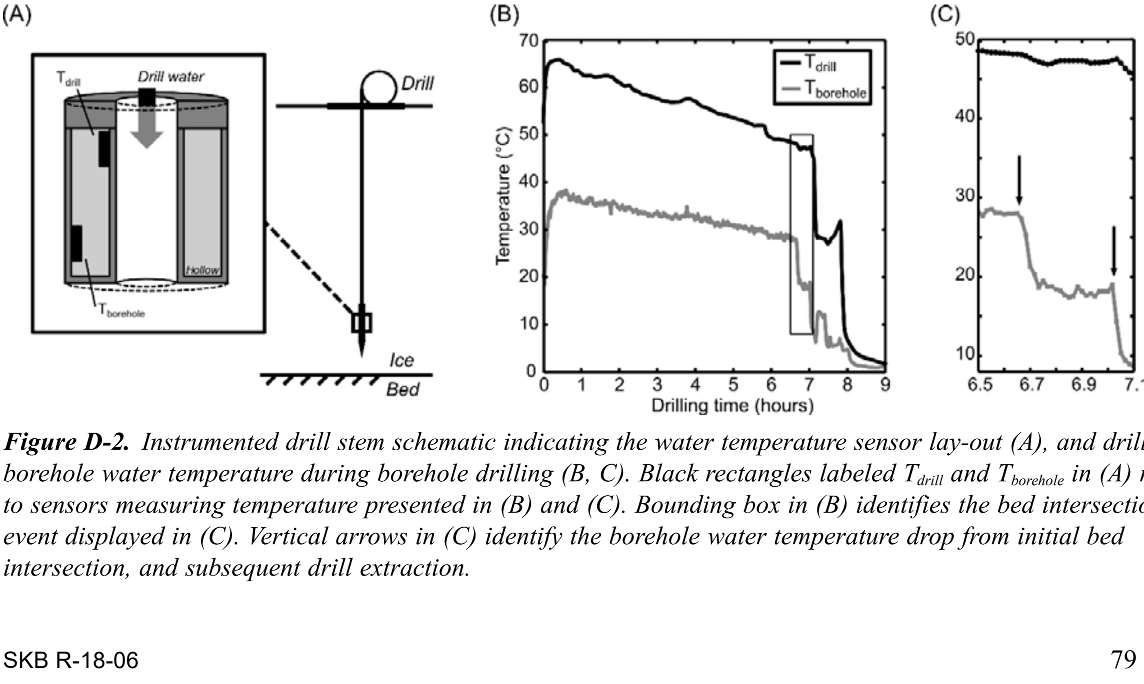

Figure D-2. Instrumented drill stem schematic indicating the water temperature sensor lay-out (A), and drill and borehole water temperature during borehole drilling (B, C). Black rectangles labeled T_{drill} and $T_{borehole}$ in (A) refer to sensors measuring temperature presented in (B) and (C). Bounding box in (B) identifies the bed intersection event displayed in (C). Vertical arrows in (C) identify the borehole water temperature drop from initial bed intersection, and subsequent drill extraction.

We measured borehole water pressure using 2 000 psi, Omega PX309-2KGI pressure transducers which were installed just above the bed and connected to low power dataloggers at the surface via signal cable. Dataloggers were constructed in house and converted analog pressure readings to a digital signal using a 24 bit A/D converter, yielding measurement resolution of approximately 0.1 m water level change. The measurement interval varied from one second to 15 minutes.

D3.6 Surface velocity

Four global positioning system (GPS) units were spaced approximately one ice thickness (700 m) apart in a strain diamond pattern encompassing our field site, and measured positions at 15 second intervals. Kinematic positions were determined by differential processing relative to a base station located ~22 km away in front of the ice sheet margin using TRACK v.1.29 processing software. Reported positional errors are ~1–2 cm. Processed positions were smoothed using a Gaussian filter over a 6 hour window to remove spurious, high frequency noise. Velocities were subsequently calculated over 6 hour time windows following Bartholomew et al. (2012). Over these time intervals, positional errors yield velocity errors of ~30–43 m a^{-1}.

D4 Results

Below, we partition the results in to three different phases based on timing and relevant events.

Stage 1: Borehole drilling (day of year 198)

Drill water temperatures declined over the course of drilling the 675 m borehole from increasing conductive losses as drill hose was payed in to the water-filled hole (Figure D-2b). The thermal signature of bed intersection at the drill stem ~6.65 hours after drilling commenced is characterised by an initial drop in borehole water temperature from 28 °C to 18 °C over 5 minutes (Figure D-2c). After reaching a minimum of 17 °C, water temperature slowly increased to 19 °C when drill extraction began, 20 minutes after initial bed intersection. The change in borehole water temperature occurred in the absence of temperature change in the drill water (Figure D-2c). A second drop in borehole water temperature occurs as a result of drill extraction through cold water higher in the borehole column (Figure D-2b, c).

At the ice surface, bed intersection was characterised by enhanced back-pressure in the drilling water and sudden reduction of load on the drill tower as the drill stem came in contact with the bed. However, the borehole water level remained at the ice surface. Not until the drill was extracted from the borehole ~45 minutes after bed intersection did the water level slowly drop by approximately 65 m. The rate of water input to the hole was greater than the rate of drill hose extraction during recovery so the change in water level does not reflect a volume reduction from drill hose extraction.

Stage 2: Diurnal water pressure swings (days of year 199–209)

Following intersection of the ice sheet bed on day of year 198, water pressure rose steadily for two days to ~50 m above overburden levels (Figure D-3b). The pressure peak was followed by a gradual decrease to below overburden levels and establishment of small diurnal variations. Daily pressure excursions had a range of 4–5 m and were nearly out of phase with diurnal velocity fluctuations (Figure D-3, D-6). Daily pressure minima occurred between ~16:00–21:00 hours local time (UTC −2 during the summer season) and were closely aligned with velocity maxima. Pressure maxima occurred between ~05:00–07:00.

Surface velocities during Phase 2 show consistent diurnal variability with subtle variations in timing and magnitude of diurnal maxima and minima between GPS receivers (Figure D-3a). Minimum daily velocities range from ~120–150 m a^{-1} and rise to daily maxima of ~200–250 m a^{-1}.

Dye concentration slowly increased following installation of the fluorometer before plateauing at a constant concentration of ~95 ppb (Figure D-3c). This steady concentration was diluted from the initial drill water concentration of 610 ppb. Dye concentration remained steady for nearly two weeks with the exception of four periods of erratic behavior when voltage readings showed sporadic drops indicating dye-free conditions. Considering that the these oscillatory excursions immediately recovered to the longer term mean, we interpret them to reflect behavior associated with the fluorometer LED as opposed to real changes in dye concentration. This could result from temporary instrument malfunction if the fluorometer light source failed to power up or from temporary blockage of the light source from basal sediment or other instrumentation at the bottom of the borehole. We favor the latter interpretation as the surface datalogger was programmed to allow sufficient time for fluorometer power-up during sensor excitation.

Stage 3: Termination of diurnal variations (days of year 209 to end)

On day-of-year 209 diurnal pressure variations ended as basal pressure dropped abruptly (Figure D-3b). Erratic pressure behavior ensued. Pressures lower than those during Phase 2 continued through day of year 210, and subsequently increased to levels above local overburden at the end of the experiment. Day 210 also documents a dye disappearance event. Dye concentration briefly increased before steadily declining to 0 ppb over the course of an hour (Figure D-4). This event was followed by persistent dye-free water at the bottom of the borehole which continued until the end of the study period.

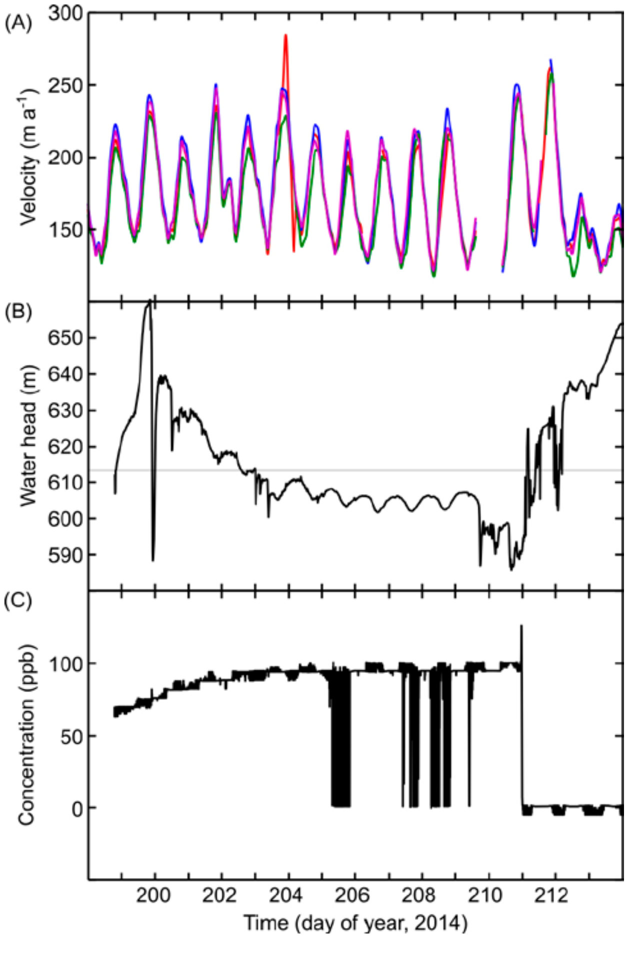

Figure D-3. *GPS surface velocity (A), water pressure expressed as meters head equivalent (B), and dye concentration (C) measured over a 15 day period in 2014. Red, blue, green, and magenta velocity time series' correspond to the west, south, north, and east GPS stations respectively. Gray line in (B) identifies the ice overburden pressure. Sporadic drops in dye time series, evident during days of year 205, 207, 208, and 209, are interpreted to reflect temporary sensor malfunction and not physical changes in dye concentration as discussed in the text.*

Days-of-year 209–210 are marked by a period of low quality GPS positions. Surface position and height show large excursions, in some places exceeding 2 m over short time intervals. Considering that this period overlapped our field season and we did not experience such large changes in surface height, we have omitted this period from the time series. Velocities following the event continued to display diurnal variation; the end of the study period showed the lowest variations of the record (Figure D-3a).

D. 5 Analysis

D5.1 Structure of the local basal system

The three phases described above display characteristic behavior which permit us to make inferences regarding the structure of the local drainage system. Phase 1 is defined by borehole water temperature drop in response to bed intersection during drilling and delayed borehole water level response, with slow drainage occurring ~45 minutes after intersection. Phase 2 is marked by out of phase, diurnal basal water pressure and surface velocity variations in the absence of changing dye concentration. Permanent dye evacuation over one hour marks Phase 3.

Slow or lacking borehole drainage in response to bed intersection during drilling has been previously interpreted to reflect connection to an isolated reach of the glacier bed (Gordon et al. 2001). This interpretation is supported at our field site by the dye concentration time series and thermal signature of bed intersection in the borehole water. In the absence of changes in drill water temperature, borehole water temperature changes reflect three possible scenarios:

Scenario 1: The drill intersects an isolated reach of the bed with no resident basal water (e.g. ice overlying bedrock).

Scenario 2: The drill intersects an isolated basal cavity of unknown volume.

Scenario 3: The drill intersects an active region of the bed with substantial water flow.

Prior to basal intersection, heat energy from drilling acts primarily to overcome the latent heat barrier associated with the phase change from ice to water ahead of the drill tip. In scenario 1 this heat energy is redirected towards melting a cavity around the drill tip and dissipation in bedrock when an isolated system without resident basal water is intersected. In the absence of efficient latent heat transfer directly in front of the drill tip, the expected thermal signature is warming of borehole water closest to the drill as depicted in Figure D-5.

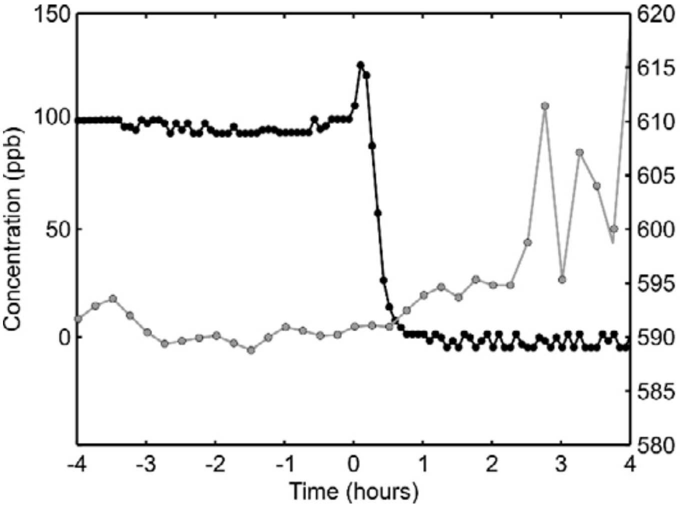

Figure D-4. *Dye concentration and water pressure (expressed in meters head equivalent) during the dye disappearance event on day of year 211. Dye concentration is shown in black, and referenced by the left y-axis. Right y-axis references basal water pressure, which is shown in gray. Time is shown in hours from the initiation of transient dye behavior indicating the beginning of the dye disappearance event.*

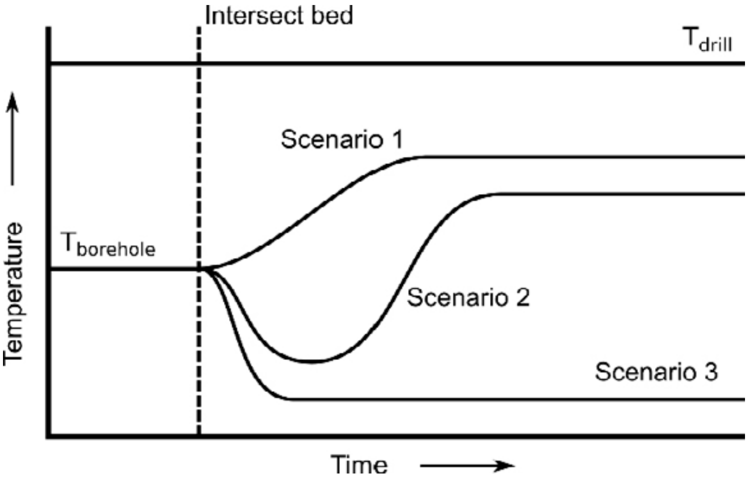

Figure D-5. *Conceptual model of borehole water temperature change in response to drill intersection with the bed for the three potential scenarios described in the text.*

In scenario 2 the drill heat energy undergoes turbulent mixing with resident basal water (initially at the pressure melting temperature) which forces an initial drop in temperature. However, due to the isolated nature of the cavity, the thermal system evolves towards a steady state similar to scenario 1 (Figure D-5). The final steady state temperature in scenario 2 is expected to be a function of the basal cavity geometry; a cavity geometry with larger ice-water contact patch (i.e. larger surface area) will have greater energy transfer to the ice, and hence lower water temperature than scenario 1.

In scenario 3, flowing basal water advects hot drill water away from the immediate basal system, resulting in a new steady temperature that is lower than prior to bed intersection. Alternatively, drainage of the borehole water column could induce a similar effect by advection of colder water from higher in the borehole column. These three conceptual models guide interpretation of water temperature results and allow us to generate constraints on the volume of basal water to which we connected.

The borehole water temperature drop upon bed intersection rules out Scenario 1. It appears that water temperatures slowly began to warm after some time, but a long term warming signature was absent because of drill extraction. However, dye concentrations are constant for nearly 2 weeks after drilling, indicating stagnant conditions at the bed, and this allows us to eliminate Scenario 3. Further, the borehole water level remained at the surface when the bed was intersected, eliminating the advection of borehole column water as a cooling source.

Taken together, measured dye concentrations and the thermal signature of the borehole water temperature during drilling strongly suggest connection to an isolated basal cavity. Further, steady dye concentrations indicate that this cavity remains unconnected for nearly two weeks after drilling. Because borehole water temperature drops at bed intersection, and measured dye concentration is dilute from the injected concentration, the basal cavity must be water-filled. In this event, the magnitudes of cooling and dilution, respectively, provide an indication of the volume of the isolated cavity. Next, we provide first-order estimates of cavity volume by considering thermal dissipation and dye dilution.

D5.2 Basal cavity volume

In estimating cavity volume from dye dilution, the measured dye concentration (C_{final}) of 95 ppb is the result of mixing of resident cavity basal water volume (V_{res}), dyed drill water (C_{drill}, V_{drill}), clean ice melted during drilling ($C_{melt} = 0$, V_{melt}), and borehole column water from delayed borehole drainage (C_{bh}, V_{bh}). The individual water volumes V_i and dye concentrations C_i mix to form the final measured solution concentration following the dilution equation:

$$\sum(C_i V_i) = C_{final} \sum V_i \; . \qquad \text{(D-1)}$$

Rearranging Equation D-1 and substituting dye concentration and volume from each of the mixing components above thus permits estimation of the basal cavity volume:

$$V_{res} = \frac{\left[C_{bh}V_{bh} + C_{drill}V_{drill}\right]}{C_{final}} - \left(V_{bh} + V_{melt} + V_{drill}\right). \qquad \text{(D-2)}$$

We estimate the melted ice volume (V_{melt}) from the measured temperature difference between drill water and borehole water, assuming that this thermal energy goes to the phase change in melting ice, and warming that melt to the ambient temperature of the borehole water. Borehole volume (V_{bh}) is estimated from the observed water level drop following drilling, assuming a cylindrical borehole with radius of 0.06 m. Drill volume is estimated from the drilling discharge rate and time spent drilling at the bed. Dye concentration of the borehole column is taken from the initial dye profile in the column during deployment of the fluorometer. With these considerations, and propagating the estimated uncertainty for each quantity (shown in Table D-1) following Taylor (1997), we calculate the estimated cavity volume from dye dilution to be 7.6 +/− 6.7 m^3.

Table D-1. Variables, variable values, and estimated uncertainties.

Variable	Value	Uncertainty (+/−)	Units	Description
L	3.34e5	–	J kg^{-1}	Latent heat of fusion
c_p	4186	–	J kg^{-1} $°C^{-1}$	Specific heat capacity of water
ρ_w	1000	–	kg m^{-3}	Density of water
ρ_i	910	–	kg m^{-3}	Density of ice
T_{drill}	50	3	°C	Drill water temperature
T_{hole}	25	3	°C	Borehole water temperature
T_{pmp}	−0.58	0.01	°C	Basal pressure melting temperature
Q_{drill}	0.076	7.6e-3	m^3 min^{-1}	Drill flow rate
t	20	1	min	Time spent at the bed
C_{drill}	610	10	ppb	Drill water dye concentration
C_{bh}	63	3	ppb	Borehole dye concentration
C_{final}	95	1	ppb	Final measured basal dye concentration
r	0.06	0.01	m	Borehole radius
h	65.	3	m	Length of drained borehole column

We estimate basal water volume from thermal dissipation by using the temperature change in borehole water during bed intersection as a thermal signature of the basal system. The temperature drop in borehole water (T_{pmp}) reflects the change in energy consumption at the bed:

$$\Delta\dot{E} = Q_{drill}c_p\rho_w\Delta T \qquad \text{(D-3)}$$

where variables are defined in Table D-1. Integration of Equation D-3 over the duration of time spent drilling at the bed yields a first-order estimate of the total change in energy consumption. We assume that this change in energy acts solely to warm resident basal water from the pressure melting temperature (T_{pmp}) to the temperature of the borehole water. This is a function of the resident basal water volume (V_{res}):

$$E = V_{res}\rho_w c_p\left(T_{hole} - T_{pmp}\right). \qquad \text{(D-4)}$$

We estimate ΔT to be 11 °C in computing the total change in energy consumption from Equation D-3. We substitute this value in the left hand side of Equation D-4, and calculate a basal cavity volume from thermal dissipation of 1.1 +/− 0.9 m^3.

Calculating basal volume from dye dilution assumes that there is complete mixing between resident water, ice melt, drill water, and borehole column water. However, the small increase in dye concentration just prior to the dye disappearance event (Figure D-4) suggests that complete mixing was not achieved and so the dye dilution calculation is a maximum estimate. With this in mind, and considering the uncertainty of the estimates, the two independent methods show the cavity volume is less than tens of cubic meters, but likely to be larger than one.

D6 Discussion

Ice sheet and glacier sliding dynamics are influenced by basal drainage processes. The coupling between drainage dynamics and ice motion is commonly assigned to basal water pressure, which responds to local water flux so that surface meltwater ultimately forces basal motion (e.g. Hewitt 2013, Hoffman and Price 2014). Our results identify pressure variations over diurnal periods in the absence of water flow, and GPS measurements show that these diurnal pressure variations are out of phase with respect to surface velocity (Figure D-6a, b). Estimates from dye and thermal dissipation considerations suggest that these pressure variations act on a cavity with volume that is on the order of cubic meters. Roughness along the bed opening up basal cavities is inherently unconstrained, but bedrock bump heights are generally assumed to be on the order of decimeters as enhanced deformation may flow around bumps larger than meter-scale. Thus, it is plausible that our measured pressure variations act over areas of the bed that are on the order of many tens of square meters.

Similarly out of phase basal pressure and surface velocity behavior has been identified on Greenland by Ryser et al. (2014a) and Andrews et al. (2014) in boreholes that were interpreted to be connected to an isolated reach of the bed. The observed prevalence of such pressure variations and likelihood that they act over a measurable area of the bed motivate investigation of other, potentially non-local sources that may influence basal pressure dynamics.

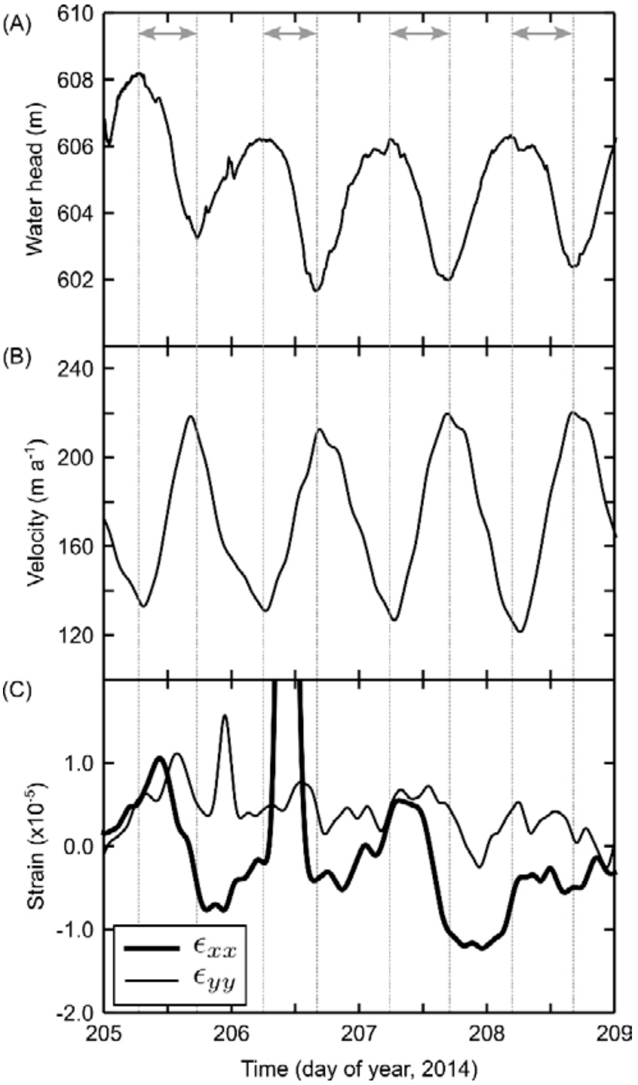

Figure D-6. Measured water pressure in meters head equivalent (A), velocity from the east GPS station (B), and detrended strain from the GPS strain grid (C) over a 4 day period from day of year 205–209. Bold black line shows ε_{xx}, and thin line shows ε_{yy} in (C). Strain in (C) is calculated by linearly detrending the cumulative strain over the time series, which is shown in Figure D-7. Periods of interest from daily water level maxima to minima are shown by the gray vertical lines and horizontal arrows.

Pressure changes in isolated cavity space can be invoked through changes in volume. The equation of state for water relates density changes to changes in pressure (Clarke 1987, Kavanaugh 2009, Murray and Clarke 1995):

$$\rho_w(p) = \rho_w(p_0)\exp[\beta(p - p_0)] \tag{D-5}$$

where P_0 is a reference water pressure, and β is the compressibility of water (taken here to be 5.1×10^{-10} Pa^{-1}). Assuming mass is conserved, density change is the result of volume change alone, and Equation (D-5) is rearranged to yield the volume change associated with a pressure perturbation:

$$\frac{V(p)}{V(p_0)} = \frac{1}{\exp[\beta(p - p_0)]}. \tag{D-6}$$

Due to water's incompressible nature, pressure excursions result from small changes in volume: a pressure change similar to the diurnal variations we observe in our boreholes (5 m head equivalent) can be induced by a volume change of ~2.5×10^{-3} %.

Small volume changes could be induced from three mechanisms, each forced by overlying ice dynamics rather than local water flow: (1) daily changes in longitudinal straining of the cavity/borehole system, (2) opening of cavity space through accelerations in glacier sliding over a bedrock bump, and (3) load transfer at the bed resulting from elastic displacement of the ice roof in response to pressure increases in nearby connected regions. We assess the plausibility of each below.

D6.1 Longitudinal effects

If longitudinal extension and compression is great enough on a daily scale, the resultant straining of the coupled borehole-cavity system could induce the measured pressure diurnal variations. Over the duration of the time series, cumulative strain across the GPS strain diamond shows net extension (positive strain) in the Cartesian y-direction, and compression in the x-direction (Figure D-7). However, by linearly detrending the cumulative strain time series to remove longer term trends, and comparing this detrended time series to the basal water pressure, surface strain changes over the half-cycle from high to low water pressure show little evidence of extension (Figure D-6). Instead, the dominant trend appears to be compression in the x-direction, which would imply squeezing of the borehole/cavity system.

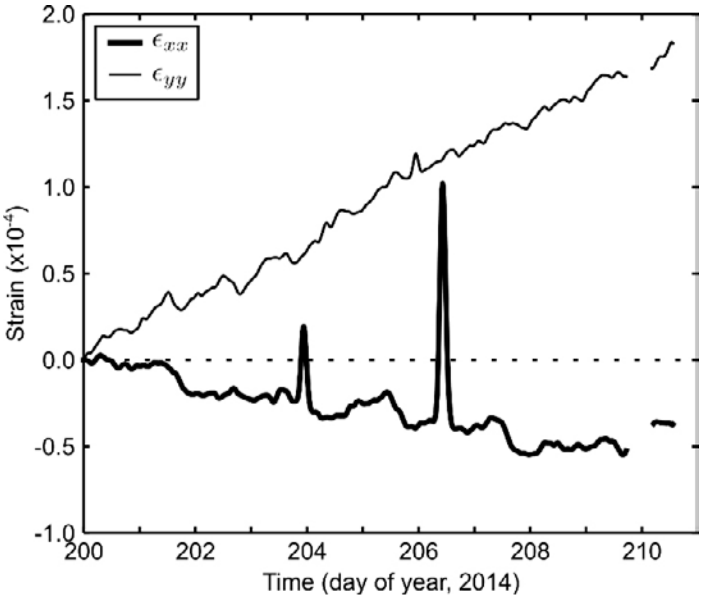

Figure D-7. Cumulative strain calculated over the GPS strain diamond during the study period. Bold black line shows ε_{xx}, and thin line shows ε_{yy}. Positive strain indicates extension, and negative values indicate compression. Horizontal dashed line indicates 0 strain. Break in time series corresponds to the period of high GPS position variability as discussed in the text. Due to resetting of the GPS units, the time series terminates before the end of the velocity record in Figure D-3.

The lack of clear tensile strain in the GPS strain diamond during basal pressure decline leads us to conclude that longitudinal stretching is unlikely to force the measured pressure variations. This result contrasts with Ryser et al. (2014a), who successfully reproduced measured out-of-phase surface velocity and basal pressure behavior using a numerical ice flow model, and concluded that the out-of-phase behavior resulted from longitudinal stress coupling between passive slippery (i.e. isolated) reaches at the bed and sticky reaches undergoing transient changes in basal traction. Inferring basal conditions from surface strain calculations as we have done ignores complicating processes through the ice column and may thus be an oversimplification, but the result of Ryser et al. (2014a) also requires longitudinal extension through the full ice thickness (e.g. see Ryser et al. (2014a) Figure 10). Alternatively, the fact that our measured pressure variations occur below ice overburden suggests that our borehole may connect to a different basal setting than the drainage system studied by the authors. Thus, isolated pressure variations that are out of phase with surface velocity may also be forced by other processes that occur outside of a setting that is near transition from slippery to sticky.

D6.2 Cavity opening from sliding

To examine cavity opening, we restrict our analysis by assuming that the change in cross-sectional area of the cavity is proportional to the change in volume. Thus, in an isolated system, Equation D-6 implies that cavity opening increases cavity volume which enforces a drop in water pressure (i.e. when $\frac{dS}{dt} > 0$, $\frac{dp_w}{dt} < 0$) and vice versa. This implies that $\frac{dS}{dt} = 0$ when $\frac{dp}{dt} = 0$ (e.g. at water pressure minima and maxima), which is satisfied twice daily under diurnal pressure variations. In the absence of melting induced by water flow, cavity opening from sliding is countered by closure from creep of the overlying ice roof (Schoof 2010):

$$\frac{dS}{dt} = u_b h_s - cSN^n \, . \tag{D-7}$$

where u_b is sliding velocity, h_s is the bedrock step height, c is a constant reflecting the ice viscosity, S is cavity cross sectional area, $N = p_i - p_w$ is effective pressure, and n is Glen's flow exponent, which we take to be 3. Our velocity results suggest that the sliding rate is also likely to vary at these two points in time. If we assume that diurnal velocity variations are due to changes in basal motion alone, then daily sliding increases from some baseline level when water pressure is high ($u_b\ (p_{max})$), to a faster speed when water pressure is low ($u_b\ (p_{min}) = u_b\ (p_{max}) + \Delta u$), by some amount Δu. Because $\frac{dS}{dt} = 0$ at pressure minima and maxima, this permits cross sectional area to be isolated in Equation D-7 at these times. Substituting the above expressions for sliding velocity, and computing the fractional change in area at these two instances yields:

$$\frac{S(p_{min})}{S(p_{max})} = \frac{\left(u_b(p_{max}) + \Delta u\right)}{u_b(p_{max})} \left[\frac{p_i - p_{max}}{p_i - p_{min}}\right]^n \tag{D-8}$$

where ice viscosity (c) and bedrock step height (h_s) cancel. Assuming that volume changes in the cavity result from cross sectional area changes alone, Equation D-8 indicates that, under the basal cavitation conceptual model, the pressure-volume relationship from Equation D-6 can only be achieved under specific baseline sliding conditions ($u_b\ (p_{max})$) if water pressures p_{min} and p_{max}, and velocity change Δu are known.

Our observations permit us to estimate p_{max} and p_{min} over the diurnal cycle. During this period, surface velocity changes by ~100 m a^{-1} (Δu = 100 m a^{-1}). Under these conditions, we calculate that baseline sliding velocity must be approximately 32 m a^{-1}. However, the sliding result is quite sensitive to small uncertainties in the ice thickness. Thickness uncertainties of +/− 3m invoke a sliding velocity uncertainty of +/− 18 m a^{-1}. Thus, background sliding on the order ~30–50 % of the minimum measured surface velocity (~120 m a^{-1}) satisfies the estimated pressure-volume relationships. In comparison, in a similar setting in Western Greenland Ryser et al. (2014b) reported basal motion can exceed 90 % of surface motion in the summer (and 44–73 % in the winter). Large variations in sliding velocity are likely across Greenland's ablation zone, and so while our estimate appears low, we cannot eliminate sliding-induced cavity opening as a mechanism controlling the measured pressure variations from our analysis.

D6.3 Load transfer

Murray and Clarke (1995) presented a conceptual model whereby pressure increases in a hydraulically active region of the bed elastically displaced the overlying ice roof, mechanically increasing the volume of nearby isolated cavity space. Assuming a simplistic, rectangular cavity with an initial height between 0.15–0.5 m, the necessary volume expansion we calculate requires raising the ice roof ~4–12 μm respectively. Murray and Clarke (1995) found that similar roof expansion values could be induced by pressure pulses on the order of 10 m head equivalent in a connected system <10 m away. Our documented dye disappearance event indicates active drainage elements persist close to our cavity, meaning a potential source exists for pressure pulses within active reaches of the bed. Elastic displacement of the overlying ice roof of the isolated cavity thus appears to be a plausible mechanism for inducing pressure perturbations.

The load transfer conceptual model is poorly constrained in that the size of the connected reach, magnitude of pressure disturbance, and distance from the isolated pocket all influence the corresponding response in the unconnected cavity. The fact that our measured dye evacuation event occurred over one hour, coupled with our volume estimates, implies that the flow rate through active drainage elements is on the order of ~0.1 m^3 min^{-1}. Large preexisting conduits (i.e. meter diameter) would likely have the capacity to evacuate the stored basal water in seconds to minutes. Thus, if pressure pulses in connected basal features elastically displace the ice roof and drop pressure in the isolated area, it appears that the connected reach must be composed of small nearby drainage elements as opposed to a large distal melt conduit.

D7 Conclusions

A suite of measurements at the surface and within a borehole provide in situ constraints on basal conditions of the GrIS at a site located 34 km inland from the outlet stream where the ice is nearly 700 m thick. Borehole water temperature and in situ dye tracing at the bed via borehole injection indicates connection to an isolated basal cavity, which we estimate to be on the order of cubic meters in size. Measurements of basal water pressure in the isolated cavity show diurnal swings which are out of phase with surface velocity recorded by a GPS strain diamond encompassing the borehole measurement. Because dye measurements indicate no local water flow at the bed, it is plausible that measured pressure changes are due to small changes in volume of the coupled borehole-cavity space.

Our in situ measurements provide direct example that changes basal water pressure can be a complex function of processes other than local water flux. In our case, longitudinal coupling effects are not responsible for pressure variations, but accelerated cavity opening and load transfer from elastic uplift are plausible mechanisms for volume/pressure changes at the bed. If load transfer is responsible for pressure variations, connected reaches of the bed are likely to consist of small nearby flowpaths as opposed to large distal melt conduits. Thus, horizontally and vertically directed mechanical processes may induce important pressure variations over isolated reaches of the bed and need to be considered in the relationship between water flux, water pressure and sliding speed.

D8 Acknowledgments

This work is funded by NSF (Office of Polar Programs-Arctic Natural Sciences grant no. 0909495), SKB, Posiva, NWMO, NAGRA, and NASA grant NNX11AM12A. Discussions with J. V. Johnson helped guide the manuscript analysis. C. Florentine assisted with instrument calibration and field experiments.

D9 References

Andrews L C, Catania G A, Hoffman M J, Gulley J D, Lüthi M P, Ryser C, Hawley R L, Neumann T A, 2014. Direct observations of evolving subglacial drainage beneath the Greenland ice sheet. Nature 514, 80–83.

Bamber J L, Griggs J A, Hurkmans R T W L, Dowdeswell J A, Gogineni S P, Howat I, Mouginot J, Paden J, Palmer S, Rignot E, Steinhage D, 2013. A new bed elevation dataset for Greenland. The Cryosphere 7, 499–510.

Bartholomew I, Nienow P, Mair D, Hubbard A, King M A, Sole A, 2010. Seasonal evolution of subglacial drainage and acceleration in a Greenland outlet glacier. Nature Geoscience 3, 408–411.

Bartholomew I, Nienow P, Sole A, Mair D, Cowton T, King M A, 2012. Short-term variability in Greenland Ice Sheet motion forced by time-varying meltwater drainage: Implications for the relationship between subglacial drainage system behavior and ice velocity. Journal of Geophysical Research 117, F03002. doi:10.1029/2011JF002220

Clarke G K C, 1987. Subglacial till: A physical framework for its properties and processes. Journal of Geophysical Research 92, 9023–9036.

Gordon S, Sharp M, Hubbard B, Willis I, Smart C, Copland L, Harbor J, Ketterling B, 2001. Borehole drainage and its implications for the investigation of glacier hydrology: experiences from Haut Glacier d'Arolla, Switzerland. Hydrological Processes 15, 797–813.

Graly J A, Humphrey N F, Landowski C M, Harper J T, 2014. Chemical weathering under the Greenland ice sheet. Geology 42, 551–554.

Harrington J A, Humphrey N F, Harper J T, 2015. Temperature distribution and thermal anomalies along a flowline of the Greenland ice sheet. Annals of Glaciology 56, 98–104.

Hewitt I J, 2013. Seasonal changes in ice sheet motion due to melt water lubrication. Earth and Planetary Science Letters 371–372, 16–25.

Hoffman M J, Catania G A, Neumann T A, Andrews L C, Rumrill J A, 2011. Links between acceleration, melting, and supraglacial lake drainage of the western Greenland ice sheet. Journal of Geophysical Research, 116, F04035. doi:10.1029/2010JF001934

Hoffman M, Price S, 2014. Feedbacks between coupled subglacial hydrology and glacier dynamics. Journal of Geophysical Research: Earth Surface 119, 414–436.

Iken A, Truffer M, 1997. The relationship between subglacial water pressure and velocity of Findelengletscher, Switzerland, during its advance and retreat. Journal of Glaciology 43, 328–338.

Kavanaugh J L, 2009. Exploring glacier dynamics with subglacial water pressure pulses: Evidence for self-organized criticality? Journal of Geophysical Research 114, F01021.

Leuschen C, Gogineni P, Rodriguez-Morales F, Paden J, Allen C, 2010. IceBridge MCoRDS L2 Ice Thickness, Version 1. Boulder, CO USA: NASA DAAC: NASA DAAC at National Snow and Ice Data Center: NASA National Snow and Ice Data Center Distributed Active Archive Center. doi:http://dx.doi.org/10.5067/GDQ0CUCVTE2Q

Lliboutry L, 1976. Physical processes in temperate glaciers. Journal of Glaciology 16, 151–158.

Meierbachtol T, Harper J, Humphrey N, 2013. Basal drainage system response to increasing surface melt on the Greenland Ice Sheet. Science 341, 777–779.

Meierbachtol T W, Harper J T, Johnson J V, Humphrey N F, Brinkerhoff D J, 2015. Thermal boundary conditions on western Greenland: Observational constraints and impacts on the modeled thermomechanical state. Journal of Geophysical Research: Earth Surface 120, 623–636.

Murray T, Clarke G K C, 1995. Black-box modeling of the subglacial water system. Journal of Geophysical Research 100, 10231–10245.

Ryser C, Lüthi M P, Andrews L C, Catania G A, Funk M, Hawley R, Hoffman M, Neumann T A, 2014a. Caterpillar-like ice motion in the ablation zone of the Greenland ice sheet. Journal of Geophysical Research: Earth Surface 119, 2258–2271.

Ryser C, Lüthi M P, Andrews L C, Hoffman M J, Catania G A, Hawley R L, Neumann T A, Kristensen S S, 2014b. Sustained high basal motion of the Greenland ice sheet revealed by borehole deformation. Journal of Glaciology 60, 647–660.

Schoof C, 2010. Ice-sheet acceleration driven by melt supply variability. Nature 468, 803–806.

Taylor J R, 1997. An introduction to error analysis. 2nd ed. Mill Valley, CA: University Science Books.

Weertman J, 1964. The theory of glacier sliding. Journal of Glaciology 5, 287–303.

Werder M A, Hewitt I J, Schoof C G, Flowers G E, 2013. Modeling channelized and distributed subglacial drainage in two dimensions. Journal of Geophysical Research: Earth Surface 118, 2140–2158.

Zwally H J, Abdalati W, Herring T, Larson K, Saba J, Steffen K, 2002. Surface melt-induced acceleration of Greenland Ice-Sheet flow. Science 297, 218–222.

Appendix E

Local basal water storage: assessment of estimates from surface elevation measurements

E1 Abstract

Changes in water storage at the bed of glaciers and ice sheets has implications for sliding dynamics and water exchange with the groundwater system by influencing water coverage at the ice – bed interface. Determining changes in water storage at the bed with confidence, however, is difficult because direct measurements are not possible. Inferring changes in basal storage from surface elevation variations along a network of GPS stakes frozen in the ice is a commonly implemented indirect method, but requires knowledge and/or assumptions regarding basal topography and vertical strain through the ice column. Here, the dense measurement network across the block site, including a strain diamond of five GPS units and in-situ inclinometers through the ice column, is used to compute changes in water storage during the transition from winter to summer melt conditions, and evaluate the fidelity of the method. Results show that two primary velocity speed-ups occur during the 2016 winter to summer melt season transition. Despite a measured sliding velocity that is an extremely high fraction of the surface speed, vertical strain rates vary substantially with depth. Consequently, computed basal storage is highly sensitive to the choice of the depth-interval over which vertical strain rates are averaged. Preliminary results identify increasing basal storage during the transition from winter to summer, but the high sensitivity to vertical strain within the ice column makes this result uncertain. The assumption that surface vertical strain rates do not change with depth is not supported by in situ measurements. Studies which compute basal water storage changes under the assumption that surface vertical strain rate reflects conditions at depth should be interpreted with caution.

E2 Introduction

It is well established that basal water and glacier and ice sheet sliding are intimately linked (e.g. Harper et al. 2007, Hoffman et al. 2011, Bartholomew et al. 2012), but critical details of the forcing and response remain elusive. On the GrIS, variations in surface velocity have been observed to follow melt production over diurnal to seasonal time scales (Bartholomew et al. 2010, 2012, Sundal et al. 2011), and has motivated a common narrative that water pressure in the subglacial drainage system controls changes in sliding rates. This hypothesis is supported by direct observations on some mountain glaciers (Iken and Bindschadler 1986, Jansson 1995, Sugiyama et al. 2011), but is contradicted by the few existing observations on the GrIS (Andrews et al. 2014, Meierbachtol et al. 2016). Alternatively, because a water layer separating basal ice from bedrock cannot support shear stress, it has been hypothesised that changes in the amount and coverage of water at the bed are also key controls on basal sliding (Bartholomaus et al. 2008, Harper et al. 2007, Kamb et al. 1994). This hypothesis remains largely untested on the GrIS, however, because bed storage changes remain unquantified.

In addition to ice flow dynamics, basal water coverage has implications for water exchange between the subglacial drainage system and underlying groundwater regime. Where ice rests on hard bedrock, groundwater recharge depends on areas of intersection between bedrock fractures and subglacial drainage elements providing a water source. In this way, basal water storage is a potentially important boundary condition between the ice and groundwater systems that is accommodated in few groundwater studies.

Attempts to quantify water storage beneath ice masses are rare because the remote nature of the domain precludes direct observation. The absolute quantity of subglacial storage is unmeasurable, and changes in basal water are more likely to exert the more important control on ice flow. Past works have therefore focused efforts on measuring changes in water storage. On smaller mountain glaciers, this has been achieved through two main approaches: 1) A generalised water budget approach in which the timing of inputs and outputs is quantified and used to determine periods of increasing or decreasing storage (e.g. Bartholomaus et al. 2008, Kamb et al. 1994, Schuler et al. 2002), or 2) changes in ice surface elevation are measured, and bed storage is computed as the residual term after accounting for other glaciological processes (see Methods below) (e.g. Andrews et al. 2014, Doyle et al. 2015, Harper et al. 2007, Hoffman et al. 2011, Hooke et al. 1989, Mair et al. 2002).

On the GrIS, calculation of a water budget is inherently unconstrained. The timing of surface meltwater input can be variable over a contributing domain that is: A) large (100s of km^2), B) sensitive to bedrock topography that is generally only loosely known, and C) is also prone to change over time as the catchment size may vary due to changing subglacial drainage system pressure (e.g. Lindbäck et al. 2015, Wright et al. 2016). This motivates investigation of basal storage changes through surface elevation variations as essentially the only way to constrain large scale changes in water volume at the bed.

Quantification of basal storage changes from a time series of surface elevation requires that ice flow effects from bed-parallel motion and vertical strain through the ice column be constrained, leaving storage change as the residual. In practice such constraints on flow conditions have not been available on the GrIS, requiring simplifications be made when computing the residual basal storage term. The effects of these simplifications on the results are unknown. In this chapter, we use the unique suite of in situ data at the block site to eliminate the necessity for such simplifications, and assess whether the incorporation of measured constraints on ice flow improves the confidence of quantified seasonal changes in basal water storage.

E3 Methods

E3.1 Basal storage framework

Vertical changes of markers frozen into the ice near the surface are independent of surface melting effects, and are attributable to three different glaciological processes: 1) bed parallel motion from ice sliding over sloping bedrock, 2) integrated vertical strain through the full ice column, and 3) vertical motion of the ice block reflecting displacement from bulk changes in the amount of water at the bed. This can be written in equation form as:

$$w = u_b \tan\theta + \overline{\dot{\epsilon}_{zz}} H + \dot{c} \qquad \text{(E-1)}$$

where w is the measured vertical velocity at the surface, u_b is the ice sliding velocity, θ is the bed slope from horizontal, $\overline{\dot{\epsilon}_{zz}}$ is the average vertical strain rate, H is the ice thickness, and $\dot{c}$ is the time rate of vertical displacement change due to bed storage. In theory, Equation 1 requires detailed knowledge of the bedrock geometry, basal sliding conditions and englacial flow conditions to quantify bed storage changes from observations of surface elevation change.

Because of the challenges associated with constraining englacial ice flow, it is commonly assumed that ice flow occurs purely through basal sliding, so that the sliding velocity is equal to the surface velocity and vertical strain is invariant with depth (e.g. Howat et al. 2008, Hoffman et al. 2011, Andrews et al. 2014, 2018). Basal sliding velocity in the bed-parallel term in Equation 1 is replaced with the surface velocity (u_s) and the vertical strain term is replaced with $\dot{\epsilon}_{zz,\,sfc}H$ where H is the ice thickness. This greatly simplifies Equation (E-1) by limiting all variables to ice geometry and surface measurements.

The simplifications of ice flow dynamics in terms of surface observations ease data requirements but the uncertainty associated with the assumptions is folded in to the bed storage residual, potentially compromising the results. At the ICE project block site, englacial ice flow is constrained to a degree that is unprecedented on the GrIS, and should eliminate the need for these assumptions. Below, we assess whether the improved ice flow constraints permit changes in bed storage to be estimated with increased fidelity.

E3.2 Field data

In this chapter we focus the bed storage analysis on the winter thru summer melt seasons of 2016, from days of year 120 (April 29) to 220 (August 7). Data collection during the 2016 field campaign in August results in termination of the time series before the end of the melt season. The remaining data were collected in 2017 and are currently undergoing processing and will be incorporated in to the analysis when available. Because the full 2016 melt season is not captured, we focus on the spring – summer transition here.

The analysis relies on surface motion data, constraints on englacial ice flow, and information on ice geometry over the site. Surface motion is measured by five GPS stations, arranged in a strain diamond configuration spanning the site (Figure E-1). Details of the collection and processing of these data are provided in Appendix D. Airborne radar from an IceBridge flightline, collected in 2011 and passing directly through the block site, yields an along-flow profile of bedrock topography (Figure E-2).

Constraints on ice flow come from in situ ice deformation measured in three boreholes at the site (15-CB, 15-S, and 15-EB), spaced approximately 150 m apart and arranged in a triangular orientation (Figure E-1). Sensor strings, deployed in boreholes and frozen in place, measured vertical tilt along two orthogonal axes at 10 to 20 m spacing through the full ice column, and at time intervals of 2 hours. These data were processed to yield tilt rates in the x- and y-directions, and oriented in the flow direction by assuming that the tilt direction followed the ice flow direction during the quiescent winter period (three dimensional magnetic data was measured by the tilt sensors as well and is currently being processed; quantifying sensor orientation confidently is made difficult by the magnetic field vector at the site, which points nearly vertical). Tilt rates were converted to rates of vertical shear at each borehole depth interval; further processing to generate time series' of basal sliding and vertical strain rate is described below.

E3.3 Approach

To minimise variability in surface vertical velocity calculations as well as the borehole tilt time series, all data were smoothed over a 5 day window using a Gaussian filter. This choice of smoothing window increases confidence in observed rates of change while still revealing multi-day changes that are observed during the spring to summer melt season transition.

Vertical shear profiles were integrated and subtracted from velocities measured at the surface to yield velocity profiles with depth at each borehole. The bottom measurement provides an in-situ quantification of the basal sliding velocity through time.

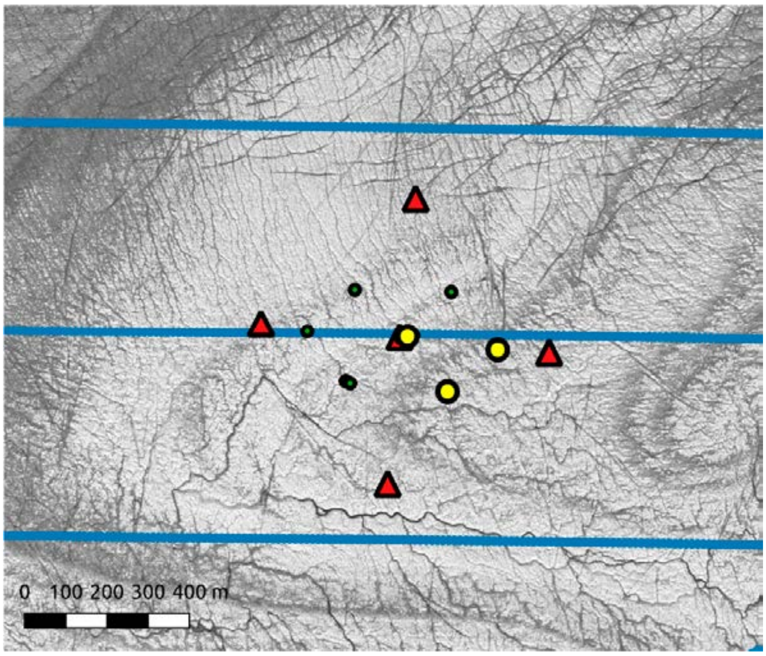

Figure E-1. *ICE project block site setting. GPS positions are shown as red triangles. Drilled boreholes are shown as green circles, and boreholes used in the basal storage analysis are shown as large yellow circles. Blue lines show IceBridge radar profiles passing through the site. Ice flow direction approximately parallels the IceBridge radar profile lines from right to left.*

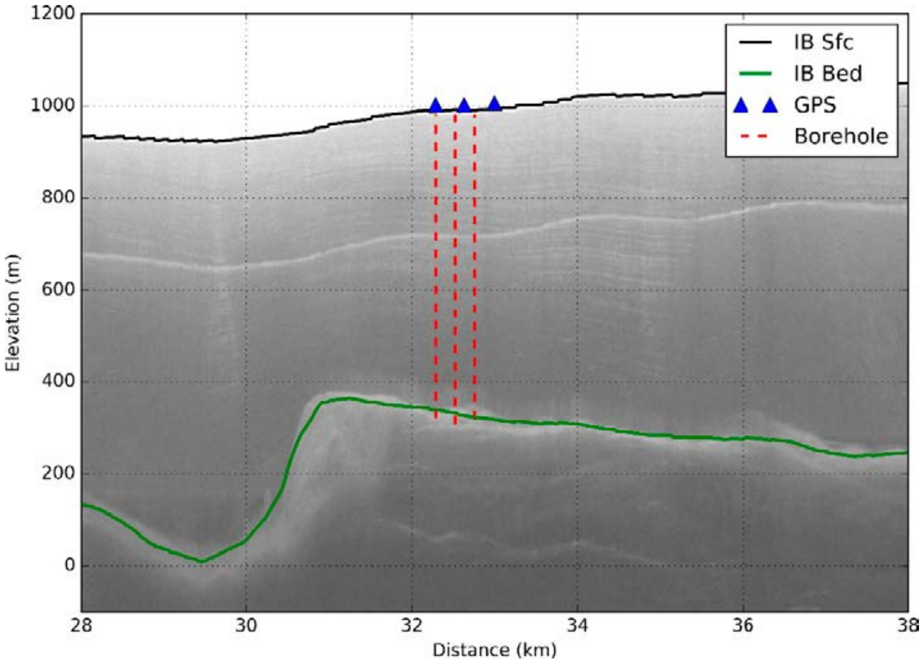

Figure E-2. *IceBridge radargram passing through the middle of the ICE project block site. Blue triangles show GPS positions on the day of installation, dashed red vertical lines identify locations of boreholes. Green line is the IceBridge provided bed pick, illustrating the reverse bedrock slope. Ice flow direction is from right to left.*

Using the orthogonal horizontal velocities quantified with depth in each borehole, normal strain rates $\dot{\epsilon}_{xx}$ and $\dot{\epsilon}_{yy}$ were computed at the centroid of the three-borehole triangle, and for each depth interval. Assuming that ice is an incompressible medium, the vertical strain rate at each depth (h) was then calculated from continuity:

$$\dot{\epsilon}_{zz}(h) = -(\dot{\epsilon}_{xx}(h) + \dot{\epsilon}_{yy}(h)) \tag{E-2}$$

The resulting vertical strain profile was then averaged to yield an average vertical strain at each time step.

The IceBridge radar profile through the study site offers a direct constraint on bedrock topography that is necessary to quantify vertical change from bed-parallel flow (Figure E-2). However, the diffuse bed reflection through the study area leaves some uncertainty as to the fidelity of the automatic picking routine that defines the bed surface. Instead, we follow an alternative approach. We assume that changes in bed storage are negligible during the winter period, and use the field constraints on vertical surface motion, sliding velocity, and vertical strain to estimate the required bed topography slope (θ). The IceBridge radar profile provides an important independent verification of the computed bed slope.

E4 Results

E4.1 Ice flow and geometry components

Surface velocity

Surface velocity at the site underwent two accelerations (Figure E-3). Velocities increased by nearly 50 m a^{-1} on May 14 (doy 134), and remained elevated for more than two weeks prior to the primary acceleration which occurred contemporaneously with the onset of the summer melt season. Beginning on June 7 (doy 157), surface speed more than doubled over 10 days, reaching a peak 5-day average of 275 m a^{-1}. Melt season velocities remained elevated until the end of the time series.

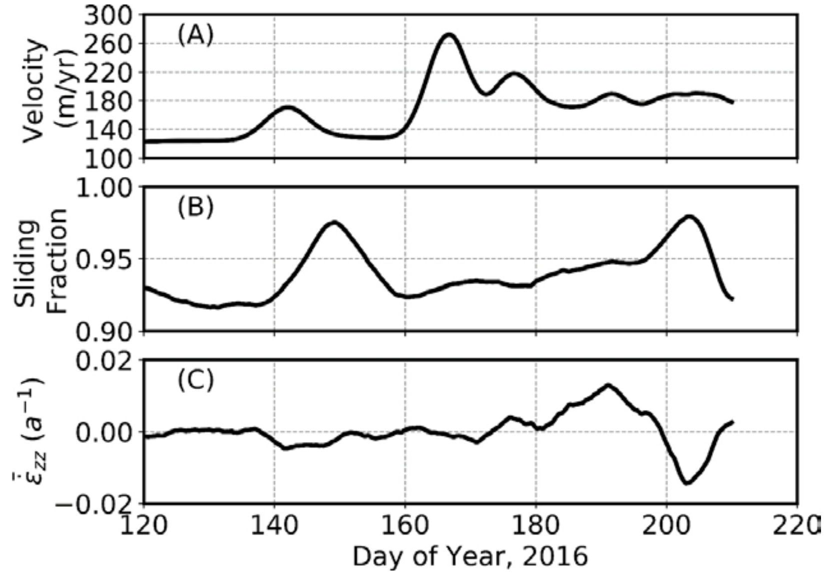

Figure E-3. *Smoothed surface velocity time series at the centroid of the borehole triangle (A), sliding fraction computed from measured deformation profiles in three boreholes (B), and average vertical strain from the surface to a depth of 550 m at the centroid of the borehole triangle (C).*

Sliding velocity

Deformation profiles from the three boreholes reveal that ice flow at the site occurs nearly entirely through basal sliding (Figure E-3, E-4). During the winter period more than 92 % of surface motion occurs at the bed. The sliding fraction changes with time, increasing to 98 % of the surface motion. Interestingly, the greatest increases in the sliding fraction do not occur during the largest surface acceleration.

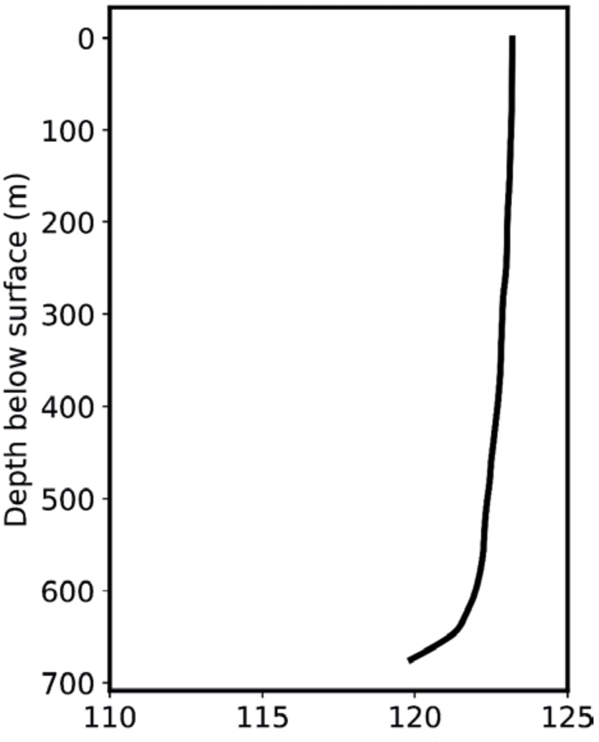

Figure E-4. *Example velocity profile from two-axis tilt measured in borehole 15-EB on 2016 day of year 125.*

Vertical Strain

Despite nearly all surface motion occurring at the bed, vertical strain calculated from the borehole network varies strongly with depth (Figure E-5). Vertical thinning near the ice surface transitions to large rates of vertical thickening at depth. This substantially complicates the basal storage analysis. Close to the ice sheet bed, borehole deformation profiles may be strongly influenced by local sticky spots or bedrock bumps. These local effects would have a large influence on the computed vertical strain rate, but do not reflect conditions over the larger borehole network that the basal storage calculation assesses.

An alternative approach is to average the vertical strain rate over a fraction of the ice thickness, avoiding the basal ice most likely to be influenced by local bed disturbances. The appropriate depth interval is not immediately clear, but previous work and our data offer rough guidance. First, Marshall et al. (2002) showed that length scale discrepancies between driving stress and strain rates can be overcome by averaging both over a length scale consistent with the depth of the strain rate of interest. This analysis treats surface driving stresses, but following Marshall's logic, vertical strain rates from the ice surface down to approximately 100 m above the bed should be representative of general conditions over the borehole triangle.

Secondly, because we compute the bed slope during the winter period, it is a function of the vertical strain rate. The strain rate averaging therefore influences the bed slope. While the exact bed slope cannot be computed from the IceBridge radar profile, the data show that the bed slope is reverse. Because the vertical strain rate becomes increasingly positive at depth, the depth-averaged strain rate transitions from strain thinning (−) to strain thickening (+) when basal ice is incorporated. Consequently, when strain rates below 575 m depth are included in the average, the computed bed slope changes from a 'reverse' trajectory to sloping downward in the direction of ice flow. This is not supported by observation.

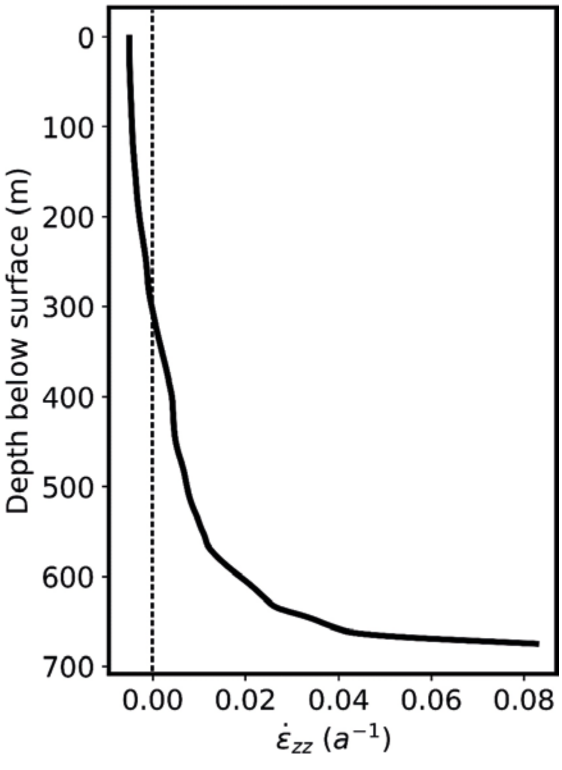

Figure E-5. *Example vertical strain profile on 2016 day of year 125. Dashed vertical line marks* $\dot{\epsilon}_{zz} = 0$.

Based on the above arguments, we have chosen to average the vertical strain from the surface to 550 m depth. The common assumption that surface strain rates are unchanged with depth (e.g. Andrews et al. 2014, Hoffman et al. 2011) is proved false at our study site (Figure E-5). However, our choice of averaging depth introduces substantial uncertainty in the analysis, and this must be kept in mind when interpreting the results. Averaged over this depth interval, the strain rate is near 0 until the velocity accelerations initiate (Figure E-3). Strain thinning ($\overline{\dot{\epsilon}_{zz}}<0$) ensues during most of the early melt season, with a period of strain thickening ($\overline{\dot{\epsilon}_{zz}}>0$) occurring from approximately days 180–200 of year 2016.

E4.2 Basal storage components

To facilitate interpretation, we present the basal storage results as cumulative change in vertical displacement as opposed to rates of change (as in Equation E-1), and describe the results in two phases based on the relevant surface velocity events.

Phase 1: Days of year 120–157

The first phase encompasses the early surface acceleration. During this period, the surface elevation trajectory slowly increases, without a significant perturbation in response to the velocity acceleration event (Figure E-6). The change in surface elevation can described in terms of bed-parallel motion.

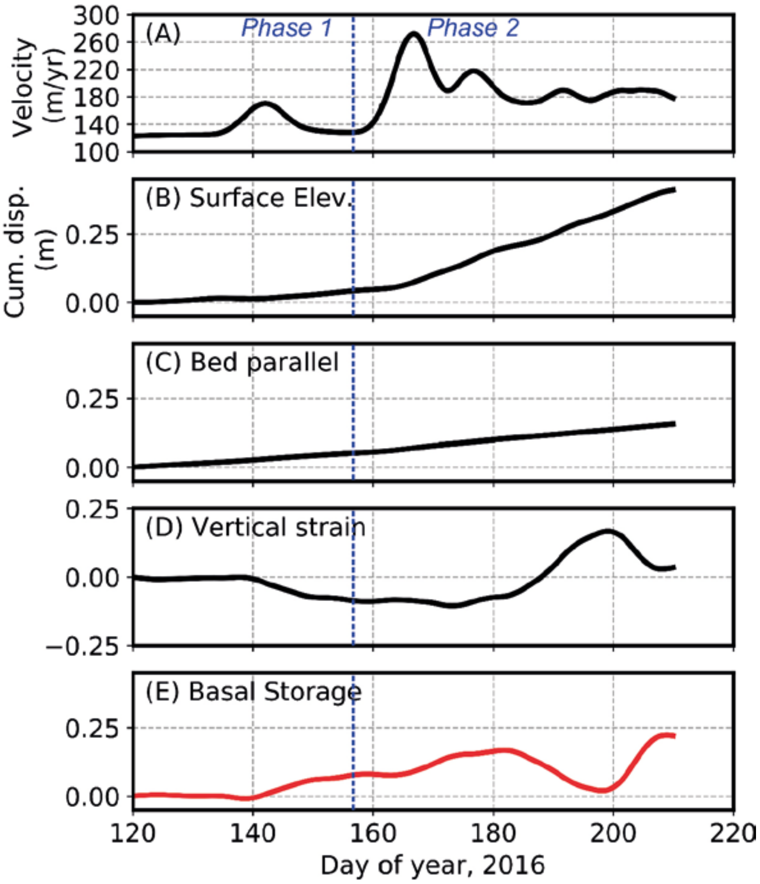

Figure E-6. *Basal storage components computed from Equation 1. Surface velocity is presented in (A) for reference. Surface elevation (B), bed parallel displacement (C), vertical strain displacement (D), and basal storage (E) are all presented as cumulative change from 2016 day of year 120. The vertical axes in panels (B) – (E) span the same displacement (0.5 m). Blue vertical dashed lines reflect transition between Phase 1 and Phase 2.*

Vertical displacement from ice strain becomes negative in response to the surface acceleration. This change in displacement from vertical strain is mirrored by an increase in basal storage of the same magnitude. The similarity of the vertical strain and basal storage curves illustrates the challenges in computing basal storage as the residual of vertical elevation changes arising from other glaciological processes. Moreover, because of the difficulties in quantifying the average vertical strain, it is difficult to confidently interpret this early change in basal storage as real in the absence of any independent indicators (such as change in the trajectory of the surface elevation).

Phase 2: Days of year 157–220

Constraining timing details is obscured by the Gaussian smoothing of the data, but in response to the primary spring acceleration event, the surface elevation trajectory undergoes a large increase which continues until the end of the time series. The surface elevation increases by approximately 0.05 m during the Phase 1, and by 0.35 m during Phase 2 (Figure E-6).

The observed surface change is unaccounted for by vertical elevation changes arising from bed-parallel motion. While the analysis assumes an unchanging bed slope throughout the time series, it is unlikely that a changing bed slope is responsible for the observed change in surface elevation trajectory for two reasons: 1) the timing of this change would have to be incredibly fortuitous, considering the contemporaneous change in surface velocity, 2) the ice traverses approximately 30 meters over the bed during the melt season, but all GPS units, spanning an area of >400 000 m^2 show similar changes in surface elevation. Instead, it most likely that the change in surface elevation trajectory owes to some combination of vertical strain and/or change in basal storage.

The ice flow regime remains strain thinning during the acceleration event. Consequently, the analysis shows that the increase in surface elevation must result from an increase in basal storage. The independent observation of surface trajectory change supports this result, but considering that uncertainty in vertical strain dominates the Phase 1 results, it is difficult to rule out the possibility that vertical strain uncertainty also dominates the result in Phase 2. Transition to a strain thickening regime occurs after the largest acceleration, resulting in a calculated evacuation of basal storage.

An increase in basal storage is calculated at the end of the time series. Evaluation of this result will benefit from the addition of data through the remainder of the melt season to assess, for instance, whether evacuation of the basal storage component occurs at the end of the melt season.

E5 References

Andrews L C, Catania G A, Hoffman M J, Gulley J D, Lüthi M P, Ryser C, Hawley R L, Neumann T A, 2014. Direct observations of evolving subglacial drainage beneath the Greenland ice sheet. Nature 514, 80–83.

Andrews L C, Hoffman M J, Neumann T A, Ginny A, Lüthi M P, Hawley R L, Schild K M, Ryser C, Morriss B F, 2018. Seasonal evolution of the subglacial hydrologic system modified by supraglacial lake drainage in western Greenland. Journal of Geophysical Research: Earth Surface 123, 1479–1496.

Bartholomaus T C, Anderson R S, Anderson S P, 2008. Response of glacier basal motion to transient water storage. Nature Geoscience 1, 33–37.

Bartholomew I, Nienow P, Mair D, Hubbard A, King M A, Sole A, 2010. Seasonal evolution of subglacial drainage and acceleration in a Greenland outlet glacier. Nature Geoscience 3, 408–411.

Bartholomew I, Nienow P, Sole A, Mair D, Cowton T, King M A, 2012. Short-term variability in Greenland Ice Sheet motion forced by time-varying meltwater drainage: Implications for the relationship between subglacial drainage system behavior and ice velocity. Journal of Geophysical Research 117, F03002. doi:10.1029/2011JF002220

Doyle S H, Hubbard A, van de Wal R S W, Box J E, van As D, Scharrer K, Meierbachtol T W, Smeets P C J P, Harper J T, Johansson E, Mottram R H, Mikkelsen A B, Wilhelms F, Patton H, Christoffersen P, Hubbard B, 2015. Amplified melt and flow of the Greenland ice sheet driven by late-summer cyclonic rainfall. Nature Geoscience 8, 647–653.

Harper J T, Humphrey N F, Pfeffer W T, Lazar B, 2007. Two modes of accelerated glacier sliding related to water. Geophysical Research Letters 34. doi:10.1029/2007GL030233

Hoffman M J, Catania G A, Neumann T A, Andrews L C, Rumrill J A, 2011. Links between acceleration, melting, and supraglacial lake drainage of the western Greenland Ice Sheet. Journal of Geophysical Research 116, F04035. doi:10.1029/2010JF001934

Howat I M, Tulaczyk S, Waddington E, Björnsson H, 2008. Dynamic controls on glacier basal motion inferred from surface ice motion. Journal of Geophysical Research: Earth Surface 113, F03015. doi:10.1029/2007JF000925

Hooke R L, Calla P, Holmlund P, Nilsson M, Stroeven A, 1989. A 3 year record of seasonal variations in surface velocity, Storglaciären, Sweden. Journal of Glaciology 35, 235–247.

Iken A, Bindschadler R A, 1986. Combined measurements of subglacial water pressure and surface velocity of Findelengletscher , Switzerland : Conclusions about drainage system and sliding mechanism. Journal of Glaciology 32, 101–119.

Jansson P, 1995. Water pressure and basal sliding on Storglaciären, northern Sweden. Journal of Glaciology 41, 232–240.

Kamb B, Engelhardt H, Fahnestock M, Humphrey N F, Meier M F, Lundstrom S, Stone D, 1994. Mechanical and hydrologic basis for the rapid motion of a large tidewater glacier. 2: Interpretation. Journal of Geophysical Research 99, 231–244.

Lindbäck K, Pettersson R, Hubbard A L, Doyle S H, van As D, Mikkelsen A B, Fitzpatrick A A, 2015. Subglacial water drainage, storage, and piracy beneath the Greenland ice sheet. Geophysical Research Letters 42, 7606–7614.

Mair D W F, Sharp M J, Willis I C, 2002. Evidence for basal cavity opening from analysis of surface uplift during a high-velocity event: Haut Glacier d'Arolla, Switzerland. Journal of Glaciology 48, 208–216.

Marshall H P, Harper J T, Pfeffer W T, Humphrey N F, 2002. Depth-varying constitutive properties observed in an isothermal glacier. Geophysical Research Letters 29, 2146. doi:10.1029/2002GL015412

Meierbachtol T W, Harper J T, Humphrey N F, Wright P J, 2016. Mechanical forcing of water pressure in a hydraulically isolated reach beneath Western Greenland's ablation zone. Annals of Glaciology 57, 62–70.

Schuler T, Fischer U H, Sterr R, Hock R, Gudmundsson H G, 2002. Comparison of modeled water input and measured discharge prior to a release event: Unteraargletscher, Bernese Alps, Switzerland. Nordic Hydrology 33, 27–46.

Sugiyama S, Skvarca P, Naito N, Enomoto H, Tsutaki S, Tone K, Marinsek S, Aniya M, 2011. Ice speed of a calving glacier modulated by small fluctuations in basal water pressure. Nature Geoscience 4, 597–600.

Sundal A V, Shepherd A, Nienow P, Hanna E, Palmer S, Huybrechts P, 2011. Melt-induced speed-up of Greenland ice sheet offset by efficient subglacial drainage. Nature 469, 521–524.

Wright P J, Harper J T, Humphrey N F, Meierbachtol T W, 2016. Measured basal water pressure variability of the western Greenland ice sheet: Implications for hydraulic potential. Journal of Geophysical Research: Earth Surface 121, 1134–1147.

Appendix F

Force balance along Isunnguata Sermia, West Greenland

(Meierbachtol T, Harper J, Johnson J, 2016. Force balance along Isunnguata Sermia, West Greenland. Frontiers In Earth Science 4. doi:10.3389/feart.2016.00087)

F1 Abstract

Ice flows when gravity acts on gradients in surface elevation, producing driving stresses. In the Isunnguata Sermia and Russel Glacier catchments of Western Greenland, a 50 % decline in driving stress along a flow line is juxtaposed with increasing surface flow speed. Here, these circumstances are investigated using modern observational data sources and an analysis of the balance of forces. Stress gradients in the ice mass and basal drag which resist the local driving stress are computed in order to investigate the underlying processes influencing the velocity and stress regimes. Our results show that the largest resistive stress gradients along the flowline result from increasing surface velocity. However, the longitudinal coupling stresses fail to exceed 15 kPa, or 20 % of the local driving stress. Consequently, computed basal drag declines in proportion to the driving stress. In the absence of significant resistive stress gradients, other mechanisms are therefore necessary to explain the observed velocity increase despite declining driving stress. In the study area, the observed velocity – driving stress feature occurs at the long-term mean position of the equilibrium line of surface mass balance. We hypothesise that this position approximates the inland limit where surface meltwater penetrates the bed, and that the increased surface velocity reflects enhanced basal motion associated with seasonal meltwater perturbations.

F2 Introduction

As the Greenland Ice Sheet (GrIS) loses mass at an accelerating rate (Shepherd et al. 2012), understanding the flow dynamics that control mass flux and geometry of the ice sheet has increasingly become a research priority. This has motivated the collection of new high resolution datasets over the last decade of GrIS surface topography (e.g. Helm et al. 2014, Howat et al. 2014), bed geometry (e.g. Bamber et al. 2013), and surface velocity (e.g. Joughin et al. 2010, Rignot and Mouginot 2012). While gravity drives the flow of ice, numerous other factors (e.g. basal topography and substrate, ice temperature, and rheology) also influence the basal sliding and deformational motion of the ice sheet in response to gravitational forcing. These new datasets of the ice sheet's physical domain have allowed the driving stress and velocity fields to be quantified with increasing accuracy, and thus facilitate investigation of additional processes and conditions which influence ice motion.

Establishing those processes driving ice flow through simple comparison of driving stress with surface velocity can be complicated by viscous stresses within the ice column. These stresses resist the transmission of driving stress to the bed by redistributing it to neighboring regions. The magnitude of these internal stresses has been found to be substantial over length scales reaching several ice thicknesses (e.g. Price et al. 2002, van der Veen et al. 2011). Consequently, the stress regime near the ice sheet base, where deformation and sliding are concentrated, can deviate significantly from the driving stress. Where observations are sufficiently resolved, the magnitude of resistive stress gradients can be estimated computationally by a force budget. Given knowledge of ice temperature and geometry, the computed spatial gradients in surface velocity yield column-averaged longitudinal and lateral resistive stresses. Gradients in these stresses determine the fraction of driving stress that is taken up in the ice column, with the remainder being locally transmitted to the ice sheet bed.

The southwest region of the GrIS (Figure F-1) was previously identified as having anomalously low driving stress compared to the bulk of the ice sheet (Bamber and Layberry 2001, Layberry and Bamber 2001) (driving stress calculations are discussed below). Available data at the time of this identification indicated increasing bed elevations and reverse bed slopes towards the ice margin, which were interpreted to be the reason behind an extensive 'ice plain' and lower driving stress in the region (Layberry and Bamber 2001). Low driving stress also extends north to the Isunnguata Sermia and Russel Glacier catchments (boxed area in Figure F-1), but new airborne-based surface and bed topography indicate that increasing bed elevations there are absent (Figures F-2, F-3).

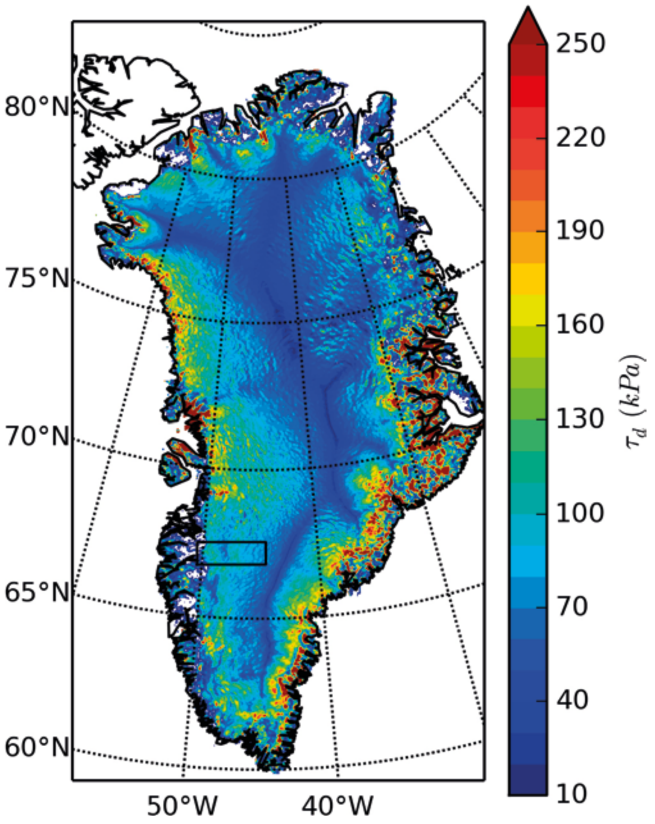

Figure F-1. Driving stress calculated over the GrIS. Surface slopes are calculated over a 4 km length scale as described in the text. Black box outlines study area displayed in Figure F-2.

For the Isunnguata Sermia and Russel Glacier catchments, high-resolution datasets of ice geometry, surface velocity, and borehole measurements of in situ ice sheet temperature (Harrington et al. 2015) are all available. Hence, this uniquely well-characterised region permits a well-constrained investigation of the factors behind a low driving stress and its relation to the observed surface motion. Here, motivated by incomplete explanation of the driving stress anomaly, we investigate the surface velocity profile accompanying the driving stress decline, and evaluate a force balance to assess the role of resistive stress gradients in modulating the transmission of low driving stress to the bed. We conclude by discussing the implications of the observed surface velocity and low driving stress for the deformational and basal sliding components of flow in the study area.

F3 Study area and datasets

The study region in W-SW GrIS includes the Isunnguata Sermia and Russel Glacier catchments (Figure F-2). These land-terminating outlet glaciers have been a focus of field-based research investigating subglacial hydrology (e.g. Chandler et al. 2013, Meierbachtol et al. 2013), lake drainage dynamics (Dow et al. 2015, Doyle et al. 2013), and meltwater influences on ice motion (e.g. Bartholomew et al. 2012, Palmer et al. 2011). The inland extent of the study domain reaches elevations of ~2 300 m, and is selected based on the fidelity of InSAR velocity measurements, which degrade towards the ice sheet interior where control points are either based on balance velocity or are 100s of km away from bedrock reference points (Joughin et al. 2010).

The relatively high density of observations made from remote (e.g. airborne-based radar) and in situ (e.g. borehole measurements) techniques uniquely position the study area for force balance analysis. InSAR-derived surface velocities from Joughin et al. (2010) define motion over the study reach during the winter period between Dec 1, 2008 and Feb 28, 2009, and are provided at 500 m spatial resolution. The digital elevation model (DEM) of bedrock topography by Bamber et al. (2013) is used. This DEM is informed by airborne radar flightlines that were collected at dense spacing (~500 m) through much of our study area as part of the IceBridge mission (Leuschen et al. 2010), and is posted at 1 km resolution.

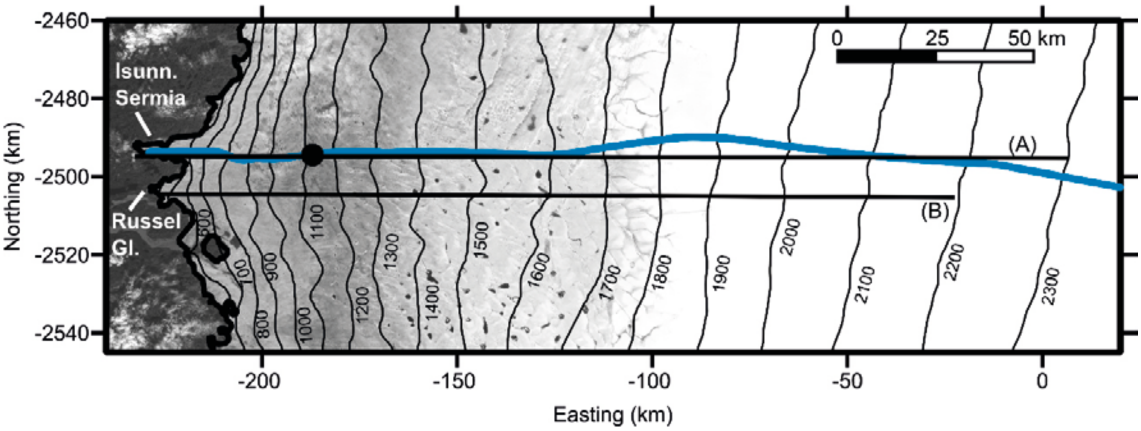

Figure F-2. Study area. Surface elevation contours come from CryoSat-2 (Helm et al. 2014). Blue line locates the flow line used in Figure F-8. Black dot locates the borehole yielding temperature data. Black lines identify the IceBridge transects presented in Figure F-3.

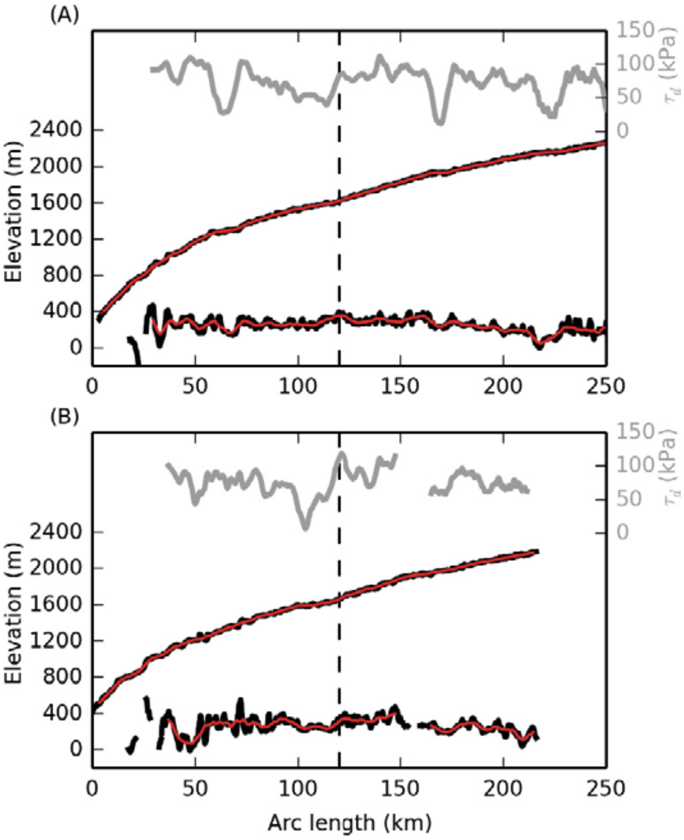

Figure F-3. Surface and bed topography (black), and computed driving stress (gray) along two IceBridge flightlines (Leuschen et al. 2010) which extend through our study area. Red lines represent smoothed topographic profiles used to compute driving stresses. Dashed black line marks the approximate onset of the decline in driving stress referenced throughout the text. Locations of the flightlines are shown in Figure F-2.

We use the CryoSat-2 DEM (Helm et al. 2014) to define the ice sheet surface over the study area. It is posted at 1 km resolution. This surface DEM is advantageous in that it is computed from data collected using a single methodology (satellite radar altimetry) over a relatively short time period (2010–2012). This limits uncertainty arising from stitching together multiple datasets which were collected using different methods and over long time periods (e.g. the GIMP dataset).

Full depth ice temperature has been measured in multiple boreholes drilled in the ablation zone of the study reach (Harrington et al. 2015). In our force balance calculations we use a constant temperature of −10.2 °C, which derives from the vertically averaged temperature measured in the study domains inland-most borehole (Figure F-4), to determine the rate factor (Equation F-9). This borehole is located 45.5 km from the terminus of Isunnguata Sermia (see Figure F-2), where the ice thickness exceeds 800 m, but is still some 50 km down-flow from the driving stress anomaly of interest (see Results). As a result, the temperature value in our force balance calculations may be biased warm over the region of low driving stress (we discuss the implications of this in the Supplementary Material).

F4 Force balance

We implement the force balance technique developed by van der Veen and Whillans (1989a), which recasts the stress balance through the ice column in terms of its resistive and lithostatic components. In the direction of flow (x), gravitational driving stress (τ_d) is resisted by viscous stress gradients associated with longitudinal coupling (τ_l) and lateral shear (τ_t) to yield the resulting friction along the bed (τ_b):

$$\tau_d = \tau_b + \tau_l + \tau_t \qquad \text{(F-1)}$$

The driving stress is calculated as:

$$\tau_d = -\rho_i g H \frac{\partial s}{\partial x}, \qquad \text{(F-2)}$$

where ρ_i is ice density, g is gravitational acceleration, H is ice thickness, and S is the surface elevation. Driving stress values are positive in the downstream direction. Viscous stresses acting in the same direction are also denoted positive when we assess the fraction of driving stress taken up by internal ice dynamics.

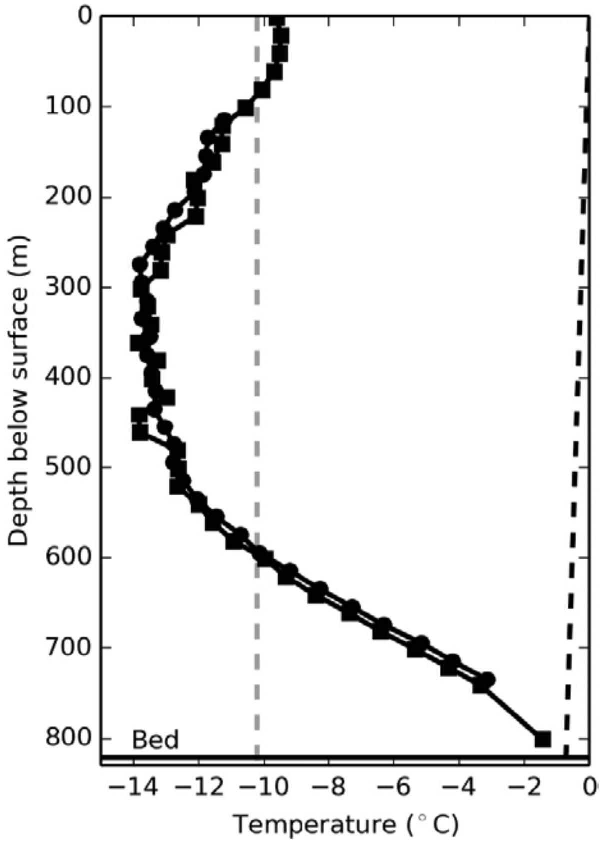

Figure F-4. Temperature profiles in two boreholes, <20 m apart, drilled to the ice sheet bed (Harrington et al. 2015). Dashed black line represents the pressure melting temperature, calculated using a Clausius Clapeyron slope of 8.7×10^{-4} °C m^{-1} for ice. Dashed grey line shows the average temperature of −10.2 °C, calculated from the two profiles.

Calculation of the resistive terms τ_l and τ_t requires knowledge of ice temperature and stresses through the ice column that are poorly constrained. Where basal sliding constitutes a substantial fraction of observed surface motion, strain rates at depth are reasonably reflected by surface values, and the assumption of depth-invariance may be invoked (O'Neel et al. 2005, Price et al. 2002, van der Veen et al. 2011). Modeling and observation suggest that this assumption is satisfied in our study area, particularly where velocity errors are small (see Supplementary Material). We therefore adopt the assumption of depth-invariance in this study. In this isothermal block model, viscous terms are written as:

$$\tau_l = -\frac{\partial}{\partial x}\left(H\bar{R}_{xx}\right) \qquad \text{(F-3)}$$

and

$$\tau_l = -\frac{\partial}{\partial y}\left(H\bar{R}_{xy}\right) \qquad \text{(F-4)}$$

where y is the direction transverse to flow. Variables $\overline{R}_{xx}$ and $\overline{R}_{xy}$ represent the vertically averaged horizontal resistive stresses, and are expressed as:

$$\bar{R}_{xx} = B\dot{\varepsilon}_e^{\frac{1}{n}-1}\left(2\dot{\varepsilon}_{xx} + \dot{\varepsilon}_{yy}\right) \qquad \text{(F-5)}$$

and:

$$\bar{R}_{xy} = B\dot{\varepsilon}_e^{\frac{1}{n}-1}\dot{\varepsilon}_{xy} \qquad \text{(F-6)}$$

where n is Glen's exponent (assumed to equal 3) and strain rates are calculated from surface velocity gradients:

$$\dot{\varepsilon}_{ij} = \frac{1}{2}\left(\frac{\partial U_i}{\partial x_j} + \frac{\partial U_j}{\partial x_i}\right) \quad i, j = x, y \qquad \text{(F-7)}$$

The effective strain rate in Eqs. 5–6 is given by:

$$\dot{\varepsilon}_e = \left[\left(\dot{\varepsilon}_{xx}^2 + \dot{\varepsilon}_{yy}^2 + \dot{\varepsilon}_{zz}^2\right) + 2\dot{\varepsilon}_{xy}^2\right]^{1/2} \qquad \text{(F-8)}$$

which computes the vertical strain rate under the continuity condition $\dot{\varepsilon}_{xx} + \dot{\varepsilon}_{yy} + \dot{\varepsilon}_{zz} = 0$. Vertical shear is omitted in Equation F-8 following the depth-invariance assumption. Vertical resistive stresses in Equation F-5 are omitted under the assumption that bridging effects are negligible over the length scales considered (~km). Vertical resistive stresses have been found to alter basal stress to a minor degree (van der Veen and Whillans 1989b), particularly over grounded ice (Morlighem et al. 2010), supporting this omission. Horizontal resistive stresses in the ice are a function of the rate factor (B), which is temperature-dependent and follows the Arrhenius relation:

$$B = \left[A_0 \mathrm{e}^{(-Q/RT)}\right]^{-1/n} \qquad \text{(F-9)}$$

where A_0 is an Arrhenius constant, Q is the activation energy for creep, $R = 8.314$ J mol^{-1} K^{-1} is the universal gas constant, and T is the vertically averaged ice temperature.

F4.1 Computational methods and selection of smoothing kernel

Input datasets must share a consistent spatial grid for force balance calculations. To achieve this, the velocity field is resampled at 1 km spacing to match the coarser DEMs. The bedrock DEM is projected to the same spatial projection as the velocity and surface elevation products, and linearly interpolated so that all datasets are populated along the same spatial coordinates. The bed DEM is then subtracted from the surface DEM to yield ice thickness. The force balance must be computed over a coarser resolution than 1 km in order to reduce the propagation of input data uncertainties. To achieve this, each dataset is smoothed using a two dimensional triangular smoothing window of size 4 × 4 km, and resampled at 4 km spacing to generate final datasets for the force balance calculations. The resulting ice thickness, surface slope, and surface speed are displayed in Figure F-5.

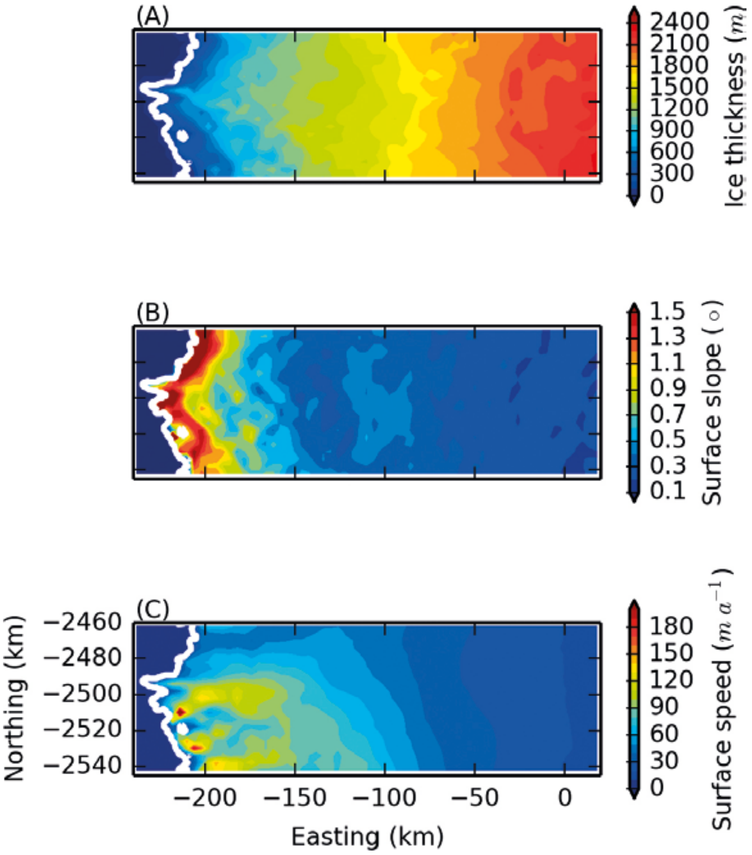

Figure F-5. *Ice thickness (A), surface slope (B), and surface speed (C) fields used for the force balance calculations after pre-processing as described in the text.*

Each computed force balance term has a corresponding uncertainty that is a function of the input dataset uncertainty and length scale over which the spatial derivatives are computed (van der Veen 2013). We use this error to inform the length scale of the smoothing window. Force balance components are computed using centered differences to calculate spatial derivatives over the resampled and smoothed data. We calculate uncertainty propagation following methods reported by Taylor (1997). Individual force balance and error components are computed as vectors on the x- and y-axes defined by the spatial projection, and then rotated to the local flow direction (which closely follows the projection x-axis) following established methods (van der Veen 2013). Sensitivity testing indicates that the uncertainty in computed basal drag decreases to <20 % of the averaged basal drag values when the gridded data are resampled over 4 km (Figure F-6). Input data are thus resampled over this length scale.

F5 Results

Results from the force balance analysis over the study area are displayed in Figure F-7. Figure F-8 presents the force balance components along the flowline shown in Figure F-2. This flowline is chosen because it terminates in the Isunnguata Sermia outlet. We have no reason to assume it is less representative than other flowlines through the study area.

F5.1 Driving stress and surface velocity

With the exception of diminishing driving stress from thin ice near the margin, calculated driving stress across the study area is between ~50 and 120 kPa (Figure F-7A). Along the flowline from the interior towards the ice margin, the driving stress shows an increasing trend from 75 kPa at 250 km to 100 kPa at 115 km (Figure F-8b). Over the subsequent 20 km, driving stress falls by 50 % from 100 kPa to a minimum of 50 kPa at 95 km. Away from the ice sheet edge, this marks the lowest driving stress along the entire flowline. Following the driving stress minimum, values slowly increase to a maximum of 140 kPa at 15 km before dropping near the ice sheet margin.

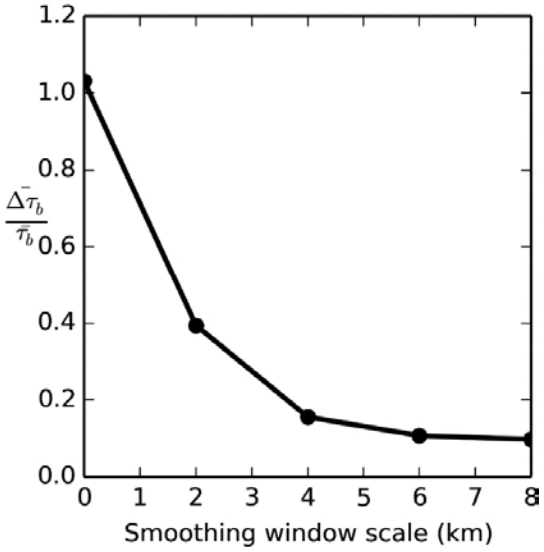

Figure F-6. *Mean basal drag uncertainty over the study domain ($\Delta\bar{\tau}_b$) displayed as a fraction of the mean computed basal drag ($\bar{\tau}_b$) for different smoothing window scales.*

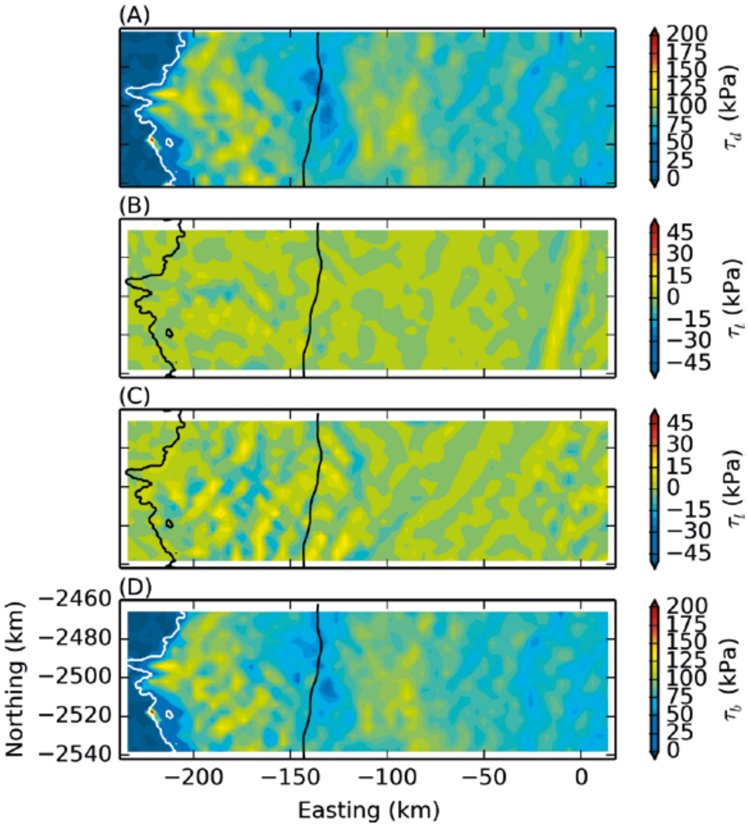

Figure F-7. *Force balance calculation results across the study domain showing driving stress (A), lateral drag (B), longitudinal stress gradient (C), and the basal drag residual (D). Black line shows the approximate long term ELA (1 553 m elevation) for reference. Note the difference in scale between resistive terms (B and C), and driving stress (A) and basal shear (D).*

Surface flow speed generally increases from the interior towards the ice margin (Figures F-5c, F-8a). A brief plateau in speed at 110 km along the flowline is followed by a sharp increase to a peak value of 105 m a^{-1} ~50 km from the margin. The onset of the surface speed-up is coincident with declining driving stress and, with the exception of the ice sheet margin, the lowest driving stress values of the profile at 90–100 km align with the greatest increase in surface speed (Figure F-8).

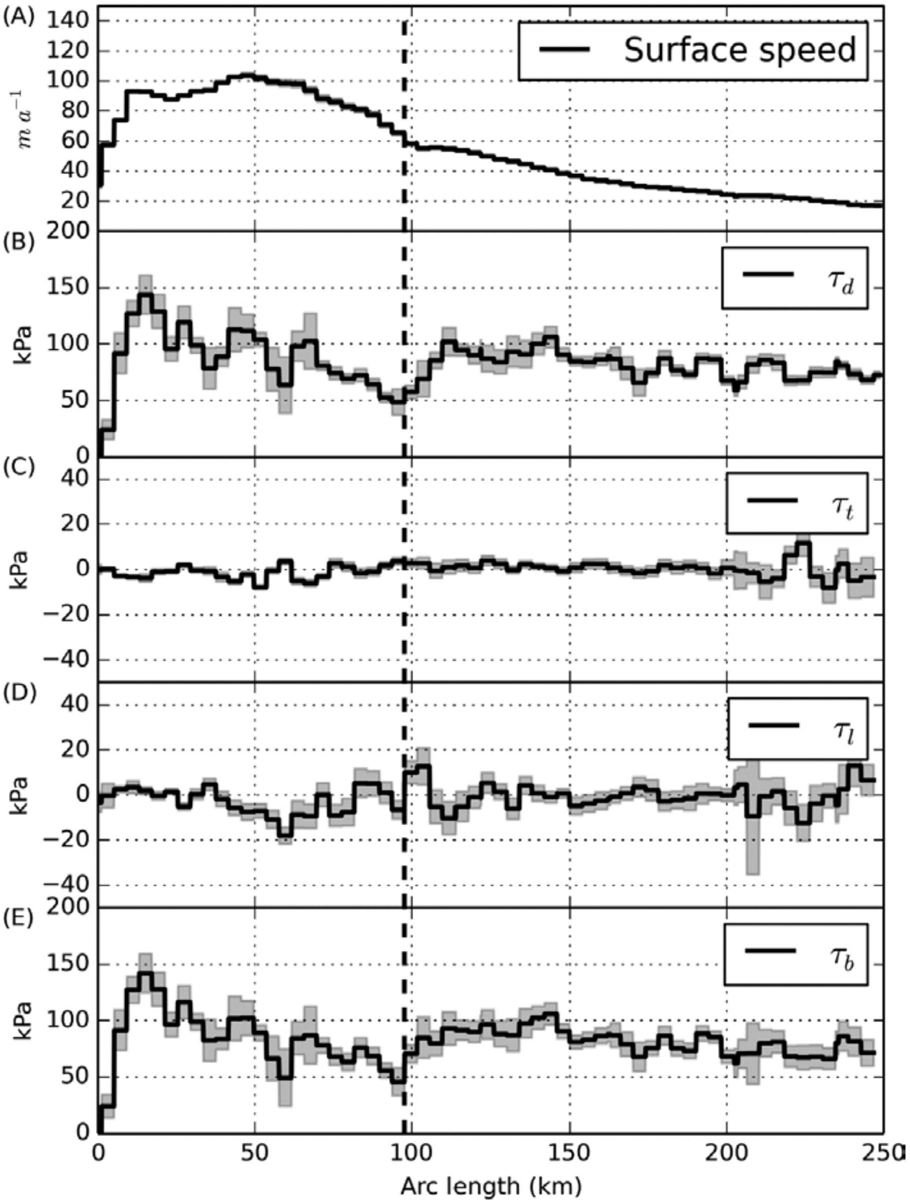

Figure F-8. *Force balance calculation results along the flowline presenting driving stress (B), lateral drag (C), longitudinal stress gradient (D), and basal drag (E). Surface speed is presented in (A) for reference. Shaded regions represent the computed uncertainty for each force balance component. Dashed black line locates the approximate long term ELA (1 553 m elevation) for reference.*

F5.2 Force balance

Lateral drag over the study area is small, and does not exceed 15 kPa in magnitude (Figure F-7b). Gradients in longitudinal stresses (τ_l) are larger in magnitude than lateral drag. Fluctuations in τ_l are small in the interior, and increase in magnitude towards the ice sheet margin, locally reaching values between −25 and 25 kPa (Figure F-7c).

Along the flowline, the largest positive τ_l are coincident with the acceleration in surface speed at 100 km. Here, τ_l reaches values that are ~20 % of the local driving stress, or 15 kPa (Figure F-8d). Positive longitudinal stress gradients subsequently decline towards the ice margin, trending to negative values that approach −20 kPa at 60 km. Negative τ_l acting against the direction of driving stress correspond to a change in curvature of the velocity profile from concave to convex.

Computed with our chosen averaging length scale, resistive stress components are no greater than ~20 % of the corresponding driving stress anywhere on the flowline. Consequently, the deviations between basal drag and driving stress remain small (e.g. Figures F-8b, F-8e). Similar to the driving stress decline along the flowline, basal drag decreases by nearly 50 % from 82 kPa to 44 kPa between 103 and 95 km. Surface speed increases from 54 to 65 m a^{-1} over the same distance.

F6 Discussion

F6.1 Force balance and surface velocity

The main conclusion from the force balance calculations is that basal traction balances most of the driving stress, including in the anomalous region where declining driving stress and increasing surface speed coincide. In ice stream settings, coincidence of declining driving stress and increasing surface velocity has been used to define the onset of streaming flow, where the bed is unable to support shear stress (e.g. Alley and Whillans 1991, Bindschadler et al. 2001). These conditions promote increased sliding that draws down the ice surface, reduces surface slopes, and lowers driving stresses. The low resistive stress gradients we compute suggest that this behavior is not unique to marine terminating ice streams, but also occurs in our study area which terminates on land.

This interpretation, however, hinges on the assumption that ice sheet velocity and geometry are in balance over similar time scales. The datasets used in the force balance analysis span a period of a couple of years (assumptions and limitations of the force balance results are detailed in the Supplemental Material). While the datasets are self-consistent over this period, each likely reflects conditions that are unchanging over a different time scale. Observations show that the study area is not undergoing rapid thinning (Helm et al. 2014, Pritchard et al. 2009), suggesting that the surface geometry has been in a relatively steady state over perhaps many decades. However, while the velocity observations in the study area are consistent over multiple years, large changes in ice motion have been observed elsewhere on the ice sheet over time periods much shorter than the decadal scale that is likely represented by the surface geometry (Joughin et al. 2010, Rignot and Kanagaratnam 2006). While these changes are generally limited to marine terminating regions, whether the observations in our study area can be interpreted to reflect ice dynamics over a longer time scale that is consistent with the surface geometry remains questionable.

This caveat complicates the interpretation of relationships between driving stress and velocity not just at our study area, but also in any study assimilating ice geometry and velocity into a physical modeling framework. Nevertheless, the unexpected finding that a substantial decline in driving stress is coincident with increasing surface velocity over such a large region (~20 km wide) begs explanation. We next explore processes that could explain this observation, bearing in mind the above caveat.

F6.2 Enhanced internal deformation

Both direct observations and modeling indicate that in the study areas ablation zone the contribution to ice flow from internal deformation is secondary (see Supplementary Material). Nevertheless, in an effort to explore all possible scenarios, we assess whether enhanced internal deformation could accommodate the observed speed-up, despite declining driving stress. A zeroth order assessment can be achieved by assuming that deformation occurs by laminar flow, and estimating the minimum degree of softening necessary for ice deformation to maintain a constant velocity under reduced driving stress. Integrating the deformation rate through an ice column of thickness H yields the formula for surface velocity (U):

$$U = \frac{2EA}{n+1} H \tau_d^{\,n} \qquad \text{(F-10)}$$

where E is an ill-constrained enhancement factor accommodating rheological changes and A is related to Equation F-9 by $A = B^{-n}$. In the absence of thickness changes, Equation F-10 requires that the product of rheological factors E and A increase > 6 fold to accommodate the documented drop in driving stress.

Achieving the required six-fold softening through warmer ice alone requires temperature changes that are unsupported by data. For instance, ice at −15 °C must warm by 11 °C in order to achieve the required softening, but this is contrary to borehole observations which show temperatures are still much colder lower in the ablation zone (Harrington et al. 2015). A more modest temperature increase (e.g. 5 °C) would require doubling of the enhancement factor. Liquid water-induced softening through growth of a temperate basal layer is not physically viable, considering that a thick temperate layer is absent in the measured profile 50 km from the observed low driving stress (Harrington et al. 2015). Other factors influencing ice rheology (e.g. related to impurity content or crystal orientation) can cause *E* to change by a factor of two or more with ice depth (e.g. Lüthi et al. 2002, Shoji and Langway 1984), but changes of a similar magnitude over the necessary horizontal length scales (~10 km) lack observational or conceptual basis.

F6.3 Enhanced basal slip

If enhanced deformation is not a viable explanation, then the observed acceleration must result from enhanced basal slip. Knowledge of the thermal state of the ice-bed interface far from the ice sheet margin is lacking. However, there is broad agreement by numerical models that temperate basal conditions extend well inland of the ELA at our study area (Meierbachtol et al. 2015, Poinar et al. 2015, Seroussi et al. 2013), despite evidence of low geothermal heat flux (Meierbachtol et al. 2015). Consequently, it is unlikely that increased basal slip results from a frozen to temperate transition.

Assuming that temperate basal conditions extend above the ELA at our study region, the increased slip may result from a reduction in bed strength. If the basal substrate is composed of subglacial till, weakening must occur through changes in pore pressure and water saturation (Cuffey and Patterson 2010). Alternatively, if the bed is predominantly hard bedrock, a redistribution of stresses to smaller contact patches would increase basal motion. In either scenario, a change in the amount or distribution of water at the bed is the most likely forcing mechanism.

Routing of surface water to the bed is well established lower in the ablation zone, but its inland extent remains unclear. Surface crevasses provide one mechanism facilitating meltwater transport. It has been suggested that conditions promoting crevasse formation are limited to below ~1 400 m (Clason et al. 2015) to 1 600 m elevation (Poinar et al. 2015) in the study area. Meltwater-induced seasonal variations in ice motion have been observed to elevations reaching ~1 500–1 600 m (Bartholomew et al. 2011, Palmer et al. 2011). Given this evidence, the long term measured ELA of 1 553 m (van de Wal et al. 2012) appears to serve as a plausible limit of the inland extent of seasonal surface meltwater routing to the bed. Its location also aligns with the greatest rate of velocity change along the flowline (Figure F-8), suggesting that the increase in velocity is related to the introduction of surface meltwater to the bed. If true, the fact that the velocity observations were collected during the winter period implies that the enhanced slip persists beyond the melt season.

Although the long term ELA aligns closely with accelerating velocity and declining driving stress, it has exhibited large variability over the past >20 years. Observational records along the nearby K-transect have shown that the annual ELA has varied from ~1 400 to 1 800 m (van de Wal et al. 2012). If the surface velocity and the ice sheet geometry are in a state of balance and reflect steady state flow dynamics over a decadal time scale across the study area, this implies that increased rates of sliding are sufficiently insensitive to seasonal variations in meltwater input so as to produce the observed ice geometry. Exactly why this is so is an intriguing question of basal hydrology beyond the scope of this paper. However, we note several factors which are perhaps relevant. First, owing to long travel paths (>100 km), and thick ice facilitating creep closure, the basal drainage system likely exhibits a high degree of isolation this far from the ice margin. Second, while the hydraulic potential field does not indicate a closed basin facilitating long term melt storage (see Supplementary Figure F-S2), the computed hydraulic gradient driving water flow is small due to the low surface slope. Coincident with the reduction in driving stress along the flowline, the hydraulic gradient declines in magnitude from nearly 80 Pa m^{-1} to <40 Pa m^{-1}. And third, the integration of basally generated melt from upstream temperate bed regions provides a continued source of basal water that introduces a buffering capacity against interannual variations in surface meltwater flux. These three factors may underpin the insensitivity of basal sliding to seasonal variations in meltwater input by modulating water flow variability at the bed.

F7 Conclusions

Available datasets of ice geometry and surface speed indicate an unexpected relationship between gravitational driving stress and ice speed in a land terminating region of the western GrIS. Nearly 100 km from the ice sheet margin, driving stress declines by 50 % over 20 km. This decline is colocated with an increase in surface speed that is the largest observed along a flowline through the well-studied Isunnguata Sermia drainage catchment. This finding shows that such behavior is not unique to ice stream onset in marine-terminating settings. Through force balance calculations, the effects of resistive stress gradients in modulating driving stress transmission to the bed are assessed. Lateral drag is found to be negligible over this interior region of the ice sheet. Longitudinal stress gradients locally reach 20 % of the driving stress, but the declining driving stress is largely taken up by basal drag.

The surface speed for a given gravitational driving stress is a sensitive function of the properties of the ice and processes governing ice flow. At our study area, we find that possible explanatory mechanisms for increased surface motion despite low driving stress are limited to those associated with enhanced basal sliding. We hypothesise that this reflects a change in basal processes associated with the configuration and volume of water at the bed, rather than a transition from frozen to temperate basal conditions. This is supported by the colocation of the surface speed-up with the long term ELA in the study area, below which seasonal routing of surface meltwater to the ice sheet bed is likely.

The study area is defined by high ablation rates and low accumulation, owing to the blocking of southwesterly atmospheric moisture flow from the nearby Sukkertoppen ice cap (Ohmura and Reeh 1991), which combine to yield the highest estimated ELA on the ice sheet (e.g. Reeh 1991). At this elevation the ice is relatively thick and flat, making the driving stress sensitive to flattening from our hypothesised weakening of the bed. In this way, the interplay of surface mass balance and ice flow processes can generate unique driving stress and velocity characteristics in this heavily studied region.

F8 Conflict of interest

The authors declare that the research was conducted in the absence of any commercial or financial relationships that could be construed as a potential conflict of interest.

F9 Author contributions

TM developed the project and performed all analysis and calculations. JH and JJ guided project development through collaborative discussions. All authors contributed to the writing of the manuscript.

F10 Funding

This work is funded by SKB, NWMO, Posiva Oy, NAGRA, and NSF (PLR-ANS grants #1203418 and #0909495, PLR grant #1543533).

F11 Acknowledgments

We thank the scientific editor, F. Ng, and S. Adhikari and an anonymous reviewer for comments which substantially improved the manuscript.

F12 References

Alley R B, Whillans I M, 1991. Changes in the West Antarctic ice sheet. Science 254, 959–963.

Bamber J L, Griggs J A, Hurkmans R T W L, Dowdeswell J A, Gogineni S P, Howat I, Mouginot J, Paden J, Palmer S, Rignot E, Steinhage D, 2013. A new bed elevation dataset for Greenland. The Cryosphere 7, 499–510.

Bamber J L, Layberry R L, 2001. A new ice thickness and bed data set for the Greenland ice sheet 1. Measurement, data reduction, and errors. Journal of Geophysical Research 106, 33773–33780.

Bartholomew I D, Nienow P, Sole A, Mair D, Cowton T, King M A, Palmer S, 2011. Seasonal variations in Greenland Ice Sheet motion: Inland extent and behaviour at higher elevations. Earth and Planetary Science Letters 307, 271–278.

Bartholomew I, Nienow P, Sole A, Mair D, Cowton T, King M A, 2012. Short-term variability in Greenland Ice Sheet motion forced by time-varying meltwater drainage: Implications for the relationship between subglacial drainage system behavior and ice velocity. Journal of Geophysical Research 117, F03002. doi:10.1029/2011JF002220

Bindschadler R A, Bamber J L, Anandakrishnan S, 2001. Onset of streaming flow in the Siple Coast Region, West Antarctica. The West Antarctic Ice Sheet: Behavior And Environment 77, 123–136.

Chandler D M, Wadham J L, Lis G P, Cowton T, Sole A, Bartholomew I, Telling J, Nienow P, Bagshaw E B, Mair D, Vinen S, Hubbard A, 2013. Evolution of the subglacial drainage system beneath the Greenland Ice Sheet revealed by tracers. Nature Geoscience 6, 195–198.

Clason C C, Mair D W F, Nienow P W, Bartholomew I D, Sole A, Palmer S, Schwanghart W, 2015. Modelling the transfer of supraglacial meltwater to the bed of Leverett Glacier, Southwest Greenland. The Cryosphere 9, 123–138.

Cuffey K M, Patterson W S B, 2010. The physics of glaciers. 4th ed. Oxford: Elsevier.

Dow C F, Kulessa B, Rutt I C, Tsai V C, Pimentel S, Doyle S H, Van As D, Lindbäck K, Pettersson R, Jones G A, Hubbard A, 2015. Modeling of subglacial hydrological development following rapid supraglacial lake drainage. Journal of Geophysical Research: Earth Surface 120, 1127–1147.

Doyle S H, Hubbard A L, Dow C F, Jones G A, Fitzpatrick A, Gusmeroli A, Kulessa B, Lindbäck K, Pettersson R, Box J E, 2013. Ice tectonic deformation during the rapid in situ drainage of a supraglacial lake on the Greenland Ice Sheet. The Cryosphere 7, 129–140.

Harrington J A, Humphrey N F, Harper J T, 2015. Temperature distribution and thermal anomalies along a flowline of the Greenland Ice Sheet. Annals of Glaciology 56, 98–104.

Helm V, Humbert A, Miller H, 2014. Elevation and elevation change of Greenland and Antarctica derived from CryoSat-2. The Cryosphere 8, 1539–1559.

Howat I M, Negrete A, Smith B E, 2014. The Greenland Ice Mapping Project (GIMP) land classification and surface elevation data sets. The Cryosphere 8, 1509–1518.

Joughin I, Smith B E, Howat I M, Scambos T, Moon T, 2010. Greenland flow variability from ice-sheet-wide velocity mapping. Journal of Glaciology 56, 415–430.

Layberry R L, Bamber J L, 2001. A new ice thickness and bed data set for the Greenland ice sheet 2. Relationship between dynamics and basal topography. Journal of Geophysical Research 106, 33781–33788.

Leuschen C, Gogineni P, Rodriguez-Morales F, Paden J, Allen C, 2010. IceBridge MCoRDS L2 Ice Thickness, Version 1. Boulder, CO USA: NASA DAAC: NASA DAAC at National Snow and Ice Data Center: NASA National Snow and Ice Data Center Distributed Active Archive Center. doi:http://dx.doi.org/10.5067/GDQ0CUCVTE2Q

Lüthi M, Funk M, Iken A, Gogineni S, Truffer M, 2002. Mechanisms of fast flow in Jakobshavn Isbrae , West Greenland : Part III. Measurements of ice deformation , temperature and cross-borehole conductivity in boreholes to the bedrock. Journal of Glaciology 48, 369–385.

Meierbachtol T, Harper J, Humphrey N, 2013. Basal drainage system response to increasing surface melt on the Greenland ice sheet. Science 341, 777–779.

Meierbachtol T W, Harper J T, Johnson J V, Humphrey N F, Brinkerhoff D J, 2015. Thermal boundary conditions on western Greenland: Observational constraints and impacts on the modeled thermomechanical state. Journal of Geophysical Research: Earth Surface 120, 623–636.

Morlighem M, Rignot E, Seroussi H, Larour E, Ben Dhia H, Aubry D, 2010. Spatial patterns of basal drag inferred using control methods from a full-Stokes and simpler models for Pine Island Glacier, West Antarctica. Geophysical Research Letters 37, 1–6. doi:10.1029/2010GL043853

O'Neel S, Pfeffer W T, Krimmel R, Meier M, 2005. Evolving force balance at Columbia Glacier, Alaska, during its rapid retreat. Journal of Geophysical Research 110, F03012. doi:10.1029/2005JF000292

Ohmura A, Reeh N, 1991. New precipitation and accumulation maps for Greenland. Journal of Glaciology, 37, 140–148.

Palmer S, Shepherd A, Nienow P, Joughin I, 2011. Seasonal speedup of the Greenland Ice Sheet linked to routing of surface water. Earth and Planetary Science Letters 302, 423–428.

Poinar K, Joughin I, Das S B, Behn M D, Lenaerts J T M, Broeke M R, 2015. Limits to future expansion of surface-melt-enhanced ice flow into the interior of western Greenland. Geophysical Research Letters 42, 1800–1807.

Price S F, Bindschadler R A, Hulbe C L, Blankenship D D, 2002. Force balance along an inland tributary and onset to Ice Stream D, West Antarctica. Journal of Glaciology 48, 20–30.

Pritchard H D, Arthern R J, Vaughan D G, Edwards L A, 2009. Extensive dynamic thinning on the margins of the Greenland and Antarctic ice sheets. Nature 461, 971–975.

Reeh N, 1991. Parameterization of melt rate and surface temperature on the Greenland lce Sheet. Polarforschung 5913, 113–128.

Rignot E, Kanagaratnam P, 2006. Changes in the velocity structure of the Greenland Ice Sheet. Science 311, 986–990.

Rignot E, Mouginot J, 2012. Ice flow in Greenland for the International Polar Year 2008–2009. Geophysical Research Letters 39, 1–7. doi:10.1029/2012GL051634

Seroussi H, Morlighem M, Rignot E, Khazendar a., Larour E, Mouginot J, 2013. Dependence of century-scale projections of the Greenland ice sheet on its thermal regime. Journal of Glaciology 59, 1024–1034.

Shepherd A, Ivins E R, A G, Barletta V R, Bentley M J, Bettadpur S, Briggs K H, Bromwich D H, Forsberg R, Galin N, Horwath M, Jacobs S, Joughin I, King M A, Lenaerts J T M, Li J, Ligtenberg S R M, Luckman A, Luthcke S B, McMillan M, Meister R, Milne G, Mouginot J, Muir A, Nicolas J P, Paden J, Payne A J, Pritchard H, Rignot E, Rott H, Sorensen L S, Scambos T A, Scheuchl B, Schrama E J O, Smith B, Sundal A V., van Angelen J H, van de Berg W J, van den Broeke M R, Vaughan D G, Velicogna I, Wahr J, Whitehouse P L, Wingham D J, Yi D, Young D, Zwally H J, 2012. A reconciled estimate of ice-sheet mass balance. Science 338, 1183–1189.

Shoji H, Langway Jr. C C, 1984. Flow behavior of basal ice as related to modeling considerations. Annals of Glaciology 5, 141–148.

Taylor J R, 1997. An introduction to error analysis. 2nd ed. Mill Valley, CA: University Science Books.

van de Wal R S W, Boot W, Smeets C J P P, Snellen H, van den Broeke M R, Oerlemans J, 2012. Twenty-one years of mass balance observations along the K-transect, West Greenland. Earth System Science Data 4, 31–35.

van der Veen C J, 2013. Fundamentals of glacier dynamics. 2nd ed. Boca Raton, FL: CRC Press.

van der Veen C J, Plummer J C, Stearns L A, 2011. Controls on the recent speed-up of Jakobshavn Isbræ , West Greenland. Journal of Glaciology 57, 770–782.

van der Veen C J, Whillans I M, 1989a. Force budget: I. theory and numerical methods. Journal of Glaciology 35, 53–60.

van der Veen C J, Whillans I M, 1989b. Force Budget: II. Application to Two-Dimensional Flow along Byrd Station Strain Network, Antarctica. Journal of Glaciology 35, 61–67.

F13 Supplementary material

F13.1 Assumption of depth invariance

Resistive stress components in the force balance are computed under the assumption that surface strain rates and a vertically averaged temperature are reasonable approximations of conditions through the ice column. The assumption is manifested in all terms in the resistive stress calculations (Equations F-5 and F-6 in the manuscript): ice viscosity is assumed to represent a vertical average with no influence from vertical shearing within the ice column, and horizontal strain rates are assumed unchanged with depth.

The assumption of depth-invariance is largely supported through the study area from available observation and numerical simulations. In situ measurements of ice deformation in boreholes drilled in the ablation zone by Ryser et al. (2014) indicate that surface motion is controlled predominantly by basal sliding during both summer and winter months in the Pakitsoq region, north of our study area in Western Greenland. There are no a priori reasons that the ablation zone in our study area would exhibit different behaviour.

Extending inland from the ice sheet margin, above the equilibrium line, simulations using a higher-order, thermo-mechanically coupled ice sheet model indicate that observed surface velocities can only be reproduced with ice dynamics driven predominantly by basal sliding (Meierbachtol et al. 2015). Calculation of the fraction of surface velocity accommodated by basal sliding under simulation 'E-FULL' (see Meierbachtol et al. 2015), shows that modeled sliding velocities exceed 90 % of surface observations beyond the ELA, and the majority of surface motion is composed of basal sliding nearly everywhere in the ablation zone (Figure F-S1). Deep in the ice sheet interior, ice deformation accommodates the majority of surface motion, however this has little bearing on the presented force balance results because: 1) the areas of interest in the manuscript are in regions shown to be dominated by sliding, and 2) surface velocity observations lose fidelity in the ice sheet interior, (see Section F13.2). Simulation results from Meierbachtol et al. (2015) have no uncertainty propagation, which is necessary for interpretation of force budget components. Consequently, we do not compute the budget of forces using simulated ice velocities through the ice column, and instead use the simulation as a guide for supporting depth-averaged assumption.

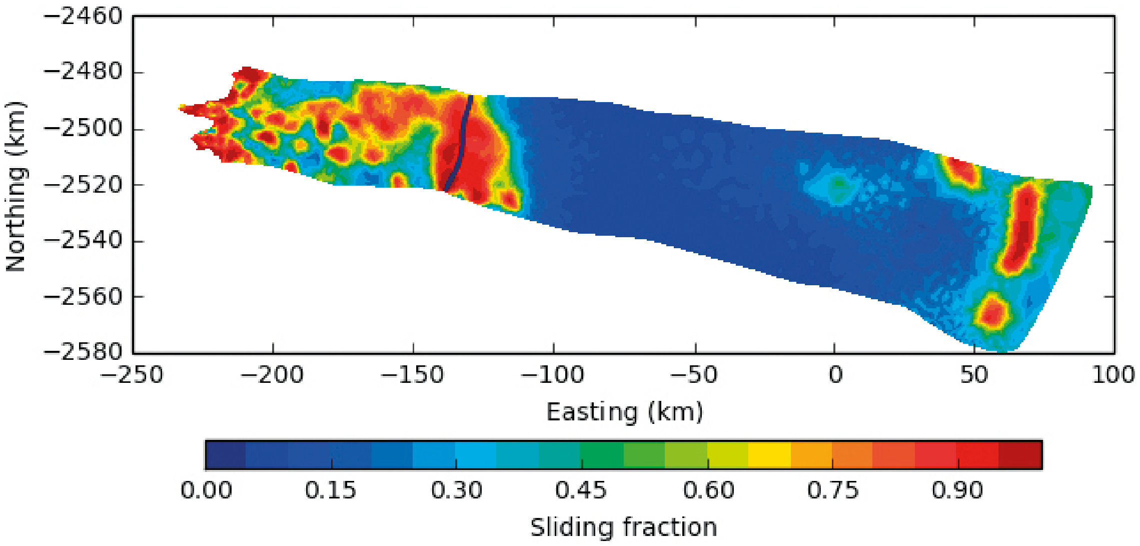

Figure F-S1. *Fraction of modeled surface velocity taken up by basal sliding in model run 'E-FULL' by Meierbachtol et al. (2015). Black line shows the long term ELA (1 553 m elevation) for reference.*

F13.2 Limitations of the force balance

Assessment of the extent to which viscous stress gradients modulate the calculated driving stress reduction is the primary objective of the force balance analysis and must consider limitations of the data and technique. Low driving stress was previously reported as anomalous compared to the general ice sheet profile by Layberry and Bamber (2001), and is corroborated here with updated topographic datasets. Because its presence is confirmed by surface and bed elevation measurements made by Operation IceBridge (Leuschen et al. 2010) along flightlines through the study domain (Figure F-3 in the manuscript), we rule out the possibility that reduced driving stress is an artifact of DEM construction.

Velocity uncertainty increases far from the ice sheet margin. The use of balance and measured velocity control points in the ice sheet interior and other artifacts, such as ionospheric variability, contribute to velocity uncertainty (Joughin et al. 2010). The impacts of such effects are clearly visible in the apparent 'streaking' exhibited by lateral shear gradients near the inland boundary of the model domain (Figure F-7b). Despite these limitations, the spatial velocity structure through the majority of the domain is consistent over multiple years of measurement, and GPS measurements of surface motion inland of anomalous driving stresses at 1 840 m elevation (Doyle et al. 2014) are consistent with the gridded velocity applied here. These observations support the fidelity of InSAR velocity through the region of interest.

The observation-based temperature that is prescribed through the study domain is likely to reflect a warm end-member case in the region of low driving stress because of the observation's proximity to the ice sheet margin. Resistive stresses are linearly proportional to the ice viscosity (defined as the product of the rate factor and effective strain rate terms in Equations 5 and 6), with the effect that softer ice may modulate resistive stress gradients. Doubling the magnitude of τ_l and τ_t in the force balance requires uniform cooling by more than 8 °C, but does not influence the spatial pattern of the resistive terms. Because the spatial scale of the driving stress anomaly is larger than the more localised stress gradient terms, the broad pattern of basal drag largely remains unchanged. Persistence of a region of reduced basal drag thus confirms that the main force balance results are insensitive to the exact choice of temperature.

Accuracy of force balance calculations also relies on the consistency between input datasets, which is to say the technique assumes datasets represent a common period of conditions. There is a ~1–3 year discrepancy between measurements defining the surface DEM and velocity dataset, meaning that this consistency is not strictly satisfied. However, rates of surface elevation change through the domain reported by the CryoSat-2 program are <1.5 m a^{-1} (Helm et al. 2014). As a result, changes in surface elevation over this short window are likely to be minimal and fall within the reported uncertainty. Thus, any change in surface elevation since collection of the velocity dataset is likely to have a negligible influence on the results.

The 4 km smoothing length scale may attenuate both the magnitude and distribution of calculated stresses to the extent that the magnitude of longitudinal and lateral effects is not adequately reflected. Indeed, this choice of resolution smooths basal topography in the lower ablation zone, which can show substantial relief (e.g. Lindbäck et al. 2014). One probable effect is a reduction in calculated lateral shear gradients, which may likely contribute more to the budget of forces in deeper troughs than is represented in our results. However, our primary objective is assessment of viscous effects through the reach of decreasing driving stress. Kamb and Echelmeyer (1986) deduced theoretically that the coupling length ranges from four to 10 times the ice thickness in ice sheets. The chosen length scale is approximately two to three times the local thickness through the driving stress reduction, and so should capture the effects of longitudinal coupling in the force balance calculation. Further, the driving stress feature itself is on the order of 10s of km. Thus, while the 4 km dataset resolution will not resolve effects acting on smaller spatial scales, it should adequately capture resistive stress gradients over scales on the order of the observed driving stress reduction. Further, because the smoothing length scale was chosen based on the propagated uncertainty of the input datasets, resolving the force budget at shorter spatial scales risks interpretation of noise as real signal.

F13.3 Basal hydraulic conditions

Basal flow conditions over the study domain are illustrated through calculation of total hydraulic potential and the potential gradient. Total hydraulic potential is the sum of potential due to bed elevation, and the pressure potential resulting from the pressure in the basal drainage system. The latter term results from complex interactions between varying meltwater discharge and basal processes, which remain poorly understood. Substantial temporal and spatial variations in water pressure have been measured in boreholes drilled in the lower ablation zone of the study area (i.e. <1 100 m elevation), making confident prediction of flow conditions difficult (Wright et al. 2016). Assessing potential gradients is further complicated by the fact that values are typically computed on gridded topographic datasets with an rigidly imposed length scale, rather than over circuitous drainage elements.

High in the ablation zone and above the ELA, however, basal water flux is likely to be more constant and, owing to thick ice and long travel paths (upwards of 100 km) to the margin, it is likely that water pressure is consistently near ice overburden. Consequently, we compute hydraulic potential and potential gradients under the assumption that water pressure is everywhere equal to ice overburden. However, for the reasons described above this represents an estimate of probable flow conditions, and is clearly of limited accuracy lower in the ablation zone.

Under the overburden assumption, total hydraulic potential and hydraulic potential gradient driving water flow are calculated respectively as:

$$\phi = \rho_w g B + \rho_i g (S - B) \quad \text{(F-S1)}$$

and:

$$\nabla\phi = -\rho_i g \left(\nabla S + \left(\frac{\rho_w}{\rho_i} - 1 \right) \nabla B \right) \quad \text{(F-S2)}$$

In Equations F-S1 and F-S2, ρ_w and ρ_i are densities of water and ice, respectively, B is the bed elevation, S is the surface elevation, and g is gravitational acceleration. Results are displayed in Figure F-S2.

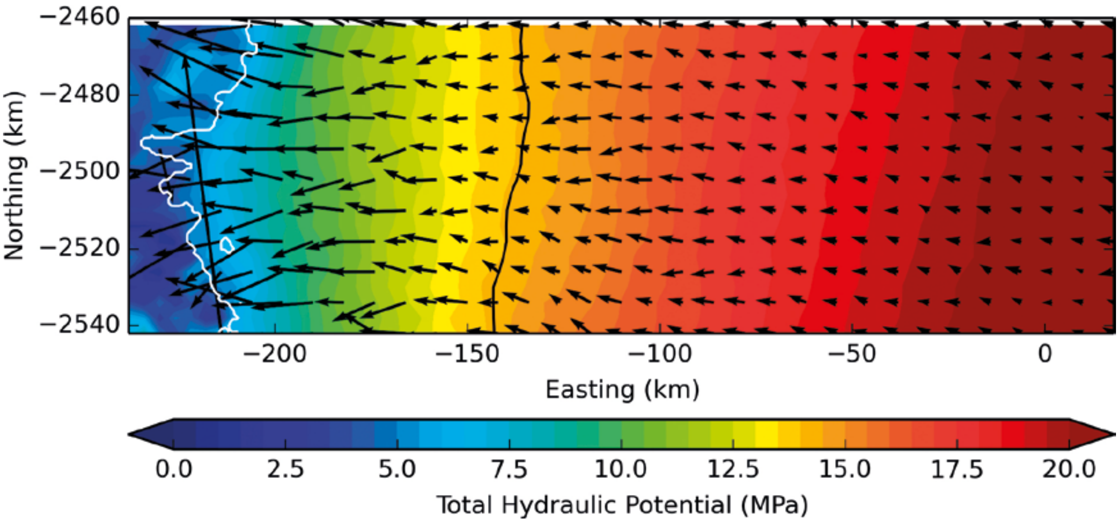

Figure F-S2. *Potential gradient vectors overlain on total hydraulic potential of the study area. Arrow length corresponds to the magnitude of the vector. Black line marks the long term ELA as discussed in the main text.*

F14 Supplementary material references

Doyle S H, Hubbard A, Fitzpatrick A W, van As D, Mikkelsen A B, Pettersson R, Hubbard B, 2014. Persistent flow acceleration within the interior of the Greenland ice sheet. Geophysical Research Letters 41, 899–905.

Helm V, Humbert A, Miller H, 2014. Elevation and elevation change of Greenland and Antarctica derived from CryoSat-2. The Cryosphere 8, 1539–1559.

Joughin I, Smith B E, Howat I M, Scambos T, Moon T, 2010. Greenland flow variability from ice-sheet-wide velocity mapping. Journal of Glaciology 56, 415–430.

Kamb B, Echelmeyer K A, 1986. Stress-gradient coupling in glacier flow: 1. longitudinal averaging of the influence of ice thickness and surface slope*. Journal of Glaciology 32, 267–284.

Layberry R L, Bamber J L, 2001. A new ice thickness and bed data set for the Greenland ice sheet 2. Relationship between dynamics and basal topography. Journal of Geophysical Research 106, 33781–33788.

Leuschen C, Gogineni P, Rodriguez-Morales F, Paden J, Allen C, 2010. IceBridge MCoRDS L2 Ice Thickness, Version 1. Boulder, CO USA: NASA DAAC: NASA DAAC at National Snow and Ice Data Center: NASA National Snow and Ice Data Center Distributed Active Archive Center. doi:http://dx.doi.org/10.5067/GDQ0CUCVTE2Q

Lindbäck K, Pettersson R, Doyle S H, Helanow C, Jansson P, Kristensen S S, Stenseng L, Forsberg R, Hubbard A L, 2014. High-resolution ice thickness and bed topography of a land-terminating section of the Greenland Ice Sheet. Earth System Science Data 6, 331–338.

Meierbachtol T W, Harper J T, Johnson J V, Humphrey N F, Brinkerhoff D J, 2015. Thermal boundary conditions on western Greenland: Observational constraints and impacts on the modeled thermomechanical state. Journal of Geophysical Research: Earth Surface 120, 623–636.

Ryser C, Lüthi M P, Andrews L C, Hoffman M J, Catania G a., Hawley R L, Neumann T A, Kristensen S S, 2014. Sustained high basal motion of the Greenland ice sheet revealed by borehole deformation. Journal of Glaciology 60, 647–660.

Wright P J, Harper J T, Humphrey N F, Meierbachtol T W, 2016. Measured basal water pressure variability of the western Greenland Ice Sheet: Implications for hydraulic potential. Journal of Geophysical Research: Earth Surface 121, 1134–1147.

Arkitektkopia AB, Bromma, 2019

SKB is responsible for managing spent nuclear fuel and radioactive waste produced by the Swedish nuclear power plants such that man and the environment are protected in the near and distant future.

skb.se